



The United Nations
University



ORKUSTOFNUN

Mathematical modeling of fluid flow and heat transfer in geothermal systems - an introduction in five lectures

by

**KARSTEN PRUESS
Earth Sciences Division,
Lawrence Berkeley National Laboratory
University of California, Berkeley
UNITED STATES**

**United Nations University
Geothermal Training Programme
2002 - Report 3
Published in October 2002**



GEOTHERMAL TRAINING PROGRAMME
Orkustofnun, Grensásvegur 9,
IS-108 Reykjavík, Iceland

Reports 2002
Number 3
and LBNL-51295

**MATHEMATICAL MODELING OF FLUID FLOW
AND HEAT TRANSFER IN GEOTHERMAL SYSTEMS
- AN INTRODUCTION IN FIVE LECTURES**

Karsten Pruess
Earth Sciences Division
Lawrence Berkeley National Laboratory
University of California, Berkeley
UNITED STATES

Lectures on reservoir engineering given in September 2002
United Nations University, Geothermal Training Programme
Reykjavík, Iceland
Published in October 2002

ISBN 9979-68-100-4

PREFACE

In order to secure the sustainable use of a geothermal reservoir, it is very important to understand the response of the system to exploitation. This makes it possible both to forecast how much energy can be withdrawn safely from the reservoir and facilitates reservoir management decisions during exploitation. The UNU Visiting Lecturer 2002, Dr. Karsten Pruess, has for many years been among the leaders in mathematical modelling and numerical simulation of geothermal reservoirs. He is a senior scientist at the Earth Sciences Division of the Lawrence Berkeley National Laboratory in California. He is the chief author of the widely used TOUGH2 geothermal reservoir simulator. He has also worked extensively on nuclear waste isolation and environmental contamination problems. He gave the lectures presented here at the UNU Geothermal Training Programme in Reykjavik in September 2002.

In the lectures, he defines the main parameters and principles involved in mathematical modelling of fluid flow and heat transfer in geothermal systems and describes the behaviour of different types of geothermal reservoirs under exploitation. His detailed and clearly written lecture notes will be of use to all students of geothermal reservoir engineering. We are very grateful to Karsten for writing up his lecture notes in such an excellent way and thus to make the lectures available to a much larger audience than those who were so fortunate in attending his lectures in Reykjavik.

Since the foundation of the UNU Geothermal Training Programme in 1979, it has been customary to invite annually one internationally renowned geothermal expert to come to Iceland as the UNU Visiting Lecturer. This has been in addition to various foreign lecturers who have given lectures at the Training Programme from year to year. It is the good fortune of the UNU Geothermal Training Programme that so many distinguished geothermal specialists have found time to visit us. Following is a list of the UNU Visiting Lecturers during 1979-2000:

1979 Donald E. White	United States	1991 Wang Ji-yang	China
1980 Christopher Armstead	United Kingdom	1992 Patrick Muffler	United States
1981 Derek H. Freeston	New Zealand	1993 Zosimo F. Sarmiento	Philippines
1982 Stanley H. Ward	United States	1994 Ladislaus Rybach	Switzerland
1983 Patrick Browne	New Zealand	1995 Gudm. Bödvarsson	United States
1984 Enrico Barbier	Italy	1996 John Lund	United States
1985 Bernardo Tolentino	Philippines	1997 Toshihiro Uchida	Japan
1986 C. Russel James	New Zealand	1998 Agnes G. Reyes	Philippines/N.Z.
1987 Robert Harrison	UK	1999 Philip M. Wright	United States
1988 Robert O. Fournier	United States	2000 Trevor M. Hunt	New Zealand
1989 Peter Ottlik	Hungary	2001 Hilel Legmann	Israel
1990 Andre Menjoz	France	2002 Karsten Pruess	United States

With warmest wishes from Iceland,

Ingvar B. Fridleifsson, director,
United Nations University
Geothermal Training Programme

INTRODUCTION

Mathematical modeling and numerical simulation have become standard techniques in the evaluation of geothermal reservoirs. They are used to assess the generating capacity of a geothermal field, to design production and injection operations, and to assist in various reservoir management decisions. Geothermal reservoir simulators are widely available, can be run on inexpensive personal computers, and have been used in several hundred field studies worldwide.

Geothermal reservoir simulation is based on the physics of fluid flow and heat transfer, on quantitative information about geothermal reservoir properties, and on the thermodynamics and thermophysical properties of reservoir fluids, chiefly water. The purpose of these lectures is to provide an introduction into the underpinnings and applications of reservoir simulation. Our goal is to provide readers with a basic understanding of reservoir simulation, so that they will be able to critically evaluate simulation studies and their limitations. We also hope that these notes will encourage wider use of geothermal reservoir simulators by non-specialists.

I am grateful to Ingvar B. Fridleifsson for providing the stimulus for assembling these lecture notes. In the approximately twenty-five years that I have been involved with geothermal reservoir simulation, I have benefitted greatly from discussions and collaborations with many colleagues, among them Paul Witherspoon, Nari Narasimhan, Michael O'Sullivan, Valgardur Stefansson, Marcelo Lippmann, Bo Bodvarsson, Sabodh Garg, John Pritchett, Sally Benson, Ashok Verma, Romano Celati, Claudio Calore, Alfredo Battistelli, Subir Sanyal, Tony Menzies, Curt Oldenburg, George Moridis, Stefan Finsterle, Christine Doughty, and Alexey Kiryukhin.

Karsten Pruess
Berkeley, California

TABLE OF CONTENTS

	Page
LECTURE I: HYDROTHERMAL SYSTEMS	1
1. Introduction	1
2. Natural Geothermal Gradients	2
2.1 Some Mathematical Issues	3
3. Hydrothermal Convection Systems	3
4. Fluid Flow	6
5. Mass Transport	11
LECTURE II: MASS AND ENERGY BALANCES	14
6. Mass Balance	14
7. Energy Balance	16
8. Fluid Properties	19
8.1 Water	19
8.2 Gases	24
8.3 Phase Partitioning	25
8.4 Brines	26
LECTURE III: NUMERICAL MODELING OF GEOTHERMAL SYSTEMS	27
9. Primer on Transport Processes	28
10. Overview of Reservoir Simulation	31
11. Preparation of Input Data	32
12. Grid Generation	34
13. Flow in Fractured Media	43
LECTURE IV: GEOTHERMAL RESERVOIR BEHAVIOR	47
14. Response to Fluid Production and Injection	47
14.1 Production from a Two-Phase Reservoir with Dissolved Solids and Non-Condensable Gas	47
14.2 Coupled Reservoir-Wellbore Flow	50
14.3 Injection of Cold Water	53
14.4 Five-Spot Production and Injection	55
14.5 Heat Sweep in a Vertical Fracture	57
15. Site-Specific Reservoir Modeling	59
LECTURE V: SPECIAL TOPICS	65
16. Water Injection into Depleted Vapor Zones	65
17. Phase Partitioning Tracers	68
18. Heat Pipe Systems	71
19. Flow Instabilities	75
19.1 Cerro Prieto	75
19.2 Mutnovsky	77
CONCLUDING REMARKS	80
ACKNOWLEDGEMENT	80
REFERENCES	81

LIST OF FIGURES

	Page
3.1 Dividing depth into small intervals	5
3.2 Thermal buoyancy flow in a conduit with a temperature gradient	6
3.3 Hydrothermal convection in a fluid layer heated from below	6
4.1 One-dimensional porous medium held between surfaces at constant pressure	6
4.2 Volume occupied by fluid during a unit of time	8
4.3 Rise of water level in a capillary tube	10
4.4 Capillary pressure function	10
4.5 Typical relative permeability functions	11
6.1 Space discretization in two dimensions	14
6.2 Space discretization and geometry data in the integral finite difference method	16
7.1 A volume of gas, held under pressure	17
7.2 Adiabatic expansion of a gas	18
8.1 Schematic temperature-pressure diagram of the phase states of pure water	20
8.2 Vapor pressure of water as function of temperature	21
8.3 Liquid and vapor density along the saturation line	22
8.4 Liquid and vapor viscosity along the saturation line	22
8.5 Liquid and vapor enthalpy along the saturation line	23
8.6 Pressure-enthalpy diagram for pure water and vapor	23
8.7 Phase partitioning of a volatile tracer	25
8.8 Henry's law coefficients for dissolution of CO ₂ in water	25
8.9 Brine densities at T=250°C and P =100 bar	26
8.10 Brine viscosities at T=250°C and P =100 bar	26
9.1 Schematic of physical and chemical processes occurring in a producing geothermal field	27
9.2 Illustration of a purely advective process in 1-D	28
9.3 A diffusive process in 1-D	29
9.4 Schematic of a solute dispersion bar	30
10.1 Iteration procedure for solution of mass and energy balances	32
11.1 Data groups for a simulation problem	33
12.1 Components of average temperature gradient	35
12.2 Portion of a grid with nodal points	36
12.3 Local grid refinement	36
12.4 Radial symmetry in a natural grid system	37
12.5 Five-spot well pattern with grid for modeling a 1/8 symmetry domain	38
12.6 Aerial view of computational grid for the Olkaria, Kenya geothermal field	39
12.7 Idealized flow system used for studying water injection into a vapor-dominated reservoir ..	40
12.8 Parallel and diagonal grids for a 2-D vertical section	40
12.9 2-D vertical section for modeling hydrothermal processes at Yucca Mountain, Nevada ..	41-42
13.1 Idealized double porosity model of a fractured porous media	44
13.2 Subgridding in the method of "multiple interacting continua" (MINC)	45
13.3 Schematic of MINC grid for modeling radial flow in a fractured reservoir	46
13.4 Flow connections in the "dual permeability" model	46
14.1 Illustration of 1-D radial model	48
14.2 TOUGH2/EWASG input data for constant-rate production from a 1-D cylindrical reservoir	49
14.3 Simulated thermodynamic conditions for 1-D radial flow problem	50
14.4 Contour plot of flowing bottomhole pressures	51
14.5 Flow behavior of a coupled reservoir-well system	53
14.6 Temperature fronts during non-isothermal injection into a 1-D fracture	54
14.7 Thermal breakthrough time as function of fluid residence time	55
14.8 Temperature profiles for five-spot problem along a line	56
14.9 Schematic diagram of injection-production system in vertical fracture	57
14.10 Temperature distribution in fracture plane after 5 years	58

	Page
14.11 Produced fluid temperature versus time for vertical fracture problem	58
15.1 General approach to reservoir evaluation	61
15.2 Flow chart for natural state modeling	63
16.1 Schematic diagram of fronts for cold water injection into a superheated vapor zone	65
16.2 Simulated temperatures for cold water injection into a superheated vapor zone	66
16.3 Schematic of cold water injection into a sub-vertical fracture filled with superheated steam .	67
16.4 Simulated plumes for injection at a rate of 10 kg/s into four heterogeneous vertical fractures	67
17.1 R-13 concentration in produced steam from wells in an undepleted region of The Geysers .	69
17.2 R-13 concentration in produced steam from wells in an depleted region of The Geysers . .	69
17.3 Five-spot production-injection system used for analysis of tracer migration	70
17.4 Simulated tracer breakthrough curves for five-spot problem in a vapor-dominated reservoir .	70
17.5 Breakthrough curves (depleted conditions)	71
18.1 Schematic of a heat pipe system	72
18.2 Heat flux and pressure gradient in vertical porous heat pipe	73
18.3 Boiling-point-for-depth curve for pure water	74
19.1 2-D vertical section model for fluid recharge at Cerro Prieto	76
19.2 Simulated vapor saturations in the Cerro Prieto III reservoir after 10 years of production .	76
19.3 Enthalpy and groundwater recharge fraction histories in the Cerro Prieto field	77
19.4 Example of co-seismic cycling in well #30, Mutnovsky geothermal field, Kamchatka	78
19.5 Conceptual model for flow cycling at Mutnovsky geothermal field, Kamchatka	79
19.6 Simulated pressure behavior at intersection of upper and lower fractures with the wellbore .	80

LIST OF TABLES

14.1 Parameters for five-spot problem	56
14.2 Parameters for fracture flow problem	59



LECTURE I: HYDROTHERMAL SYSTEMS

1. Introduction

Manifestations of the earth's hot interior involve a range of phenomena, from perilous volcanic activity to useful and beneficial hot springs, that have been known and used since prehistoric time. The Romans of antiquity made sophisticated use of natural warm waters for balneological purposes. The Maori of New Zealand used hot steaming ground for cooking. Many ancient cultures made use of the natural heat of the earth.

The fundamental source of heat in the earth is the radioactive decay of unstable isotopes that occur dispersed in small concentrations throughout the earth's volume, particularly in the crust. This decay heat is propagated towards the land surface by different heat transfer mechanisms, including heat conduction, convection of fluids (aqueous or magmatic), and by direct movement of hot molten rock towards shallower horizons, in the form of magma chambers, dikes, or volcanic discharges.

The modern quantitative study of heat began in the 1600s and 1700s, spurred on by continuous improvements in the use of heat for industrial purposes, chiefly as a source of mechanical work in steam engines and their predecessors. Characterization of the state of heat through quantitative measurements of temperature was pioneered by people such as Celsius, Fahrenheit, and Réaumur, each of which devised an apparatus for temperature measurement and a quantitative scale, based on the common observation that gases and fluids expand when heated. Up until the early 19th century, the prevalent view among scientists and engineers was that heat was a substance, albeit a "thin" and elusive one. This substance was called "phlogiston," and it was generally held that this phlogiston was coming out and going up in the air when e.g. a piece of wood was burned. Heat transfer was viewed as migration of this "phlogiston." The viewpoint that heat is some sort of substance was shared by giants in the field such as Fourier, who discovered the fundamental law of heat conduction (1822), and Carnot, who developed profound insight into the limitations for converting heat into mechanical work (1824). The recognition that heat is a state of matter and just another form of energy was not achieved until the 1840s, through the work of Robert Mayer (1842) and Joule on the "mechanical equivalent of heat."

Let us now turn our attention to subsurface systems in which heat effects play an important role.

2. Natural Geothermal Gradients

Rocks contain various amounts of radiogenic isotopes, whose natural radioactive decay produces heat. In typical continental crust, temperatures will increase by $\approx 3 \text{ }^{\circ}\text{C}$ for every 100 m depth. The ratio of temperature increase ΔT to vertical depth interval Δz over which it occurs is called “temperature gradient” and is written ∇T . According to the foregoing we have $\nabla T = \Delta T / \Delta z \approx 3/100 \text{ }^{\circ}\text{C/m} = 0.03 \text{ }^{\circ}\text{C/m}$ as an average temperature (or geothermal) gradient in continental crust. When average gradients prevail, we need to go down to about 6 km depth to reach a temperature of 200 $^{\circ}\text{C}$. Geothermal gradients can be enhanced locally or regionally due to special geologic conditions, for example, where the earth’s crust is unusually thin, or where hot molten rock has risen to shallower depths, forming igneous dikes or magma chambers. In regions with deep fluid circulation, average or moderately enhanced geothermal gradient can be sufficient to generate practically useful geothermal manifestations. An example is the Rhine graben between Germany and France, where tectonic activity has created fractures and faults that permit fluid circulation to great depth. The heated fluid subsequently may rise back up to shallower elevations, providing temperatures of 140 $^{\circ}\text{C}$ at depths of only 2000 m (Baria et al., 2000).

From Fourier’s law of heat conduction, the heat flux q (units: W/m^2 , Watts per square meter) associated with a temperature gradient ∇T is given by

$$\mathbf{q} = -K\nabla T \quad (2.1)$$

where K , the constant of proportionality, is called “thermal conductivity.” A typical value for rocks is $K \approx 2 \text{ W/m } ^{\circ}\text{C}$ (“watts per meter per degree Celsius”), so that we obtain for a typical continental heat flux

$$q \approx -2 \times 0.03 = 0.06 \text{ W/m}^2 \quad (2.2)$$

Over an area of 1 km^2 (10^6 m^2), the typical crustal heat flow rate would be $6 \times 10^4 \text{ W}$, or 60 kW, a small amount compared to heat extraction rates of typically tens to hundreds of megawatts in producing geothermal fields. Note that conduction is not the only mechanism of heat transfer. The flow of hot fluids (liquids and gases) through porous and permeable rocks gives rise to “convective” heat transfer, which may occur at much larger rates than can be accomplished by conduction. Additional heat transfer effects occur during phase change processes, such as boiling or condensation.

2.1 Some Mathematical Issues

Before proceeding further, we wish to note two somewhat subtle mathematical points that are “buried” in our introduction of a temperature gradient. Similar issues will arise later on in our discussion of numerical modeling of geothermal systems, and it is appropriate to provide some clarification here.

The first point is that, unless T is a linear function of depth z , the expression $\Delta T/\Delta z$ will depend on the magnitude of the interval Δz used to evaluate it. This ambiguity can be resolved rigorously through the methods of differential calculus, where $\Delta T/\Delta z$ is evaluated for a sequence of different z -increments Δz_i , and the behavior of $\Delta T/\Delta z_i$ is considered for the “limit” of $\Delta z_i \rightarrow 0$. In the lectures presented here we do not wish to make calculus a prerequisite, and we therefore bypass this aspect of mathematical rigor. From a practical viewpoint, when evaluating a temperature gradient (or other gradients such as pressure or solute concentration gradients), we consider that Δz should be chosen “suitably” small. Exactly what is “suitable” depends upon how temperature varies with position. Approximations to gradients that involve finite increments to the space coordinates are referred to as “finite differences.”

The second point is that, strictly speaking, the “gradient” is a vector, not a number. A vector is a mathematical object that has not only a magnitude but also a direction. A familiar example of a vector is velocity. A vector can be represented by an arrow which shows the direction, while the length of the arrow gives the magnitude of the vector. The quantity $\Delta T/\Delta z$ introduced above is the magnitude of the temperature gradient. In general, temperatures may vary in all directions, not just in the vertical (z) direction, and the proper mathematical notation for temperature gradient is $\nabla T = (\partial T/\partial x, \partial T/\partial y, \partial T/\partial z) \approx (\Delta T/\Delta x, \Delta T/\Delta y, \Delta T/\Delta z)$, indicating the “components” of that vector in the x , y , and z , directions, respectively. ∇T can be visualized as an arrow that is obtained by adding three arrows in x , y , and z , direction, with lengths of $\Delta T/\Delta x$, $\Delta T/\Delta y$, and $\Delta T/\Delta z$.

3. Hydrothermal Convection Systems

Consider a reservoir of fluid with density ρ . Under static conditions (no flow), the fluid pressure is given by the weight of the fluid column per unit area and increases with depth z according to

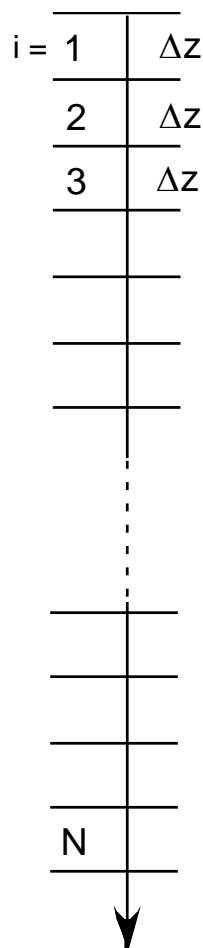
$$P_h(z) = \rho g z \quad (3.1)$$

For water at ambient conditions of temperature and pressure we have $\rho \approx 1000 \text{ kg/m}^3$. Acceleration of gravity is $g = 9.81 \text{ m/s}^2 \approx 10 \text{ m/s}^2$, so that the pressure increase in a column of water for 1 m increase in depth is approximately $1000 \text{ kg/m}^3 \times 10 \text{ m/s}^2 \times 1 \text{ m} = 10^4 \text{ kg/m s}^2$. A force acting on 1 kg of mass and producing an acceleration of 1 m/s² is called 1 N (“Newton”), i.e., 1 N = 1 kg m/s². The previously calculated pressure increase per meter in a column of water at ambient conditions can be written as 10⁴ N/m². A force of 1 N per m² is abbreviated as 1 Pa (Pascal); so the pressure in our water column increases by 10,000 Pa per meter depth. Another commonly used pressure unit is 1 bar = 10⁵ Pa, which is close to mean atmospheric pressure at sea level (1.013 bar), and corresponds to a 10 m column of water.

Fluid densities generally vary with depth as functions of temperature, pressure, and salinity. For liquids, the temperature and pressure dependence of density can be approximated as

$$\rho = \rho_0 [1 - \alpha(T - T_0) + \beta(P - P_0)] \quad (3.2)$$

Here, α is the expansivity and β the compressibility of the fluid. When fluid density varies with depth, because of generally increasing temperatures and pressures, Eq. (3.1) is no longer applicable to calculate the dependence of fluid pressure on depth. We generalize this equation by dividing the total depth z into N small intervals of length $\Delta z = z/N$ (Fig. 3.1).



The depth reached after i intervals is z_i :

$$z_i = i \times \Delta z \quad (3.3)$$

The pressure increase in the i -th interval is:

$$\Delta P_i = \rho_i g \Delta z \quad (3.4)$$

where $\rho_i = \rho_i(T_i, P_i)$ is the average fluid density in interval i . When the intervals are chosen “small”, 1 m, say, we may take ρ_i to be the density at the end of the previous interval. We can start from the land surface and in the first interval take $\rho_1 = \rho_0$. In the second interval we take $\rho_2 = \rho(P_1)$, then $\rho_3 = \rho(P_2)$, and so on. Summing all pressure increases, we obtain after N intervals:

$$P(z = N\Delta z) = \sum_{i=1}^N \Delta P_i = \sum_{i=1}^N \rho_i g \Delta z \quad (3.5)$$

As is shown in calculus, when we let $\Delta z \rightarrow 0$ we obtain the integral

$$P(z) = \int_0^z \rho g dz' \quad (3.6)$$

Figure 3.1 Dividing depth into small intervals Δz , numbered $i = 1, 2, \dots, N$.

Warm water is less dense than cold water, so a column of warmer water weighs less than a column of colder water. We have the phenomenon of “thermal buoyancy” (Fig. 3.2). Fluid pressure at the bottom of the left (colder) column of water is greater than at the bottom of the right (warmer) column, causing fluid circulation as indicated by the arrows. The left column could represent conditions in a recharge zone of a geothermal field, while the right column may represent conditions in the center of the field.

For hydrothermal circulation to occur, we need not only a temperature gradient. We also need appropriate permeability, and we need a supply of fluids. Another configuration in which thermal buoyancy flow can take place is shown in Fig. 3.3.

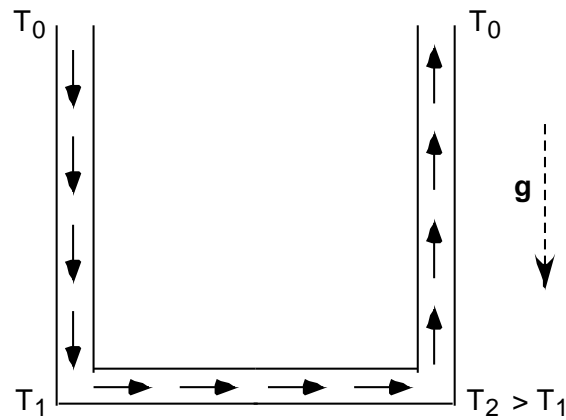


Figure 3.2. Thermal buoyancy flow in a conduit with a temperature gradient.

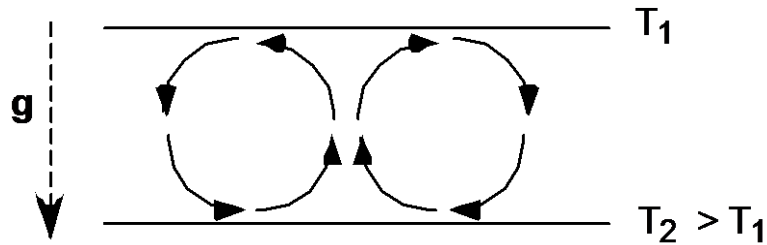


Figure 3.3. Hydrothermal convection in a fluid layer heated from below.

4. Fluid Flow

Fluids move in response to forces, the most important of which are pressure forces and the force of gravity. Capillary pressures may also be important. The fundamental law relating fluid flow to the forces causing the flow was established by Henri Darcy (1856), based on a series of experiments he did to observe water flowing through a sandpack. Consider a one-dimensional horizontal porous medium held between pressures P_1 and $P_1 + \Delta P$.

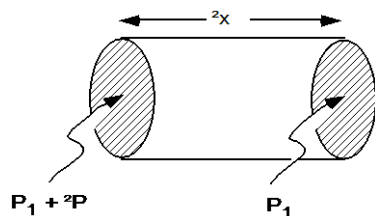


Figure 4.1. One-dimensional porous medium held between surfaces at constant pressure.

For the conditions shown in Fig. 4.1, fluid will flow from left to right. The rate of fluid flow depends not on the magnitude of the pressure change as such, but on the “intensity” of pressure change, i.e., on the magnitude of pressure change per unit length, the so-called

pressure gradient, $\Delta P/\Delta x$. Darcy's experiments showed that the fluid mass flow rate F per unit cross-sectional area of the medium is proportional to the pressure gradient,

$$F = -k \frac{\rho}{\mu} \frac{\Delta P}{\Delta x} \quad (4.1)$$

The minus-sign occurs because fluid flows from higher pressure to lower pressure, analogous to heat flowing from higher temperature to lower temperature. In Eq. (4.1) k is the so-called "absolute permeability," a measure of the ease with which fluid can migrate through a porous medium, and μ is viscosity, which is a measure of the internal friction of the flowing fluid. The SI unit for permeability is m^2 ; in practical field applications, the unit "darcy" is often used; we have the correspondence $1 \text{ darcy} = 1 \text{ d} \approx 10^{-12} \text{ m}^2$. For 3-D flows, Eq. (4.1) is generalized to read

$$\begin{pmatrix} F_x \\ F_y \\ F_z \end{pmatrix} = -k \frac{\rho}{\mu} \begin{pmatrix} \Delta P/\Delta x \\ \Delta P/\Delta y \\ \Delta P/\Delta z - \rho g \end{pmatrix} \quad (4.2)$$

Here we have introduced flux components in x , y , and z -directions, each of which responds to the component of pressure gradient in its own direction. For the vertical component, we have added the so-called "body force" from gravity. Equations such as (4.2) can be written more compactly in vector notation. We denote the triplet (F_x, F_y, F_z) as \mathbf{F} , and write the pressure gradient as $(\Delta P/\Delta x, \Delta P/\Delta y, \Delta P/\Delta z - \rho g) = \nabla P$. Eq. (4.2) can be rewritten as

$$\mathbf{F} = -k \frac{\rho}{\mu} (\nabla P - \rho g) \quad (4.3)$$

where the vector \mathbf{g} of gravitational acceleration is given by the components $(0, 0, g)$. Dividing the mass flux by the fluid density gives the volumetric flux (amount of fluid volume crossing a unit cross sectional area per unit of time).

$$\mathbf{u} = -\frac{k}{\mu} (\nabla P - \rho g) \quad (4.4)$$

In groundwater hydrology it is customary to write volumetric flux in terms of a "pressure head" $h = P/(\rho g)$, which has units of length. This is very useful under conditions where fluid density is approximately constant, because then a factor ρg can be extracted from the pressure gradient term to give

$$\mathbf{u} = -K \nabla h \quad (4.5)$$

where $K = k \rho g / \mu$ is the hydraulic conductivity (units of m/s), and $h = P / (\rho g) + z$ is the hydraulic head (pressure head plus “elevation head” z). In geothermal applications we usually encounter conditions where fluid density can be quite variable, due to dependence on temperature, pressure, and salinity, so that Eq. (4.5) is of limited usefulness and Eq. (4.4) is used.

The volumetric flux \mathbf{u} is sometimes referred to as the “Darcy velocity,” but it is not the velocity with which the fluid parcels are actually flowing. The latter quantity is known as the “pore velocity,” denoted by \mathbf{v} . Fig. 4.2 shows that the volume crossing a unit cross-sectional area per unit time is given by

$$\mathbf{u} = \phi \mathbf{v} \quad (4.6)$$

where ϕ is the porosity of the medium. Eq. (4.6) implies that in media with low effective porosity the pore velocity can be considerably larger than the Darcy velocity. Practical examples are seen in fractured media, where solute tracers may migrate with very large velocities, often as large as tens of meters per hour.

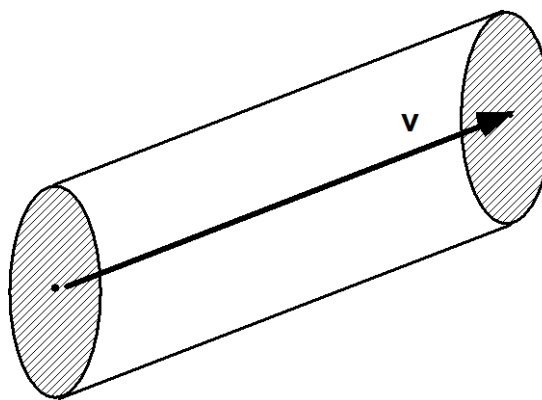


Figure 4.2. Volume occupied by fluid crossing the left interface during a unit of time.

Eq. (4.3) is written for the case when the pore space contains a single fluid phase, for example a liquid (aqueous) phase. In geothermal reservoirs we often encounter situations where two phases, liquid and gas, coexist in the pore space of the medium. Each of the two phases flows under its own pressure gradient and body force, but the effective permeability of the medium is reduced relative to single-phase conditions, because each of the flowing phases has only

part of the pore space available. This effect is taken into account by introducing so-called “permeability reduction factors,” or “relative permeabilities” $k_{r\beta}$ for phases $\beta = \text{liquid, gas}$, as follows.

$$\mathbf{F}_\beta = -k \frac{k_{r\beta} \rho_\beta}{\mu_\beta} (\nabla P_\beta - \rho_\beta \mathbf{g}) \quad (4.7)$$

The coefficients $k_{r\beta}$ represent the reduction in available permeability due to the fact that only a fraction of the pore space is occupied by phase β . The fraction of pore space occupied by a fluid phase is termed its saturation S_β , and the relative permeabilities are functions of S_β , $k_{r\beta} = k_{r\beta}(S_\beta)$.

P_β ($\beta = \text{liquid, gas}$) are the pressures in liquid and gas phases, which in general will be different, due to the surface tension of water and the fact that most mineral surfaces are hydrophilic, i.e., are preferentially wetted by water. The pressure of the liquid phase is generally lower than that of the gas phase. The difference $P_g - P_l = P_{\text{cap}} > 0$ is termed the capillary pressure and is a function of saturation, $P_{\text{cap}} = P_{\text{cap}}(S_l)$. (Sometimes capillary pressure is defined as $P_l - P_g < 0$.) The term originates from the well-known phenomenon of water rising in a capillary tube, see Fig. 4.3. The capillary rise, h , is proportional to surface tension σ and cosine of contact angle γ , and inversely proportional to the radius R of the tube. The pressure associated with the capillary rise is

$$P_{\text{cap}} = \rho g h = \frac{2\sigma \cos \gamma}{R} \quad (4.8)$$

In porous media, capillary pressure comes about through the combined action of many pore channels with generally irregular shape, corresponding to a broad range of capillary radii. Fig. 4.4 shows a typical capillary pressure function for a porous medium with a permeability of $100 \times 10^{-15} \text{ m}^2$. Capillary pressures become stronger for media with small permeability (small pore radii). In geothermal reservoir simulation, capillary pressures have usually been neglected. There may be some justification for this from the fact that surface tension decreases with increasing temperature.

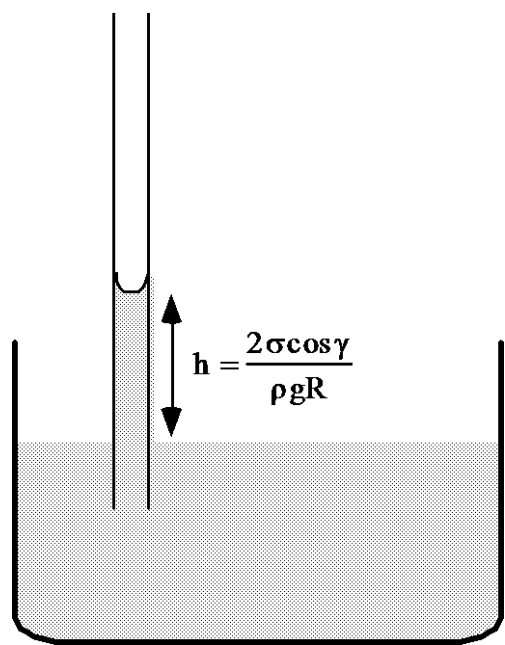


Figure 4.3. Rise of water level in a capillary tube.

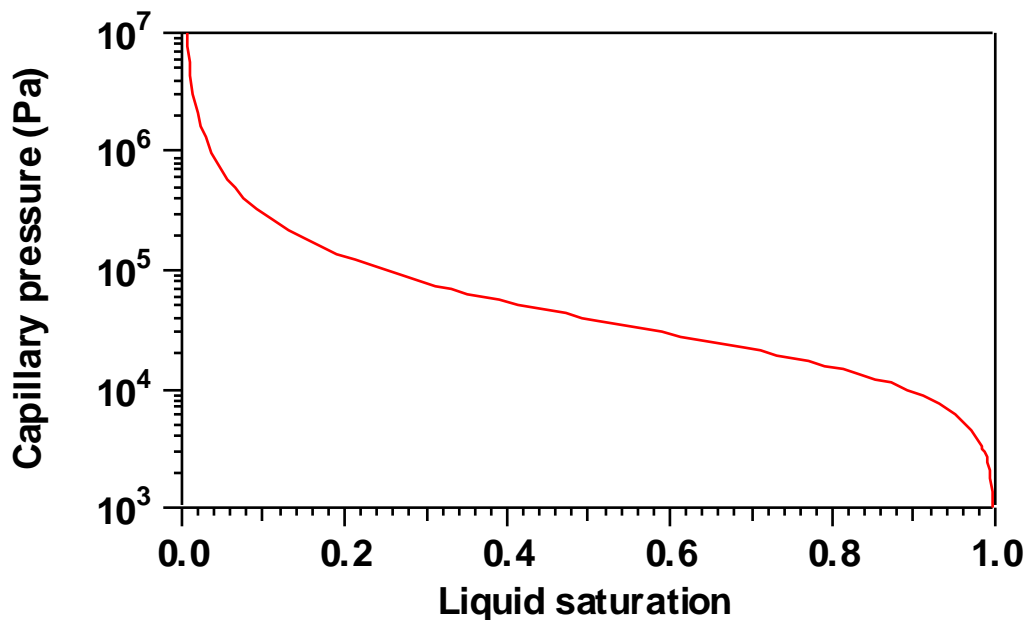


Figure 4.4 Capillary pressure function.

The functional form of the relative permeability functions $k_{r\beta}(S_\beta)$ depends on the geometry of the pore space and the connectivity of the pore network. Relative permeabilities can be measured on specimen of permeable media in the laboratory, but such determination has limited value for the reservoir scale, where flow may largely occur through fractures that

are connected on a scale far greater than can be studied in the laboratory. The spacing between major fractures in geothermal reservoirs may be of the order of 10 - 100 m or more. In practice, relative permeabilities are often treated as adjustable parameters in models of geothermal systems. An example of typical gas (vapor) and liquid relative permeability functions for porous media is given in Fig. 4.5. The liquid relative permeability curve $k_{rl}(S_{liq})$ is of the van Genuchten type (1980), with $k_{rl} \rightarrow 0$ as S_{liq} approaches the “irreducible” saturation $S_{lr} = 0.3$. Gas relative permeability is a Corey curve (1954) with an irreducible gas saturation of $S_{gr} = 0.05$. The different functional forms of vapor and liquid relative permeabilities can be understood by conceptualizing the porous medium as a network of capillary tubes with different radii. When a fully water-saturated porous medium is being desaturated, capillary pressure effects cause the large capillaries to desaturate first, leading to a steep decrease of effective permeability for the liquid phase. Conversely, at low liquid saturations only the smallest capillaries retain liquid. These make only a small contribution to overall permeability, so that there is only a modest reduction in vapor phase relative permeability.

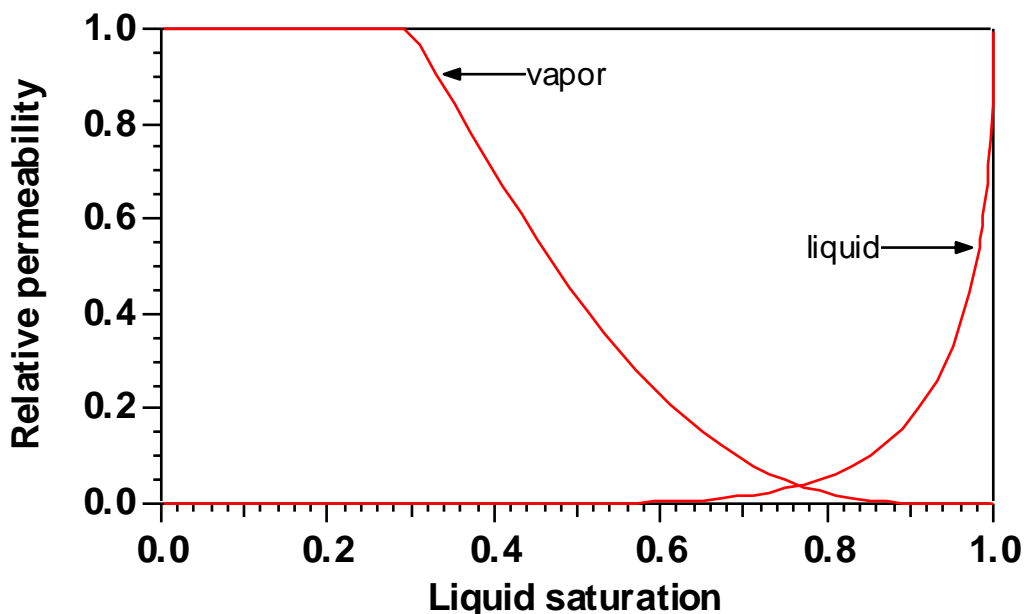


Figure 4.5. Typical relative permeability functions.

5. Mass Transport

Hydrothermal fluids are not pure substances, but generally are mixtures of several mass components or chemical species. The dominant fluid component is usually water, and for practical reservoir studies it is often reasonable to ignore other components. The aqueous phase generally contains solutes such as NaCl and other salts, as well as dissolved non-

condensable gases, such as CO₂, H₂S, and noble gases, and constituents of rock minerals such as SiO₂. If a gas phase is present, it usually is predominantly H₂O, but may also contain other gases. Let us consider a mass component κ such as CO₂, which may be present simultaneously in the gas phase and in the aqueous (liquid) phase, with mass fractions of X_g ^{κ} and X_l ^{κ} , respectively. The total mass flux of component κ due to fluid flow is then

$$F^{\kappa} = X_g^{\kappa} F_g + X_l^{\kappa} F_l \quad (5.1)$$

In addition to the “advection” described by Eq. (5.1), mass transport occurs by means of molecular diffusion, that is, due to the random motion of solute and solvent molecules. Diffusive mass flux is given by Fick’s law.

$$f_{\beta}^{\kappa} = -\phi \tau_0 \tau_{\beta} \rho_{\beta} d_{\beta}^{\kappa} \nabla X_{\beta}^{\kappa} \quad (5.2)$$

The driving force for diffusion is the mass fraction gradient, $\nabla X_{\beta}^{\kappa}$. Equation (5.2) without the three coefficients $\phi \tau_0 \tau_{\beta}$ would give the diffusive flux of component κ in a “free” phase β , when no porous medium is present. The coefficient d_{β}^{κ} is known as “diffusivity” and has units of m²/s. Diffusivities depend on the nature of the components that are diffusing, and may also depend on other parameters, such as temperature and pressure. Typical diffusivities for aqueous solutes are of order 10⁻⁹ - 10⁻¹⁰ m²/s, while gas phase diffusivities are of order 10⁻⁸ m²/s at typical geothermal reservoir conditions. The porosity ϕ in Eq. (5.2) accounts for the reduction in volume available for diffusion due to the porous medium, τ_0 is a tortuosity coefficient that represents the reduction in diffusion due to tortuous paths, and τ_{β} is an additional tortuosity coefficient that comes into play because fluid volumes for diffusion decrease, and path lengths increase, when more than one phase occupies the pore space.

The mass components are transported in the flow according to the actual pore velocities, which due to the (partially) random nature of porous media will exhibit local variability. This causes a dispersion of a solute plume, an effect that is not captured by the flux law Eq. (5.1) which ignores such local variability and addresses only average flow velocities. Dispersion has often been modeled in analogy to diffusion, but this approach has been thoroughly discredited through an extensive body of hydrogeologic research during the last twenty years. Proper modeling of mass transport in porous media remains a difficult challenge (see Section 9).

We observe a formal analogy between the laws for heat conduction, fluid flow, and molecular diffusion. In each case the flux is given by the product of a driving force (gradient of temperature, pressure, mass fraction) and a coefficient that represents a “conductivity” of the medium for the particular process. The three flux laws are identical in form to Ohm’s law for electric current, which is $I = (1/R)*U$, where $1/R$ is conductivity (inverse resistivity), and U is the voltage drop across the resistor.



LECTURE II: MASS AND ENERGY BALANCES

6. Mass Balance

Of fundamental importance for fluid flow studies, whether in porous media or in free space, is the mass balance or mass conservation equation. Simply put it states that the change in fluid mass in some reservoir volume is given by the net inflow across the surface of that volume, plus contributions from sinks (production wells) and sources (injection wells).

$$\boxed{\text{change in fluid mass in volume } V} = \boxed{\text{net fluid inflow across surface of } V} + \boxed{\text{net gain of fluid from sinks and sources}} \quad (6.1)$$

A mass balance as shown in Eq. (6.1) holds for any (sub-)volume of a reservoir, regardless of its shape and size. Mass balances may be applied to an entire reservoir, viewing it as a large fluid tank, or they may be applied to any subvolume or subdomain. In reservoir simulation, a reservoir volume is broken down into many small subvolumes, generally referred to as “volume elements” or “grid blocks,” and mass balances are set up for each of them and solved by computer. Although different choices for volume elements are possible (see Section 12), from a practical viewpoint it is best to think of them as boxes or, in two dimensions, rectangles (Fig. 6.1). The centroids of the grid blocks are referred to as “nodal points,” and we associate average pressure, temperature, etc. in a grid block with these nodal points.

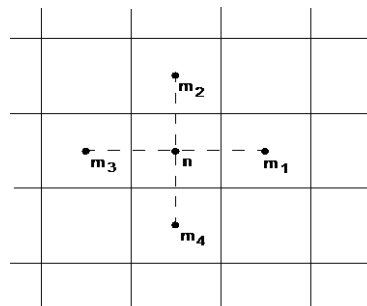


Figure 6.1. Space discretization in two dimensions, showing a grid block n and its neighbors m_i .

For simplicity, let us consider a single-phase system with a single-component fluid (water), and write down a mass balance for volume element or grid block n . The rate at which fluid enters grid block n from neighboring grid blocks m is given by

$$\sum_m A_{nm} F_{nm} \quad (6.2)$$

where the summation runs over all grid blocks that share a common interface with grid block n. A_{nm} is the interface area between grid blocks n and m, and F_{nm} is the average mass flux across that interface, counted positive when flow is from m to n. The total change in fluid mass content in grid block n from flows to and from neighboring grid blocks over a time interval Δt is given by

$$\Delta M_n = V_n \Delta M_n = \Delta t \left\{ \sum_m A_{nm} F_{nm} + Q_n \right\} \quad (6.3)$$

Here we have also introduced contributions from sinks and sources at a total net rate of Q_n . V_n is the volume of the grid block in question, ΔM_n is the change of fluid mass in V_n , and ΔM_n is the change in fluid mass per unit volume during the time Δt . For reference we give expressions for the fluid mass per unit volume for different conditions.

$$\text{single phase, single component} \quad M = \phi \rho \quad (6.4)$$

$$\text{single phase, multi-component} \quad M^\kappa = \phi \rho X^\kappa \quad (6.5)$$

$$\text{multi-phase, multi-component} \quad M^\kappa = \phi \sum_\beta S_\beta \rho_\beta X_\beta^\kappa \quad (6.6)$$

Here, ϕ is porosity, X^κ is mass fraction of component κ , and the subscript β refers to fluid phase (gas, liquid). S_β is the saturation of phase β , i.e., the fraction of pore volume occupied by that phase.

From Eq. (4.3), a finite difference expression for the average flux F_{nm} in a single-phase system across the interface between grid blocks n and m can be written as (see Fig. 6.2)

$$F_{nm} = k_{nm} \left[\frac{\rho}{\mu} \right]_{nm} \left[\frac{P_m - P_n}{D_{nm}} + \rho_{nm} g_{nm} \right] \quad (6.7)$$

where the subscripts (nm) denote a suitable averaging at the interface between grid blocks n and m (interpolation, harmonic weighting, upstream weighting). P_n and P_m are (average) pressures in the

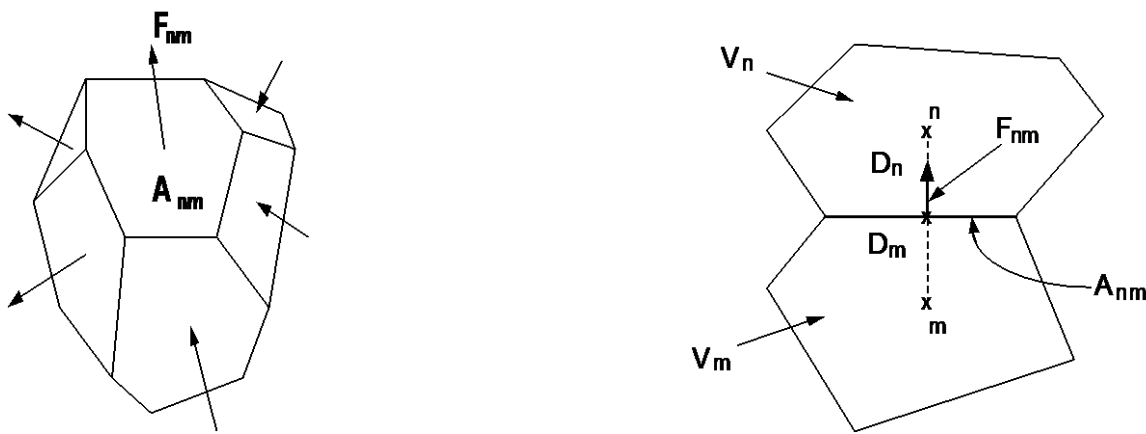


Figure 6.2. Space discretization and geometry data in the integral finite difference method.

two grid blocks, $D_{nm} = D_n + D_m$ is the distance between the nodal points n and m, and g_{nm} is the component of gravitational acceleration in the direction from m to n. For multiphase conditions, an analogous expression can be written based on Eq. (4.7).

In order to get useful information from a mass balance, it is necessary to know formation parameters appearing in the flux expressions. We also need information about fluid properties such as density and viscosity, and their dependence on fluid pressure and temperature. We will revisit mass balances after some review of these topics.

7. Energy Balance

Energy balances are more complicated than mass balances, primarily because thermal energy is not conserved as such, but may be partially converted into mechanical work and vice versa. This is expressed by the First Law of Thermodynamics, or energy balance,

$$\Delta U = G + W \quad (7.1)$$

where the change ΔU in internal energy of a system is due to heat transfer G and mechanical work W done to the system. Here we consider both heat transfer and mechanical work as positive when they are done to the system. Let us consider a thermodynamic system consisting of a fixed quantity of gas occupying a volume V at a pressure P (see Fig. 7.1). If we add a

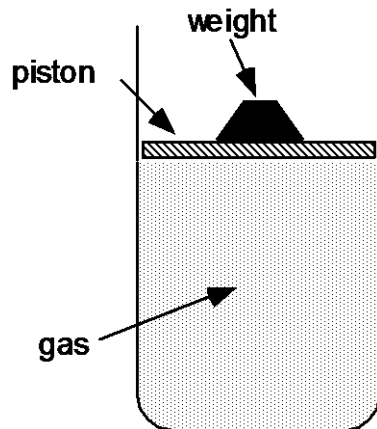


Figure 7.1. A volume of gas, held under a pressure that is equal to the gravity force F_g on the weight, divided by the piston area A , $P = F_g/A$.

thermal energy G to this gas, both its temperature and volume will increase, while under the (idealized) arrangement shown in Fig. 7.1 the pressure must remain constant. The work done to the gas is $W = -F_g \Delta z$, where F_g is the force acting on the piston, and Δz is the distance over which the piston moves upward to accommodate the increase in gas volume. This work is counted as negative because it is done by the system to its surroundings, thus reducing its energy content. We have $F_g = P A$, so that

$$W = -P A \Delta z = -P \Delta V \quad (7.2)$$

where the volume increase is $\Delta V = A \Delta z$. We see that of the total thermal energy G transferred to the gas, only the portion $G - P\Delta V$ is added to its internal energy, the remainder $P\Delta V$ being converted into mechanical work. In geothermal reservoir processes, the only significant mechanical work is that due to pressure forces; other forms of mechanical work do occur (Bird et al., 1960) but are not practically important and will not be considered further. A more complete discussion of mechanical work is given by Bird et al. (1960), and, specifically for geothermal applications, by Brownell et al. (1977).

Using Eq. (7.2), the First Law of Thermodynamics, Eq. (7.1), may be written

$$\Delta U = G - P\Delta V \quad (7.3)$$

Eq. (7.3) shows that when a gas is compressed, $\Delta V < 0$, its internal energy will increase unless heat is withdrawn ($G < 0$).

An important process is the “adiabatic” expansion (or compression) of a gas, i.e., an expansion process in which no thermal energy is exchanged with the surroundings. Consider an arrangement as shown in Fig. 7.2. Suppose a unit mass of gas with volume $v_1 = 1/\rho_1$ is pushed

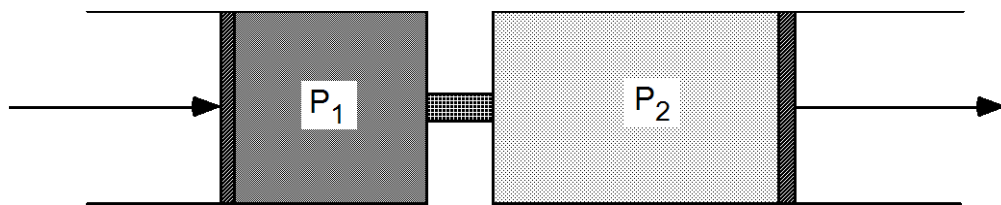


Figure 7.2. Adiabatic expansion of a gas.

through a throttle (choke), while pressure is maintained constant at P_1 on one side, P_2 on the other. According to Eq. (7.3) the change in internal energy per unit mass, $u_2 - u_1$, must be equal to the net work done to the system, which is $P_1 v_1 - P_2 v_2$.

$$u_2 - u_1 = P_1 v_1 - P_2 v_2 \quad (7.4)$$

so that

$$u_2 + P_2 v_2 = u_1 + P_1 v_1 \quad (7.5)$$

The quantity that is conserved in this process is called specific enthalpy, $h = u + Pv = u + P/\rho$. Adiabatic expansion is a reasonable model for many geothermal applications, for example, for flow of a two-phase mixture of water and steam down a pressure gradient to a separator. If produced enthalpy is h , and the separator operates at a pressure P_s where specific enthalpies of vapor and liquid are h_{vs} and h_{ls} , respectively, then conservation of specific enthalpy demands that $h = X h_{vs} + (1-X) h_{ls}$, where X is the mass fraction of two-phase fluid converted to steam. For a given separator pressure P_s the specific enthalpies of vapor and liquid can be obtained from “steam tables” (see Section 8.1, below), so that the mass fraction converted to steam can be calculated.

$$X = \frac{h - h_{ls}}{h_{vs} - h_{ls}} \quad (7.6)$$

For a finite (sub-)volume V of a flow system, when not only heat and work but also fluids may be exchanged with the surroundings, the energy balance can be written in the following form.

$$\boxed{\text{change in internal energy in volume } V} = \boxed{\text{net transfer of energy by fluid flow}} + \boxed{\text{mechanical work done to volume } V} + \boxed{\text{net heat transfer by conduction}} + \boxed{\text{net energy gain from sinks and sources}} \quad (7.7)$$

We now consider specific mathematical expressions for the various terms. The internal energy per unit volume in a general multiphase system is given by

$$M^h = (1-\phi)\rho_R C_R T + \phi \sum_{\beta} S_{\beta} \rho_{\beta} u_{\beta} \quad (7.8)$$

where ρ_R and C_R are, respectively, grain density and specific heat of the rock, T is temperature, and u_{β} is specific internal energy in phase β . Total internal energy in a grid block n is obtained by multiplying Eq. (7.8) with the grid block volume. The change in internal energy over some period of time is obtained by evaluating Eq. (7.8) for the thermodynamic conditions (temperature, pressure, saturation, etc.) at the beginning and end of that time period, and then taking the difference.

Energy transfer due to fluid flow and associated mechanical work is calculated by multiplying the mass flow rates by the corresponding specific enthalpies.

$$F^h = \sum_{\beta} h_{\beta} F_{\beta} \quad (7.9)$$

where the multiphase mass fluxes are given by Eq. (4.6). Conductive heat transfer is given by Eq. (2.1), and energy sinks and sources are calculated by multiplying mass rates with the appropriate specific enthalpies.

8. Fluid Properties

Geofluids in general consist of liquid-gas mixtures of water and steam, with dissolved solids such as NaCl and non-condensable gases such as CO₂. The physical properties of water are fundamental for an understanding of geothermal reservoirs and will be reviewed first.

8.1 Water

For temperature and pressure conditions of interest to geothermal engineers, water may exist as a single-phase liquid, as a single-phase gas called “vapor” or “steam,” or as a two-phase mixture of water and steam. At any given temperature, there is a unique pressure, known as “saturated vapor pressure” and denoted by $P_{\text{sat}}(T)$, at which vapor and liquid may

coexist (Fig. 8.1). At pressures larger than P_{sat} , we can only have single-phase liquid, while at pressures lower than P_{sat} we have single-phase vapor (see Figs. 8.1-2). At increasing temperatures the properties of vapor and liquid become more similar, and differences between the two phases vanish at the “critical point” ($T_{\text{crit}}, P_{\text{crit}} = (374.15 \text{ }^{\circ}\text{C}, 221.2 \text{ bars})$). Beyond the critical point there is only a single “supercritical” phase of water. The functional relationship of $P_{\text{sat}}(T)$ as well as properties such as densities, viscosities, and specific enthalpies of liquid water and steam have been thoroughly studied through experimental observations and theoretical analyses, and are available in handbooks or through mathematical correlations known as “steam tables” (IFC, 1967; Keenan et al., 1969). Figs. 8.2-5 through show liquid and vapor properties along the saturation line as functions of temperature, calculated from the IFC (1967) steam table equations as coded in the TOUGH2 reservoir simulator (Pruess et al., 1999).

A very useful diagram for representing water properties that are important for two-phase geothermal reservoirs is the pressure-enthalpy diagram, Fig. 8.6.

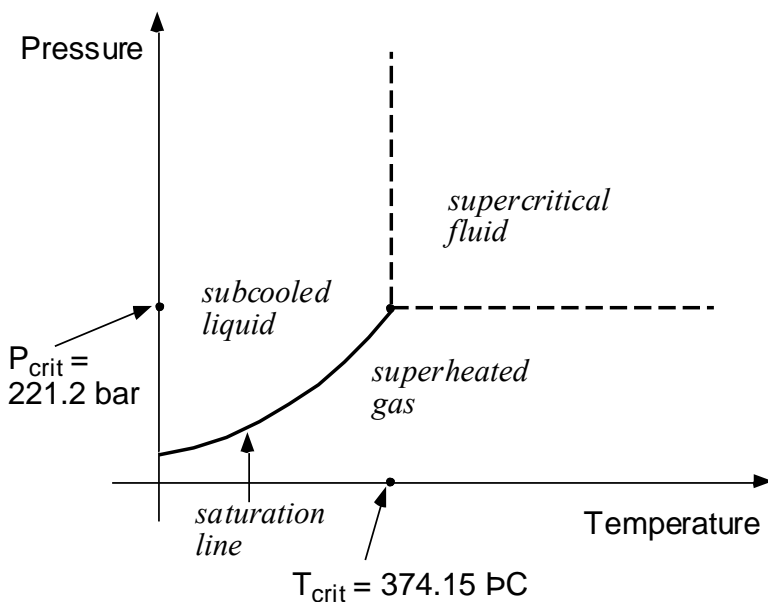
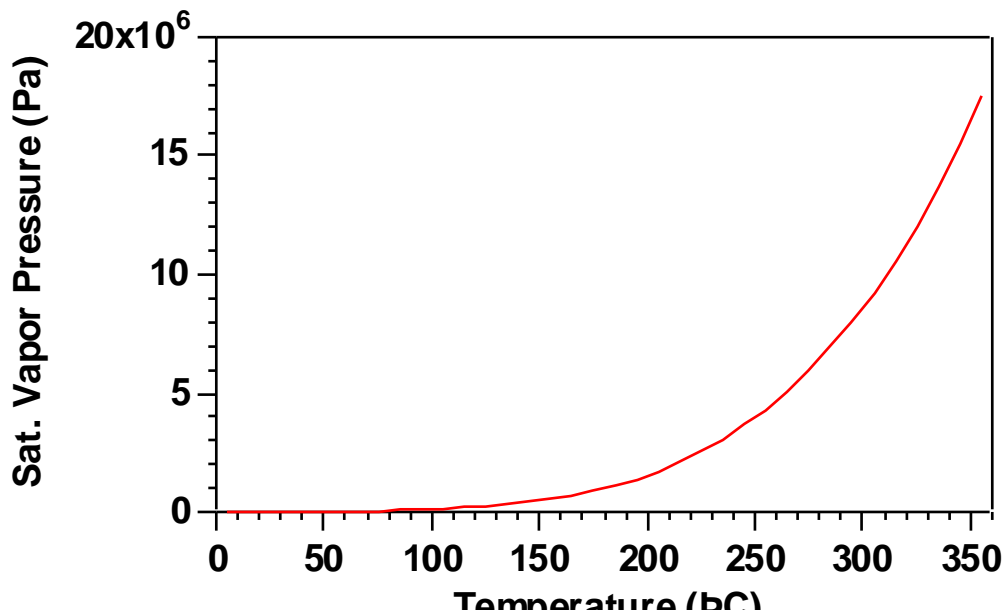
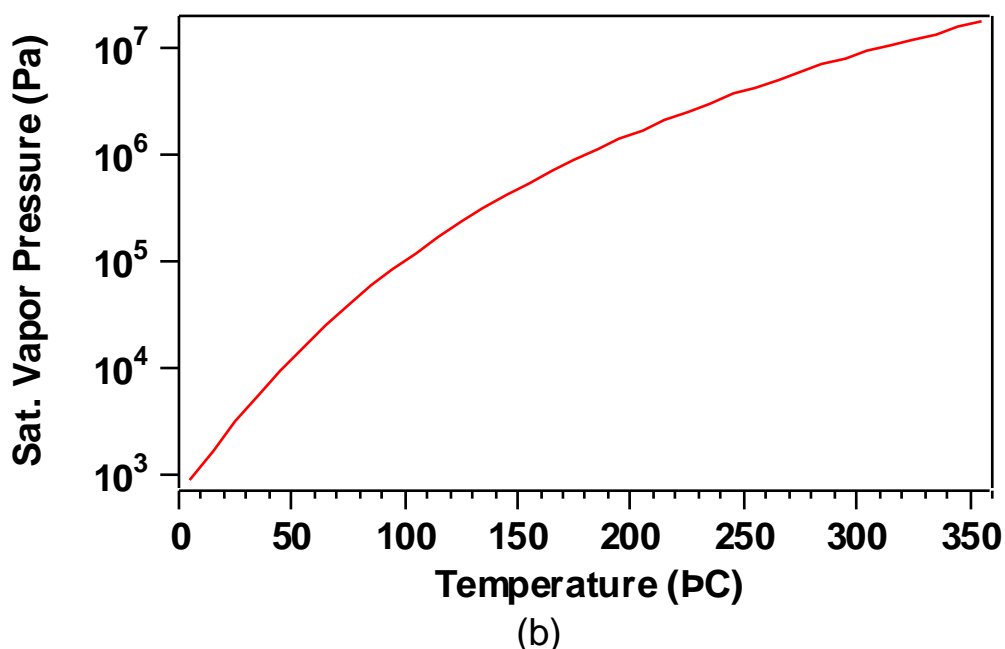


Figure 8.1 Schematic temperature-pressure diagram of the phase states of pure water.



(a)



(b)

Figure 8.2 Vapor pressure of water as function of temperature on linear (a) and logarithmic scale (b). The data were calculated from IFC (1967) steam table equations as coded in the TOUGH2 reservoir simulator (Pruess et al., 1999).

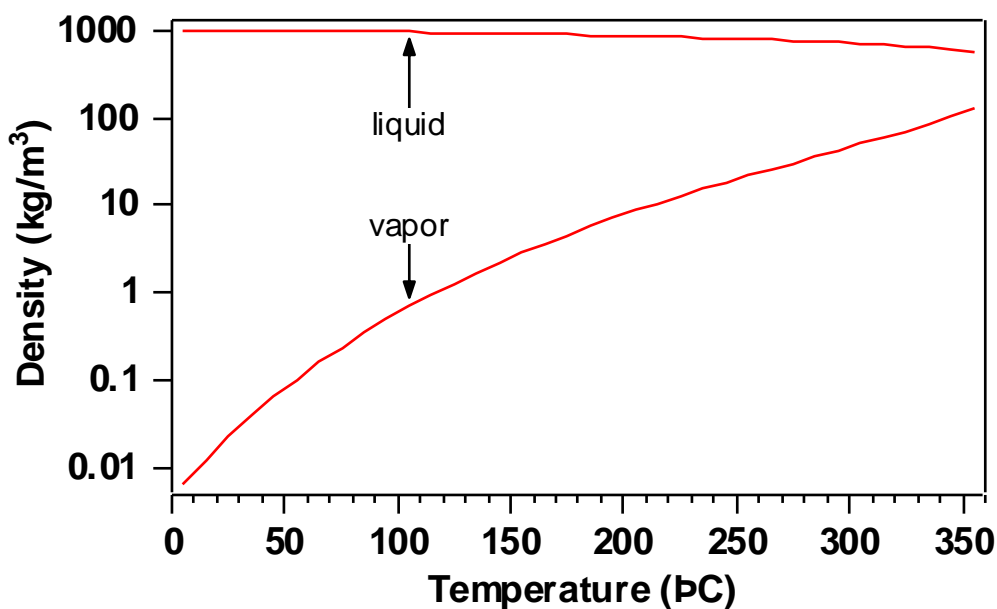


Figure 8.3 Liquid and vapor density along the saturation line.

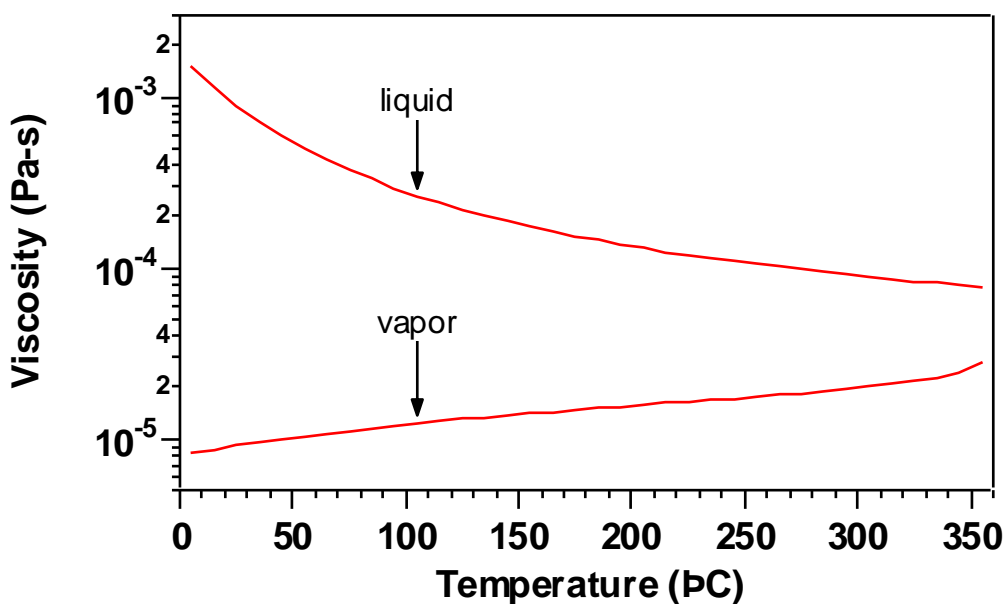


Figure 8.4 Liquid and vapor viscosity along the saturation line.

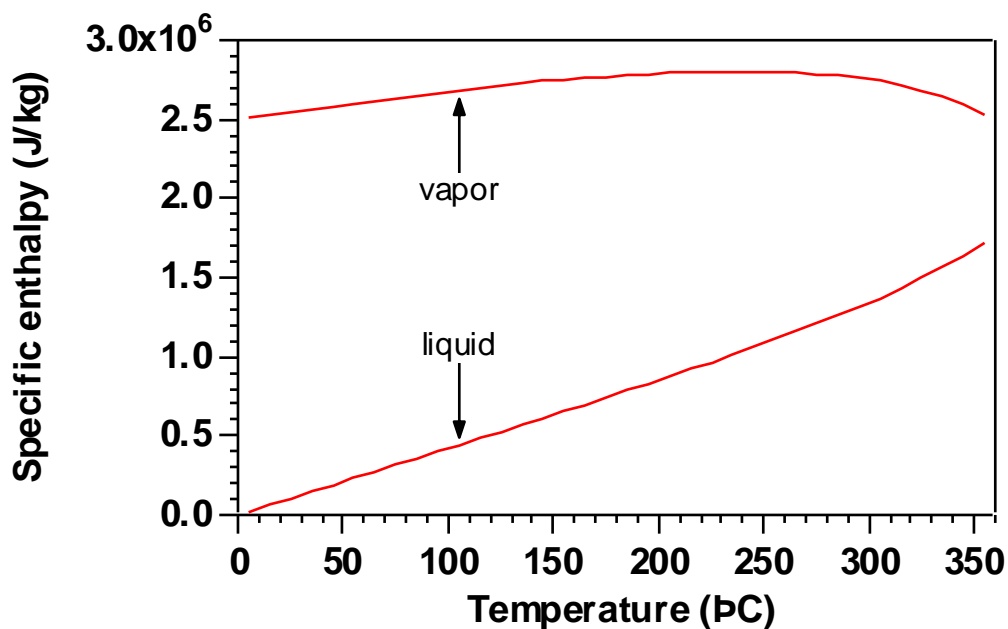


Figure 8.5 Liquid and vapor enthalpy along the saturation line.

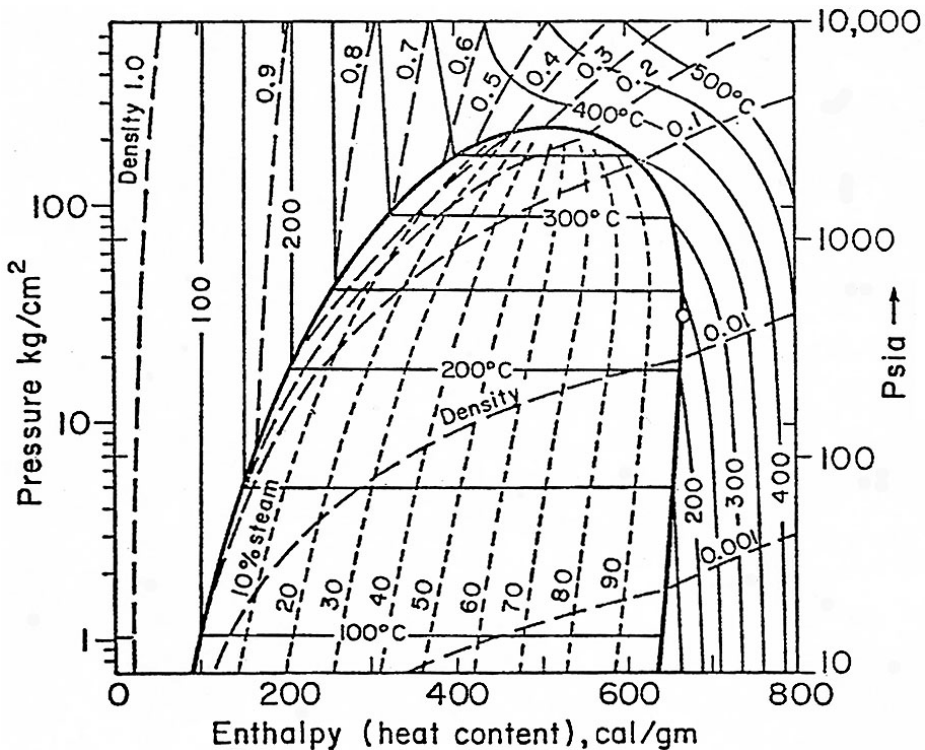


Figure 8.6. Pressure-enthalpy diagram for pure water and vapor, showing contours of equal temperature, density, and mass fractions of steam. Open circle indicates maximum enthalpy of saturated steam (from White et al., 1971).

8.2 Gases

Of fundamental importance in the study of gas behavior is the “ideal gas law,” written as

$$PV = nRT \quad (8.1)$$

Here n is the number of moles of the gas, i.e., the mass M of the gas divided by the molecular weight m of the gas expressed in grams, $n = M/m$. T is “absolute temperature” measured in degrees Kelvin ($T(K) = T(^{\circ}C) + 273.15$), and $R = 8.315 \text{ J/(mole } ^{\circ}\text{C)}$ is the universal gas constant. Eq. (8.1) says that at a fixed temperature, the pressure and volume of a fixed quantity of gas are inversely related, $V \propto 1/P$, and, furthermore, that the pressure of a given quantity of gas held in a fixed volume is proportional to absolute temperature. Empirically it is found that “real” gases obey Eq. (8.1) only approximately, and to better approximation at high temperatures and low pressures. The isothermal compressibility of an ideal gas can be calculated from Eq. (8.1) as

$$\kappa_T = -\frac{1}{V} \frac{\Delta V}{\Delta P} = \frac{1}{P} \quad (8.2)$$

i.e., it is simply given by the inverse of the pressure.

Many different enhancements to Eq. (8.1) have been developed for different chemical substances, especially in the petroleum industry which must deal with a great variety of gaseous and volatile fluids. Some of these equations are even capable of representing the phase change to liquid conditions which occurs at “low” temperatures and “high” pressures, exactly what is “high” or “low” depending on the chemical nature of the fluid under consideration. For geothermal applications, the most important gases are water vapor and carbon dioxide, but air, hydrogen sulfide, and noble gases may also be present. From a practical engineering viewpoint, for an accurate representation of gas properties it is most convenient to modify Eq. (8.1) in a way that preserves its structure. The “real gas law” is written, in analogy to Eq. (8.1),

$$PV = ZnRT \quad (8.3)$$

where $Z = Z(T, P)$ is the “real gas compressibility factor,” a function of temperature and pressure that can be regarded as a measure of the deviation from ideal gas behavior.

8.3 Phase Partitioning

When two fluid phases are present, non-condensable gases (NCGs) such as CO₂, H₂S, noble gases and many man-made chemical tracers, will partially dissolve in the liquid phase. Under ideal conditions, the mole fraction $x_{\text{aq}}^{\text{NCG}}$ that dissolves in the liquid phase is proportional to the partial pressure in the gas phase, a relationship that is known as “Henry’s law.”

$$P_{\text{NCG}} = K_h x_{\text{aq}}^{\text{NCG}} \quad (8.4)$$

The partitioning of a volatile tracer between water and steam is shown schematically in Fig. 8.7.

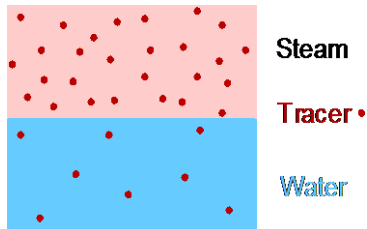


Figure 8.7. Phase partitioning of a volatile tracer.

The Henry’s coefficient K_h for dissolution of CO₂ in water is strongly dependent on temperature. Several different correlations developed for $K_h(T)$ are shown in Fig. 8.8. An early correlation developed by O’Sullivan et al. (1985) is accurate to within a few percent of experimental data in the temperature range of 40 °C ≤ T ≤ 330 °C, but becomes rather inaccurate at lower temperatures. The correlation developed by Battistelli et al. (1997) is accurate for 0 °C ≤ T ≤ 350 °C, and is used in the TOUGH2 simulator. It agrees well with another correlation developed by S. White (private communication, 1986).

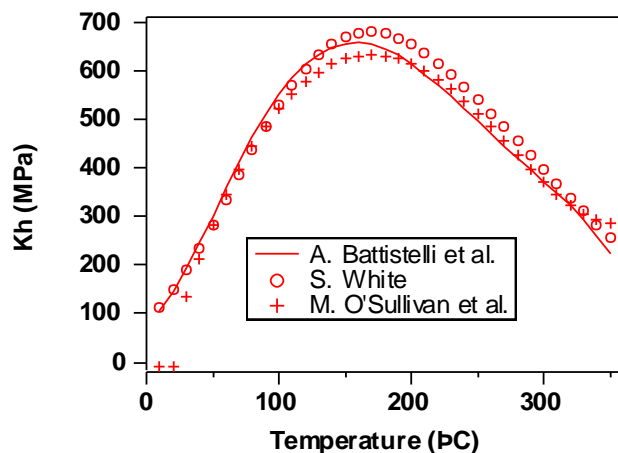


Figure 8.8. Henry’s law coefficients for dissolution of CO₂ in water.

8.4 Brines

Geothermal waters may contain considerable amounts of dissolved salts, such as NaCl. Salty aqueous fluids or “brines” have larger density and viscosity than pure water. They also have lower vapor pressure and lower solubility for non-condensable gases. Figs. 8.9-10 illustrate the dependence of density and viscosity on salt concentration for the most commonly encountered NaCl brines, based on the correlations developed by Battistelli et al. (1997).

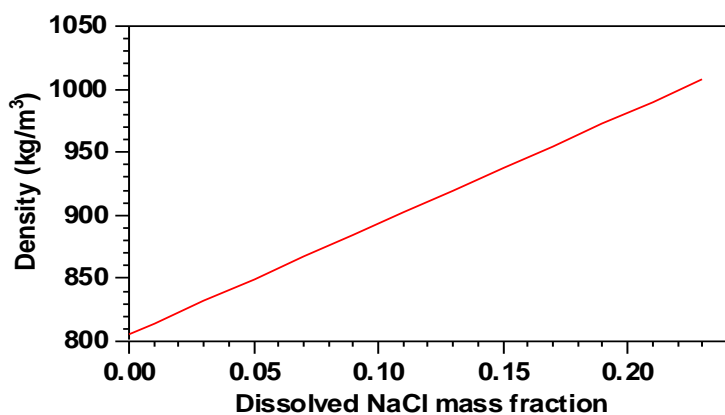


Figure 8.9. Brine densities at $T = 250 \text{ } ^\circ\text{C}$, $P = 100 \text{ bar}$.

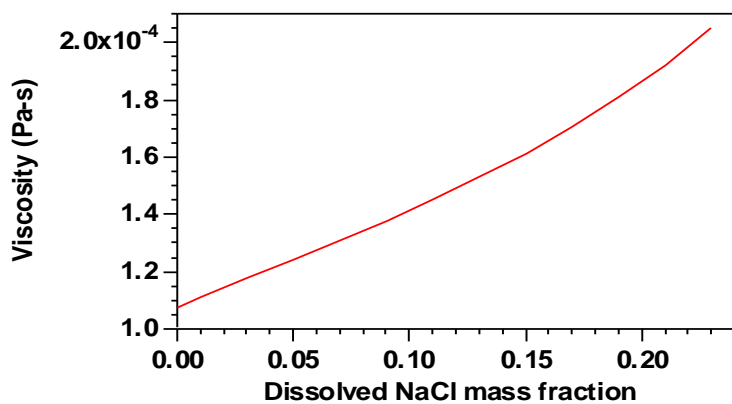


Figure 8.10. Brine viscosities at $T = 250 \text{ } ^\circ\text{C}$, $P = 100 \text{ bar}$.



LECTURE III: NUMERICAL MODELING OF GEOTHERMAL SYSTEMS

Geothermal reservoirs are dynamic systems that are driven by throughputs of fluid and heat. This is true under natural conditions, but rates of mass and energy transport are typically much larger in reservoirs that are being exploited. Fig. 9.1 illustrates some of the physical and chemical processes that take place in a producing geothermal field.

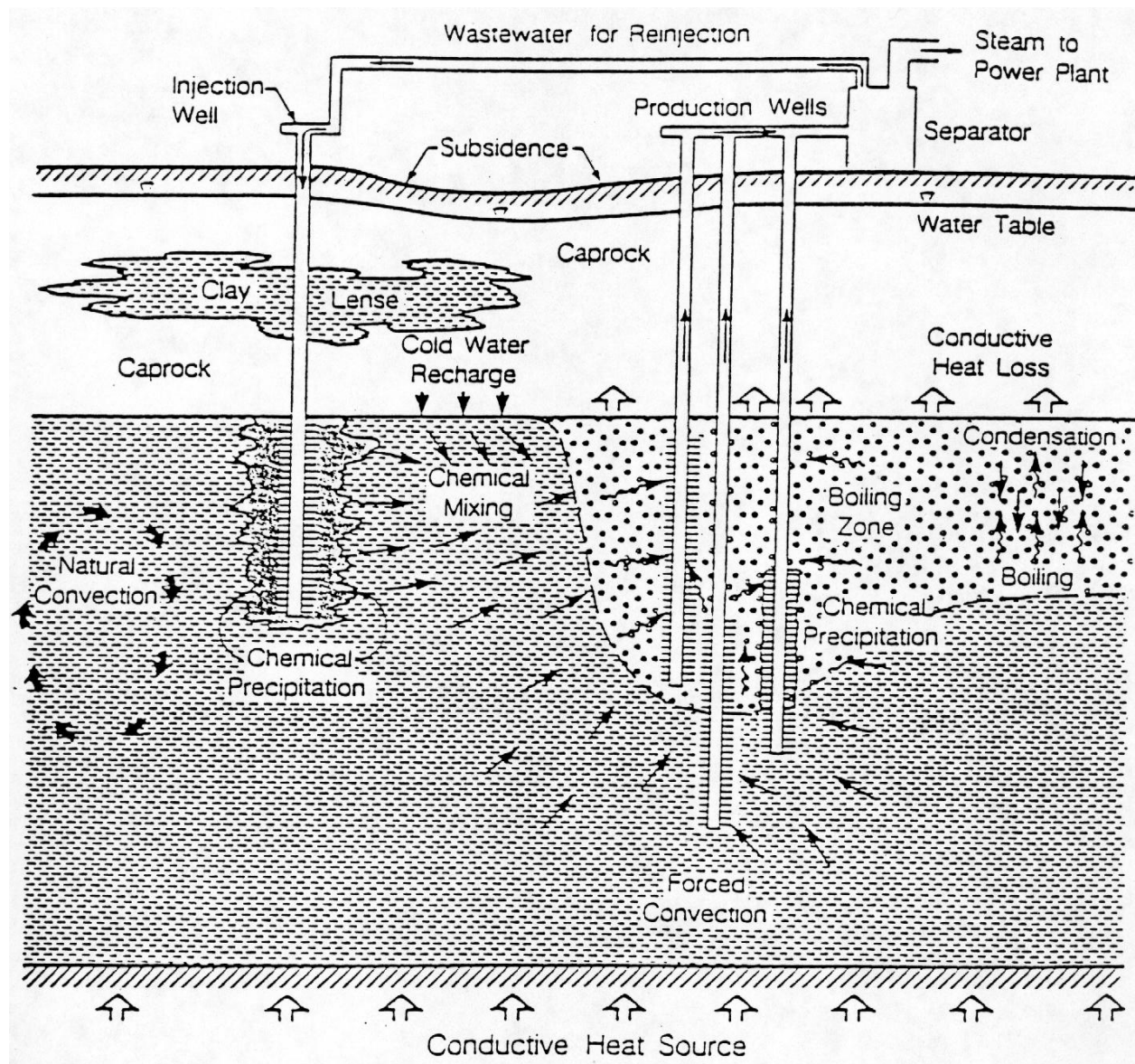


Figure 9.1. Schematic of physical and chemical processes occurring in a producing geothermal field (from Bodvarsson and Witherspoon, 1989).

9. Primer on Transport Processes

Before proceeding to a more detailed discussion of approaches and methodology for reservoir simulation, it is useful to briefly review some basic types of mass and energy transport processes. Three basic process types have been recognized, (a) advection, (b) diffusion, and (c) dispersion. Actual mass and energy transport processes described by the equations discussed in Sections 6 and 7 usually involve some combination of these.

Advection involves the translation of fluid parcels over time, as can be traced by solutes dissolved in the fluid. Suppose at some time t_0 we have a solute distribution given by $C_0(x)$, see Fig. 9.2. For a purely advective flow, the distribution at some later time t is identical to C_0 , except

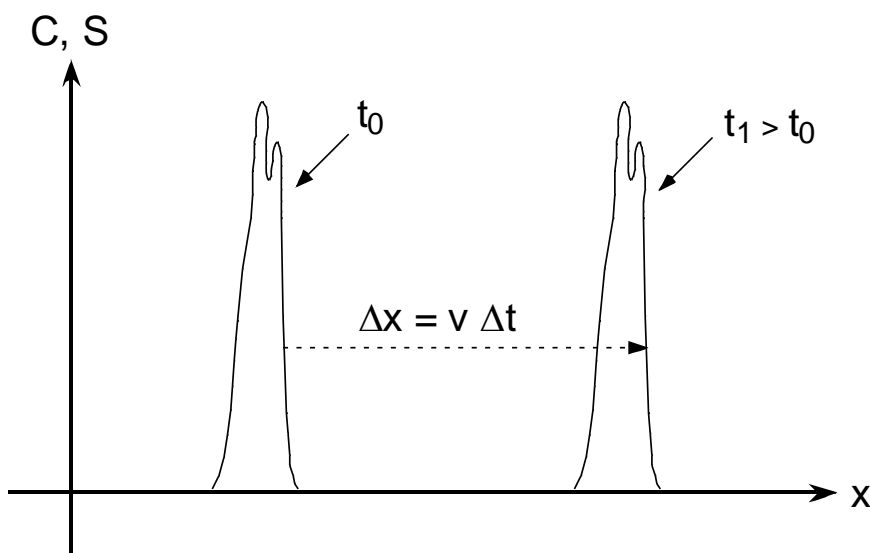


Figure 9.2. Illustration of a purely advective process in 1-D. $\Delta t = t_1 - t_0$ is a time interval.

everything is displaced by $\Delta x = v(t-t_0)$, where v is the flow velocity, so that $C(x, t) = C_0(x-v[t-t_0])$. Mathematically speaking, advective processes are described by a so-called “hyperbolic” partial differential equation (PDE), which involves only first-order derivatives in space and time.

$$\frac{\partial C}{\partial t} + v \frac{\partial C}{\partial x} = 0 \quad (9.1)$$

Diffusion arises from random motions on a molecular scale. Examples include heat conduction, molecular diffusion of solutes or gases, and the propagation of pressure disturbances in fluids. Diffusion tends to average out whatever spatial variations may be present initially, and to broaden initial distributions (Fig. 9.3). From a mathematical viewpoint, diffusion processes are

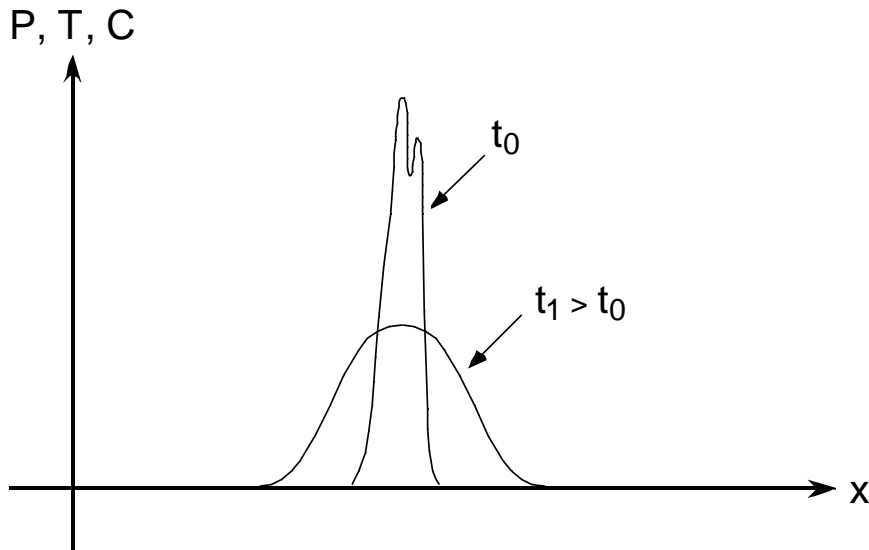


Figure 9.3. A diffusive process in 1-D.

described by a “parabolic” PDE which involves first-order time and second-order space derivatives. The prototype for this is the heat conduction equation,

$$\frac{\partial T}{\partial t} - D \frac{\partial^2 T}{\partial x^2} = 0 \quad (9.2)$$

where D is the diffusivity, which has units of m^2/s . Diffusion processes have the characteristic that the width of the distribution grows proportional to the square root of time. A perturbation applied locally to a diffusive system will over a time period t propagate a distance

$$x = \sqrt{Dt} \quad (9.3)$$

Eq. (9.3) is useful for estimating the range of influence of a diffusive process, but it must be kept in mind that diffusive profiles are characterized by broad distributions, not sharp fronts. “Small” amounts of the diffusing quantity will reach distances far greater than x estimated from Eq. (9.3).

Thermal diffusivity is given by $D = K/\rho c$, where K is thermal conductivity, ρ is specific density, and c is specific heat. For typical reservoir rocks, these parameters have values of $K \approx 2 \text{ W/m } ^\circ\text{C}$, $\rho \approx 2500 \text{ kg/m}^3$, and $c \approx 800 \text{ J/kg } ^\circ\text{C}$, so that thermal diffusivity is of order $D \approx 10^{-6} \text{ m}^2/\text{s}$. The penetration distances for heat conduction are then $x = 5.6 \text{ m}$ in 1 year, $x \approx 30 \text{ m}$ in 30 years.

The third fundamental transport process is dispersion, which arises from fluctuations in pore velocity due to irregular pore channels, presence of fractures, or heterogeneities of any other kind. Dispersion will cause an initially compact plume of solutes to change its shape in

more-or-less erratic fashion, see Fig. 9.4. A solute cloud (plume) as shown on the left of Fig. 9.4 may at some later time reside in an irregularly-shaped volume as shown on the right. The magnitude of the volume occupied by the solute will increase over time, but this tends to be a slow process driven primarily by molecular diffusion. The most dramatic and typically far more rapid change is in the shape of the plume. A theoretical approach originally proposed by Scheidegger (1954) and subsequently widely used in hydrology seeks to capture the growth of the volume in which solutes may be found in some average fashion, by treating dispersion in analogy to molecular diffusion. Scheidegger's dispersion model would predict that solute will occupy the lightly shaded elliptical region on the right of Fig. 9.4. Hydrogeological research during the last twenty years has shown that the diffusive analog to dispersion has serious shortcomings. It cannot properly predict the growth of the plume in longitudinal and transverse directions, and it tends to overestimate dilution effects. No alternative model of similarly broad scope has taken the place of the diffusive analog. In practical applications it is desirable to explicitly represent the heterogeneity that is causing the dispersion, although for many applications the diffusion model, if used carefully, can still provide useful answers.

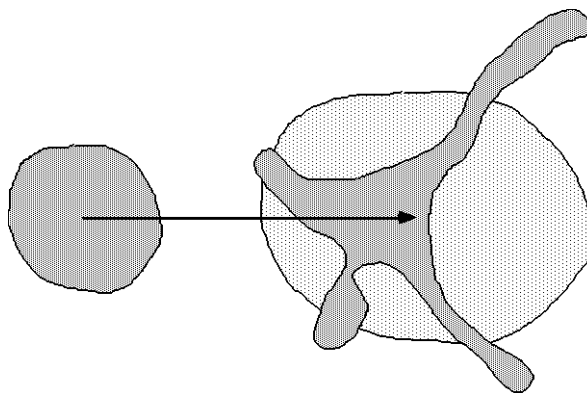


Figure 9.4. Schematic of solute dispersion. The compact solute plume shown on the left may at some later time occupy the irregular volume on the right. The lightly shaded region indicates the solute distribution that would be predicted from an approach that models dispersion in analogy to diffusion.

10. Overview of Reservoir Simulation

The aim of reservoir simulation is to construct a mathematical model of a reservoir, or of some hypothetical, idealized flow system that we wish to study, and to obtain quantitative numerical solutions for this model. In order to be able to devise a mathematical model, we need to

- identify and understand the basic physical and chemical processes operating in a reservoir;
- develop mathematical expressions (equations) for describing these processes;
- have information or make appropriate assumptions about the hydrogeologic parameters of the formation (such as permeability, porosity, etc.), including their spatial variation;
- have quantitative information about the relevant fluid properties (such as density, viscosity, enthalpy, vapor pressure, etc.), and their dependence on the thermodynamic conditions;
- have information or make appropriate assumptions about initial conditions throughout the system, and boundary conditions at all times at the outer boundary of the system;
- we also need to know the nature, location, and rates of sinks and sources.

For idealized and simplified systems and conditions, it is possible to solve mathematical models by analytical techniques. However, geothermal reservoir problems will in general feature irregular variations of thermodynamic conditions, fluid properties, and formation parameters, and operation of production and injection wells may occur in some time-varying fashion. Then no closed-form analytical solutions of the governing mass and energy balance equations are possible, and we must resort to numerical techniques.

The basic approach taken in numerical reservoir simulation involves “discretizing” the continuous space and time variables. Space discretization means that we break down or “partition” the volume of the system we are interested in into sub-volumes. Different shapes may be used, but from a practical viewpoint it is best to think of these sub-volumes as “bricks” (what mathematicians call “parallelepipeds”) or, in two dimensions, rectangles. The sub-volumes will be referred to as “volume elements” or “grid blocks.” We then set up mass balances (and for non-isothermal processes also energy balances), for each of the grid blocks. In reality, the thermodynamic conditions in a flow system may vary from point to point; by discretizing into finite-size grid blocks we approximate these point-to-point variations by means of averages in each grid block. Expressed differently, we assume that (approximate) thermodynamic equilibrium prevails “locally,” on the scale of a grid block. Time is also discretized into finite increments or “time steps” Δt . Suppose that at some given time t we know the thermodynamic conditions in all grid blocks. From this information we calculate the rates of mass (and energy) flow between grid blocks. We then allow these flows to proceed for

a time Δt and, using mass balances Eq. (6.1) and energy balances Eq. (7.7), we obtain new updated inventories of mass and energy in each grid block corresponding to time $t + \Delta t$. This process is repeated for as many time steps as desired, to obtain a prediction of thermodynamic conditions for a time period of interest.

Because thermodynamic conditions change during a time step, we initially only have information about the mass (and energy) flow rates corresponding to the beginning of the time step. The outcome at the end of the time step will depend on the manner in which the flow rates change. Often times it is necessary to apply an iterative procedure to solve for the changes during a time step.

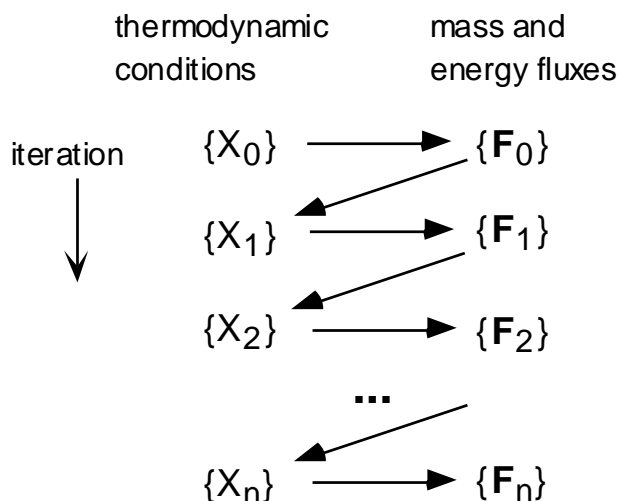


Figure 10.1. Iteration procedure for solution of mass and energy balances.

The discretization of space and time into finite-size intervals introduces inaccuracies, known as “space and time truncation errors,” which generally become smaller when discretization is refined.

11. Preparation of Input Data

The types of data needed to characterize a flow system and specify a simulation problem are summarized in Fig. 11.1. In addition to these data we also need fluid properties (see Sec. 8), which usually are provided internally in a reservoir simulation program. In practical applications of reservoir simulation, the most important parameters are the magnitude and spatial distribution of permeability and porosity; the temperatures, pressures, and vapor saturations of the reservoir fluids, and the location and rates of upflow and recharge. Typically these parameters are only incompletely known at the beginning of a simulation study, and one of the important objectives is then to determine them in a process known as “model calibration” or “history matching.” This involves making guesses for poorly constrained parameters, running a simulation, and comparing the outcome with field

observations, such as pressure and temperature distributions, changes in well flow rates and enthalpies, tracer returns, and others. Discrepancies between predicted and observed field characteristics and behavior will be noted, and parameters will be revised to try and reduce these discrepancies. Model calibration can be done as a trial-and-error process, using engineering judgment in making parameter estimations, or it can be automated using “inverse modeling” (Finsterle et al., 2000).

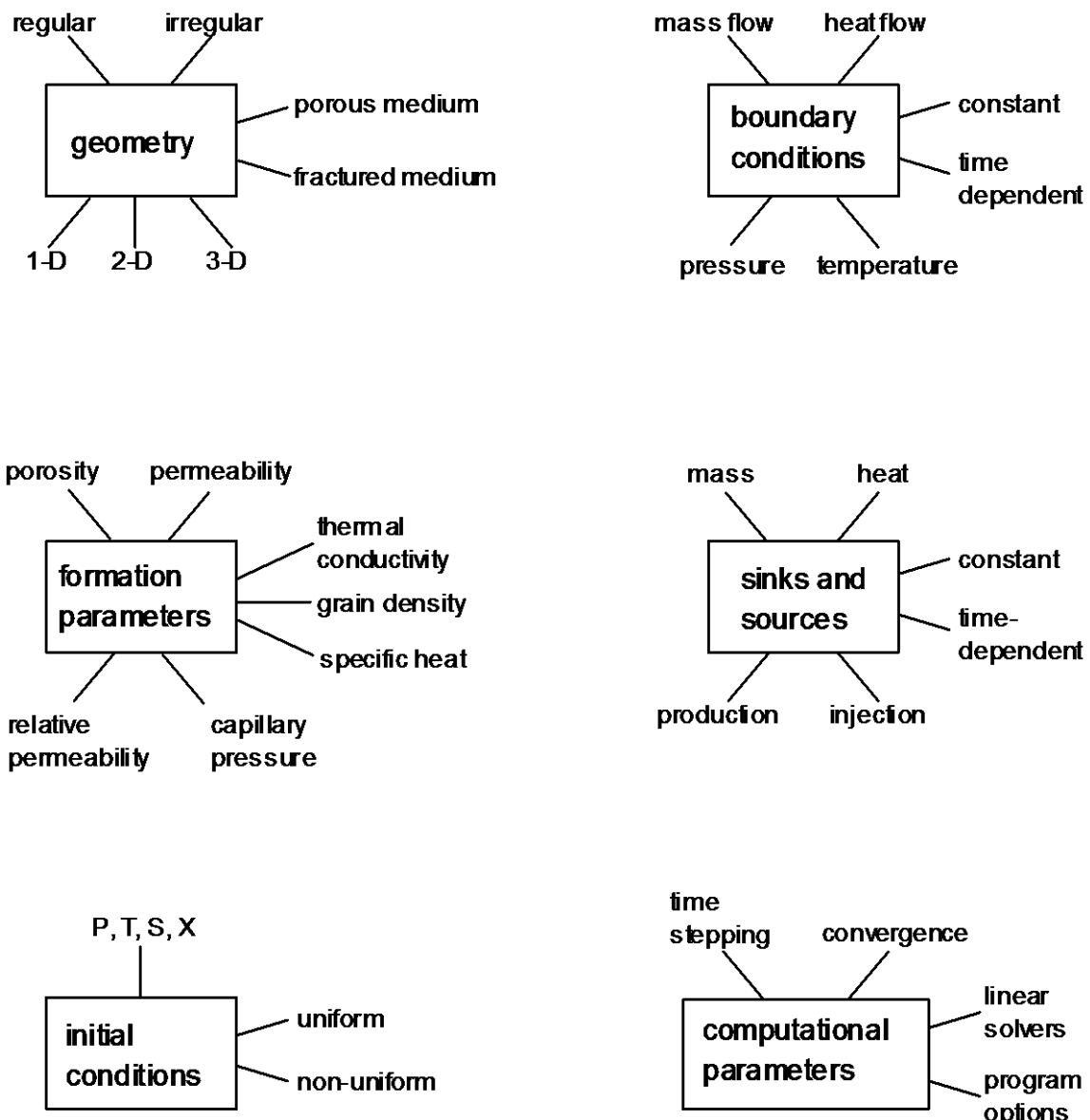


Figure 11.1. Data groups for a simulation problem.

Sometimes it is held that numerical simulations require a lot of data in order that useful results may be obtained. If the objective is to develop detailed forecasts of future well and reservoir behavior (flow rates, enthalpies, pressures, gas concentrations, etc.), then indeed the reliability of predictions depends on the detail and comprehensiveness of available information for the formations (permeability, porosity, characteristic curves, initial and

boundary conditions). In practice, much of this information is developed through “history matching.” More detailed observations made over a longer period of time provide more constraints for history matching and, if indeed history matching is successful, will permit more reliable forecasts. As a rule of thumb, it is often held that performance forecasts may be made for a period of time comparable to the period for which observations are available and have been matched by a reservoir model.

However, we wish to stress that reservoir simulators can also be usefully applied even in situations where only limited data are available. Uncertainties due to the paucity of data can be evaluated by examining a range of reservoir models and parametrizations that cover the range of uncertainties. Simplified models can be used to gain insight into reservoir behavior and flow mechanisms.

12. Grid Generation

Specification of the domain to be modeled and development of a computational grid have a large impact on the realism, accuracy, and potential usefulness of a reservoir model. The model domain should not be chosen too small, so that model behavior is not unduly affected by artificial boundary conditions. For example, specification of water inflow near producing wells, either by way of an explicit recharge rate or through constant pressure boundaries, can have a strong influence on predicted well behavior. It is desirable that the model domain extends a “large” distance beyond an actual or potential well field, so that fluid supply to the wells is governed by flow in the domain that is modeled, rather than by artificial or poorly known boundary conditions.

In addition to the question of the size of the model domain, very important issues relate to the size and shape of grid blocks. In order that accurate results may be obtained, grid blocks should be chosen “sufficiently small” so that variations in thermodynamic conditions within the grid block volume are modest. More specifically, in regions where thermodynamic conditions vary rapidly, as e.g. near production and injection wells, and near upflow and recharge zones, grid blocks should be chosen small.

The fundamental issue is to be able to calculate the flow (of heat, fluid, solute) across an interface between two grid blocks. To do this accurately, we should divide an interface into many small surface segments, know the gradient of the quantity driving the process (pressure, temperature, saturation, solute concentration) in all of the segments, also know the corresponding conductivities, and then apply the appropriate flux law to calculate flow rates in each segment. Total flow across the interface would be given by a summation over the individual segments.

In reality we do not have sufficient information for such a detailed evaluation. What we have is average values of thermodynamic parameters, that correspond to discrete nodal points (grid block centers). Gradients at interfaces need to be approximated from information available at these discrete nodal points. Actually, what is needed for most transport processes is not the entire gradient, but just the component perpendicular to the interface, the so-called “normal” component.

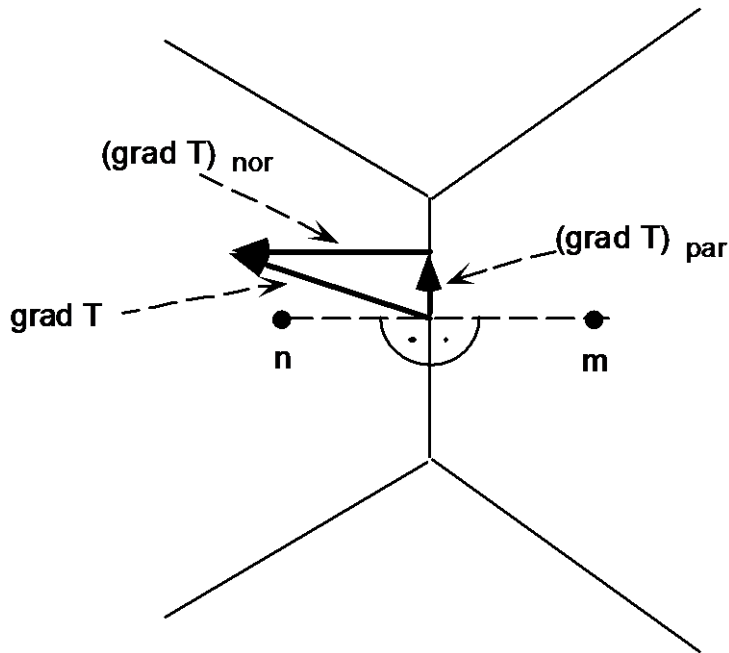


Figure 12.1. Components of average temperature gradient at the interface between grid blocks n and m.

As indicated by Fig. 12.1, an estimate of the normal component of the gradient can be obtained from data at the two neighboring grid blocks, provided the interface is oriented perpendicular to the nodal line connecting n and m. This leads to the concept of constructing grids from the perpendicular bisectors of nodal lines.

Additional constraints need to be observed. Consider the grid fragment shown in Fig. 12.2. The interface between nodal points n and m is given by the perpendicular bisector, yet it is intuitively obvious that knowledge of conditions at nodal points n and m may not provide a good estimate of the gradient at their common interface. Skewed angles should be avoided in grid design.

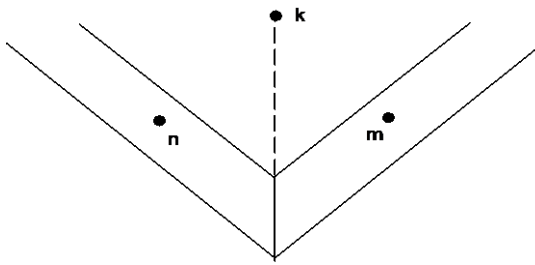


Figure 12.2. Portion of a grid with nodal points n, m, and k.

Another gridding issue is illustrated in Fig. 12.3. Here it is desired to refine the grid spacing in the central block, to be able to more accurately define the gradients driving flow. The reason for wanting to do this may be that there is a well located in the middle of the central grid block. It is clear that it is not possible to obtain the normal component of gradients at the sub-divided interfaces from parameters at two neighboring grid blocks. A more complex scheme is needed, where additional “interpolation nodes” are introduced (Pruess and García, 2000).

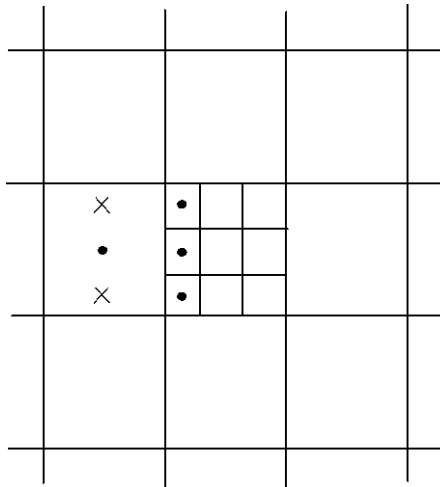


Figure 12.3. Local grid refinement. Nodal points are marked with solid circles, interpolation nodes are marked as an x.

From these examples it is clear that grid design requires careful thought and scrutiny, as it can provide a potentially major source of errors or inaccuracies. For practical simulation studies it is recommended to include some evaluation of grid sensitivity. One way to accomplish this is to solve the same flow problem on different grids and compare results.

Mesh generation can be greatly simplified by exploiting actual or approximate symmetries of a flow system. This allows far more efficient and potentially more accurate simulations. A case in point is flow to or from a well, which in “sufficient” proximity to the well may approximate radial symmetry, meaning that at any given time, parameters such as

pressure, temperature, saturation, etc. depend only on distance R from the well, and possibly also on depth Z (see Fig. 12.4).

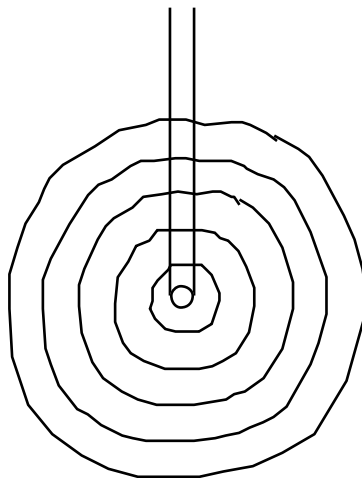


Figure 12.4. For radial symmetry, contour lines of pressure, temperature, etc. form concentric circles around the well, providing a natural grid system.

Radial symmetry may be violated by heterogeneities of the flow system, such as fractures, and at any rate will not hold for “large” space and time scales, where boundaries and large-scale variability of the flow system will come into play. On the other hand, for the analysis of well tests which sample only a limited reservoir volume over a limited period of time, perhaps of order 100 m and hours to days, idealization of the flow system as radially symmetric may be entirely adequate. It may even be possible to neglect Z -dependence and approximate the flow system as 1-D radial. The gain in efficiency and accuracy from such geometric simplifications can be appreciated by comparing gridding requirements between 1-D radial and 3-D Cartesian grids. Let us suppose we need to consider flow within 1 km distance from a well. If we use a grid spacing of 10 m, discretization of a $2 \times 2 \text{ km}^2$ region requires $200 \times 200 = 40,000$ grid blocks. If reservoir thickness is 500 m, we need 50 grid layers, for a total of 2,000,000 grid blocks. The same level of discretization in a 1-D radial model requires $1,000 / 10 = 100$ blocks. The 3-D model is at the limits of what can be done with a state-of-the-art massively parallel supercomputer, whereas the radial model is an easy problem on a PC. Clearly, in the 1-D radial model we can afford considerably finer grid spacing for a more accurate solution (provided radial symmetry is approximately valid), yet realize enormous savings in computing time. Radially symmetric models are also very useful for “generic” studies, to investigate flow mechanisms.

Another idealization that is useful for studying reservoir mechanisms is the five-spot model, which consists of a regular pattern of production and injection wells placed at the corners and centers of a quadrangle, respectively (see Fig. 12.5). The injection well may be absent. In actual geothermal reservoirs, wells are seldom sited with anything approaching the regularity of Fig 12.5, and even if they were, symmetry would be violated by the fact that the

well field is finite and does not continue the pattern indefinitely. Furthermore, wells would rarely operate all at the same rates, which again would violate symmetry. In spite of these limitations, a simplified five-spot geometry provides a very convenient means for studying production and injection behavior, and gaining an understanding of flow mechanisms. The chief advantage is that only 1/8 of a single five-spot needs to be modeled, shown by the gridded triangle in Fig 12.5, because the symmetry means that the boundaries of that triangle are “no flow” boundaries.

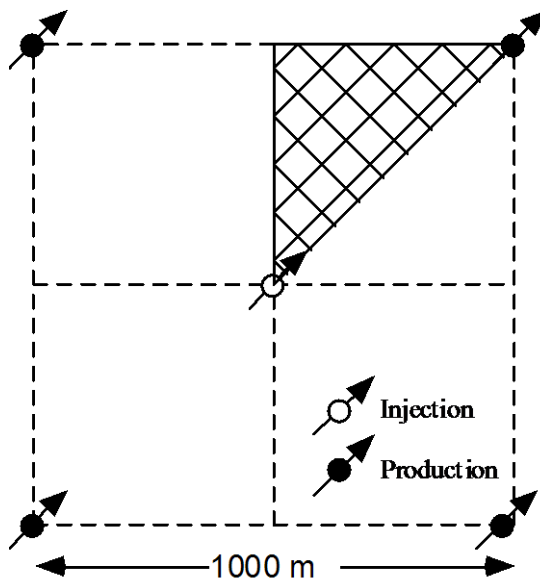


Figure 12.5. Five-spot well pattern with grid for modeling a 1/8 symmetry domain

Fig. 12.6 gives an areal view of the kind of grid that might be used for a field simulation study. Often it will be necessary to go to a 3-D model and include several layers, each of which would have the same discretization as shown in Fig. 12.6. Discretization is finer near the wells, to better resolve variations in thermodynamic conditions, while coarser grid spacing is employed at larger distance. For more accurate representation of near-well behavior, it is also possible to embed a radial grid within grid blocks containing wells. As mentioned before, it is important that the model domain be specified large enough so that simulated behavior is not unduly influenced by artificial boundary conditions close to the well field.

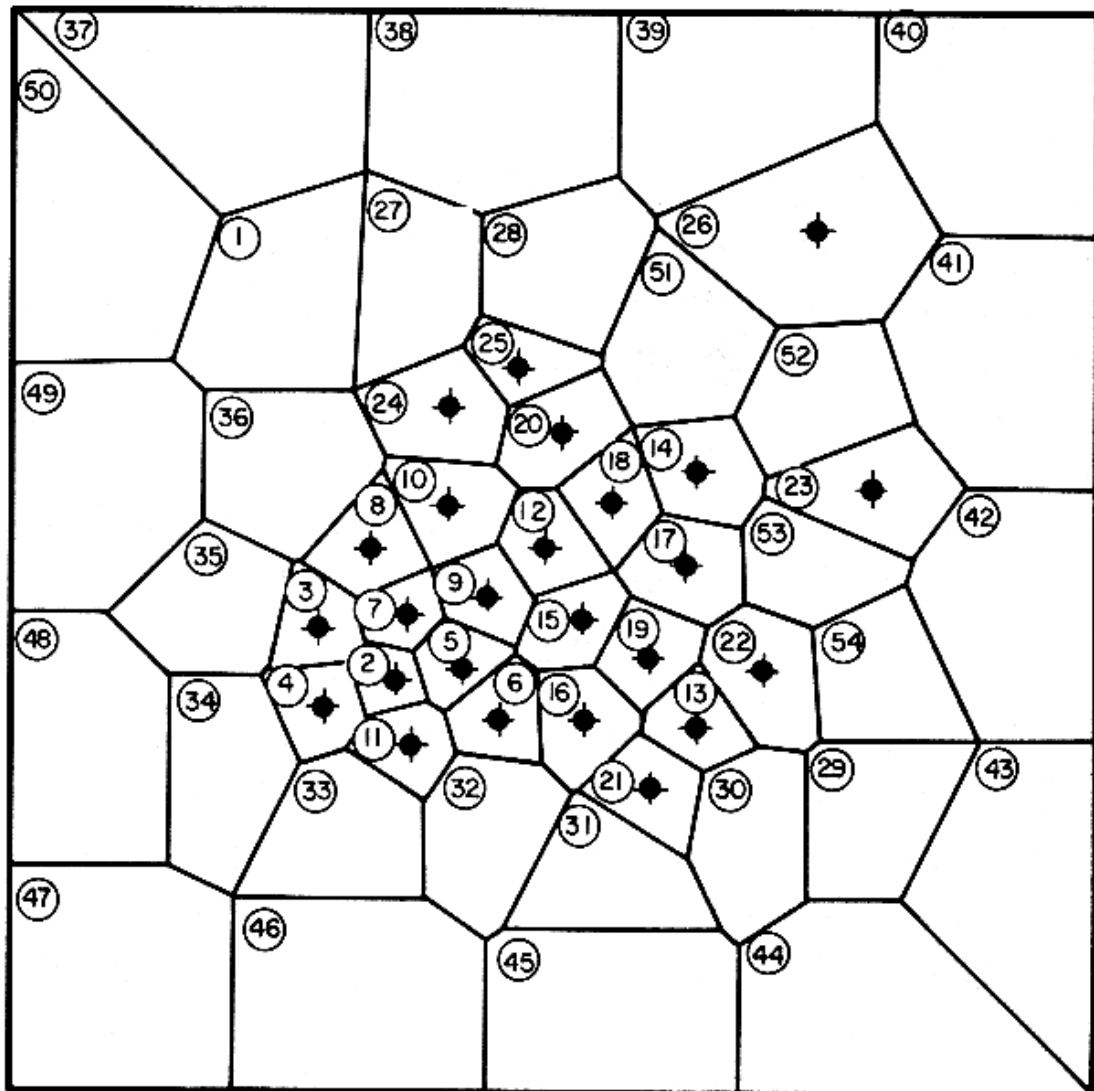


Figure 12.6. Areal view of computational grid for the Olkaria, Kenya geothermal field
(from Bodvarsson et al., 1985).

Fig. 12.7 shows a conceptual model for water injection into a superheated vapor zone in a vapor-dominated reservoir as a simplified 2-D vertical section model. Two grid designs which have been used to investigate the behavior of injection plumes in vapor zones are shown in Fig. 12.8.

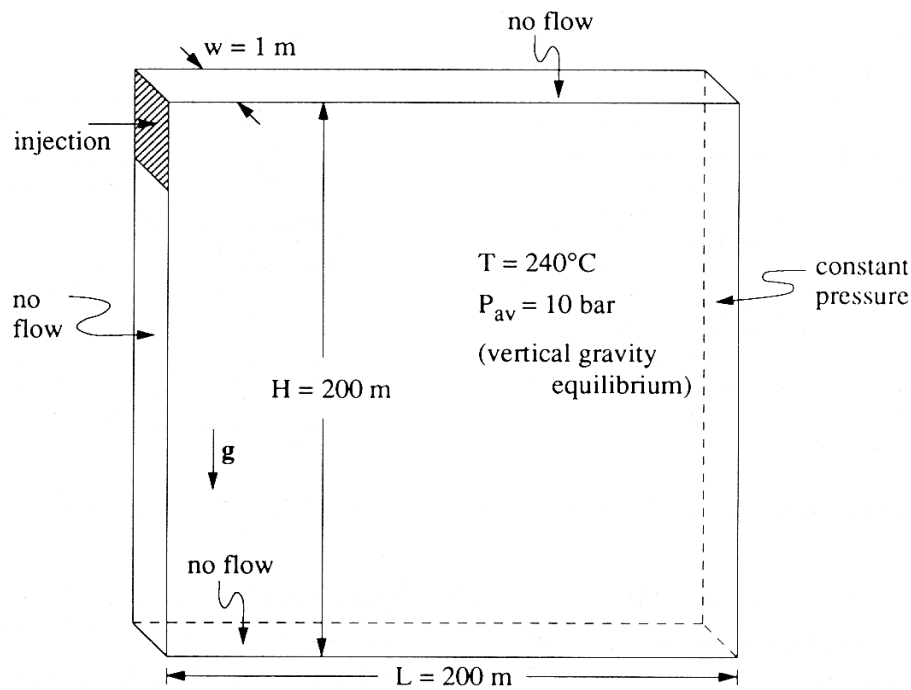


Figure 12.7. Idealized flow system used for studying water injection into a vapor-dominated reservoir (after Pruess, 1991).

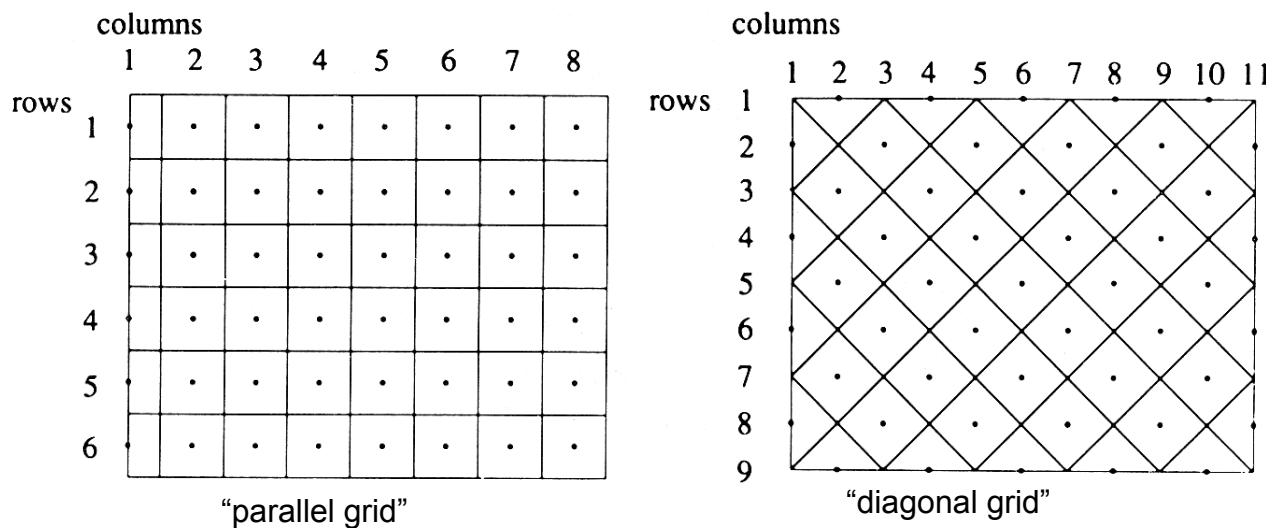


Figure 12.8. "Parallel" and "diagonal" grids for a 2-D vertical section (after Pruess, 1991).

As an example of the complex gridding that may be employed in reservoir studies, Fig. 12.9 shows a grid used for simulating hydrothermal processes during large-scale heater testing at the proposed nuclear waste repository at Yucca Mountain, Nevada. Small grid blocks are used to resolve detail in regions with strong spatial variability, while coarser blocks are used where gradients are expected to be small. The domain is chosen large enough so that artificial boundary effects are avoided. Further discussion of gridding will be given in Sec. 13 for fractured media, and in specific simulation problems discussed below.

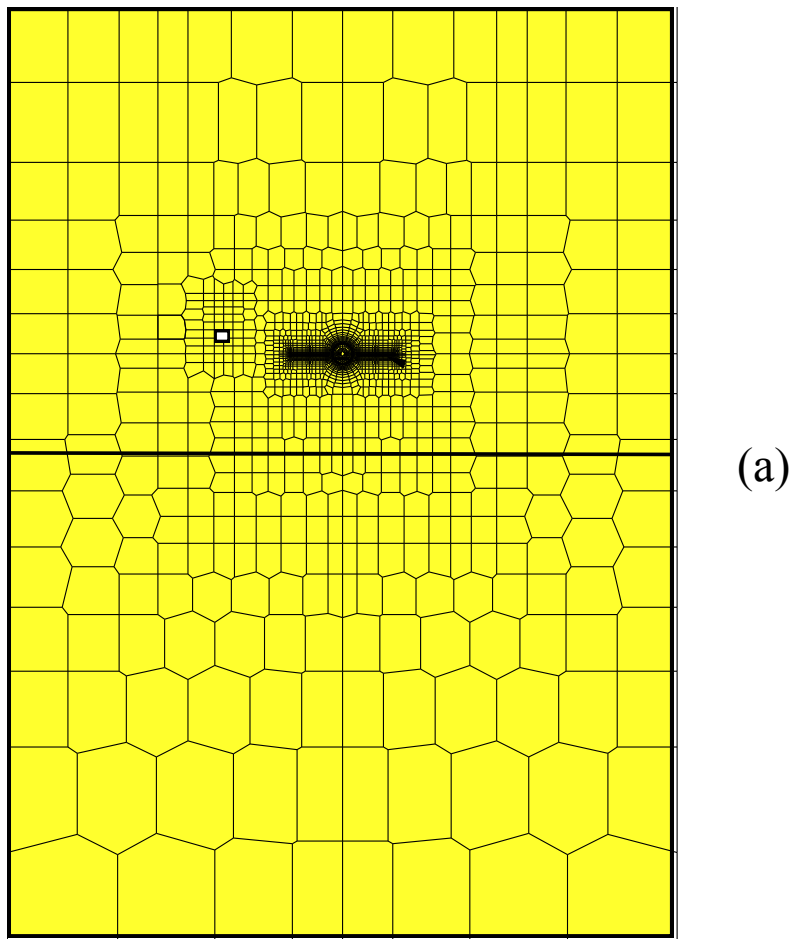


Figure 12.9. 2-D vertical section grid for modeling hydrothermal processes at Yucca Mountain, Nevada, in three views from global (a) to detailed (b and c) (from Birkholzer and Tsang, 1997).

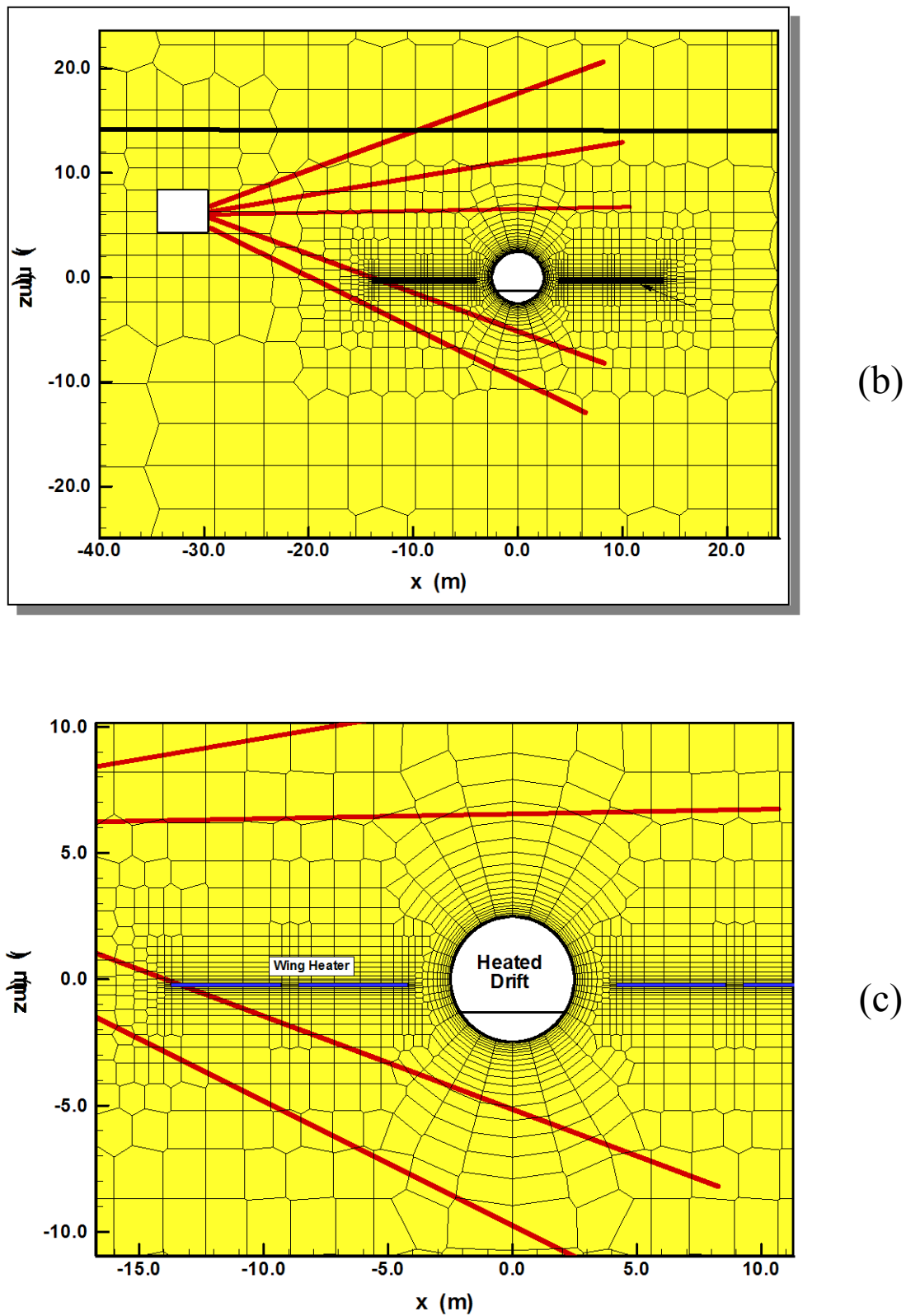


Figure 12.9. (continued) 2-D vertical section grid for modeling hydrothermal processes at Yucca Mountain, Nevada, in two more detailed views (from Birkholzer and Tsang, 1997).

13. Flow in Fractured Media

Most geothermal reservoirs are situated in fractured rock. Global fluid flow occurs primarily through a network of highly permeable interconnected fractures, while rocks of low permeability provide conductive heat supply, and may also participate in fluid flow locally. Typical tasks that a reservoir engineer may be called upon involve interpretation of well tests in fractured reservoirs, analysis of heat sweep during cold water injection (heat transfer from matrix rocks to fluids flowing in the fractures), and design and analysis of tracer tests. Different approaches are available to model flow in fractured media. The selection of the approach to be used in a particular study depends on the physical characteristics of the reservoir (parameters such as fracture spacing and connectivity, permeability of the matrix rocks), on the flow processes to be modeled (fluid production, injection, tracer migration), and on the available data and objectives of the study.

The simplest approach for modeling flow in fractured media is known as the “effective continuum method,” or ECM. In this approach, the reservoir is modeled as a single porous medium, and properties of the medium are chosen in such a way as to approximately represent the properties of a fractured porous medium. For example, in a fractured two-phase reservoir, the matrix blocks may have a rather large water saturation, yet the water does not flow (much) in the matrix blocks because of their low permeability. Instead, fluid production from the fractures induces a pressure drop which causes boiling of water in the matrix blocks, discharging vapor into the fractures. Such a process may be approximated by modeling the reservoir as a porous medium with large irreducible water saturation.

Another approach that is very simple conceptually involves explicit modeling of fractures, by including a region of large areal extent and small width, with appropriate hydrogeologic parameters, into the definition domain of a flow system. This approach is usually applicable only to studies of fluid and heat flow in idealized settings, because fractures in geothermal reservoirs are too numerous to allow for explicit representation. Occasionally, though, if we are dealing with a major fracture or fault zone, an explicit representation may be viable and the method of choice.

The most widely used approach for modeling flow in fractured media is the double-porosity concept that was first proposed by Barenblatt et al. (1960) and popularized by Warren and Root (1963). This concept is illustrated in Fig. 13.1. Matrix blocks of low permeability are embedded in a network of interconnected fractures. Global flow in the reservoir occurs only through the fracture system, which is described as an effective porous continuum. Rock matrix and fractures may exchange fluid (or heat) locally by means of “interporosity flow,” which is driven by the difference in pressures (or temperatures) between matrix and fractures. Warren and Root approximated the interporosity flow as being quasi-steady, with rate of matrix-fracture interflow proportional to the difference in (local) average pressures.

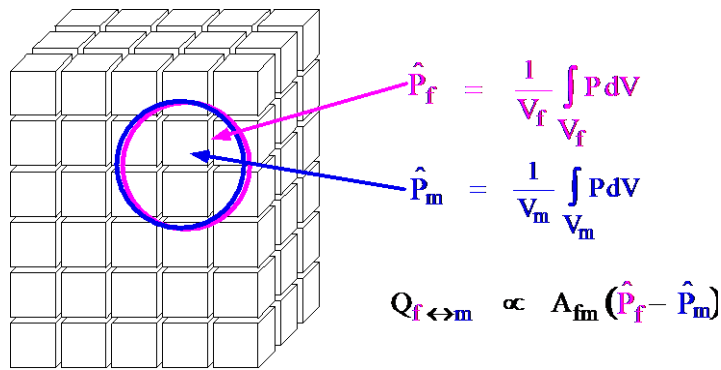


Figure 13.1. Idealized double porosity model of a fractured porous medium.

The quasi-steady approximation is applicable to isothermal single-phase flow of fluids with small compressibility, where pressure diffusivities are large, so that pressure changes in the fractures penetrate quickly deep into the matrix blocks. However, for multiphase flows, or coupled fluid and heat flows, the transient periods for interporosity flow can be very long (tens of years). In order to accurately describe such flows it is necessary to resolve the driving pressure, temperature, and mass fraction gradients at the matrix/fracture interface. In the method of “multiple interacting continua” (MINC; Pruess and Narasimhan, 1982, 1985), resolution of these gradients is achieved by appropriate subgridding of the matrix blocks, as shown in Fig. 13.2. The MINC concept is based on the notion that changes in fluid pressures, temperatures, phase compositions, etc. due to the presence of sinks and sources (production and injection wells) will propagate rapidly through the fracture system, while invading the tight matrix blocks only slowly. Therefore, changes in matrix conditions will (locally) be controlled by the distance from the fractures. Fluid and heat flow from the fractures into the matrix blocks, or from the matrix blocks into the fractures, can then be modeled by means of one-dimensional strings of nested grid blocks, as shown in Fig. 13.2.

In general it is not necessary to explicitly consider subgrids in all of the matrix blocks separately. Within a certain reservoir subdomain (corresponding to a finite difference grid block), all fractures will be lumped into continuum # 1, all matrix material within a certain distance from the fractures will be lumped into continuum # 2, matrix material at larger distance becomes continuum # 3, and so on. Quantitatively, the subgridding is specified by means of a set of volume fractions VOL(j), $j = 1, \dots, J$, into which the primary porous medium grid blocks are partitioned.

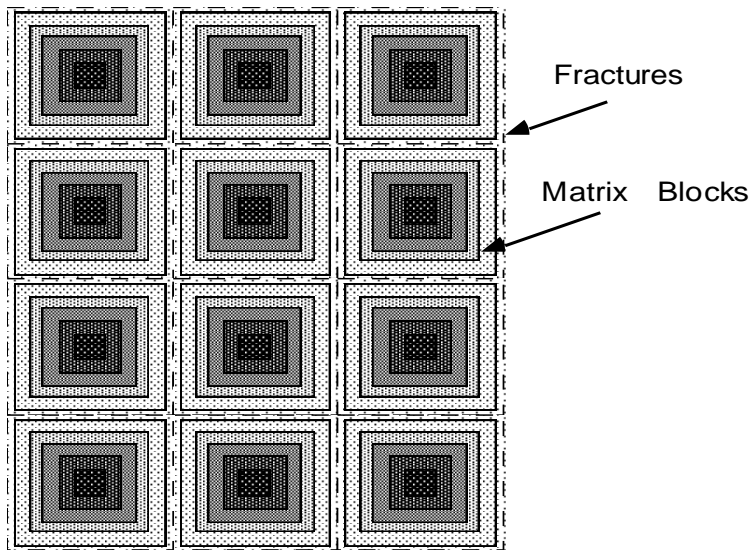


Figure 13.2. Subgridding in the method of "multiple interacting continua" (MINC).

The MINC-process in the MESHMAKER module of TOUGH2 operates on the element and connection data of a porous medium mesh to calculate, for given data on volume fractions, the volumes, interface areas, and nodal distances for a secondary fractured medium mesh. The information on fracturing (spacing, number of sets, shape of matrix blocks) required for this is provided by a “proximity function” PROX(x) which expresses, for a given reservoir domain V_o , the total fraction of matrix material within a distance x from the fractures. If only two continua are specified (one for fractures, one for matrix), the MINC approach reduces to the conventional double-porosity method. Full details are given by Pruess (1983).

Figure 13.3 shows a schematic of a MINC grid for modeling radial flow in a fractured reservoir. The MINC-method as implemented in TOUGH2 can also describe global matrix-matrix flow. The most general approach, often referred to as “dual permeability,” allows global flow in both fracture and matrix continua (Fig. 13.4). It is also possible to permit matrix-matrix flow only in the vertical direction. For any given fractured reservoir flow problem, selection of the most appropriate gridding scheme must be based on a careful consideration of the prevailing physical and geometric conditions of flow. The MINC approach is not applicable to systems in which fracturing is so sparse that the fractures cannot be approximated as a continuum.

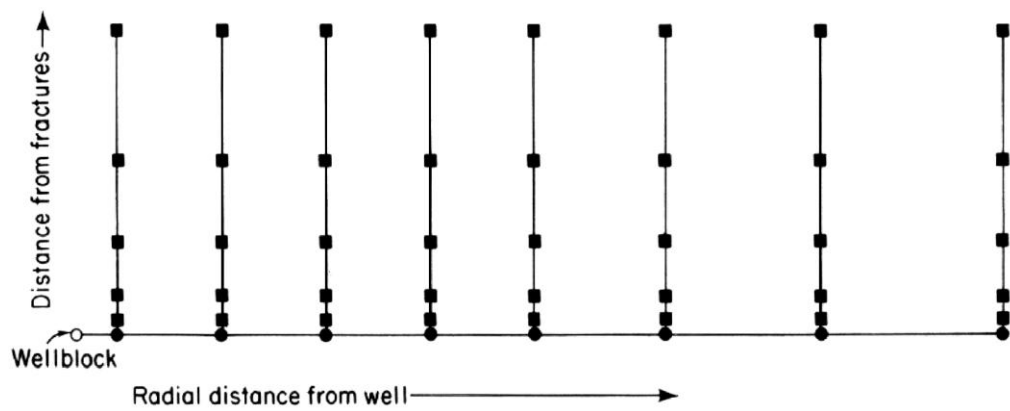


Figure 13.3. Schematic of MINC grid for modeling radial flow in a fractured reservoir (from Pruess and Narasimhan, 1982).

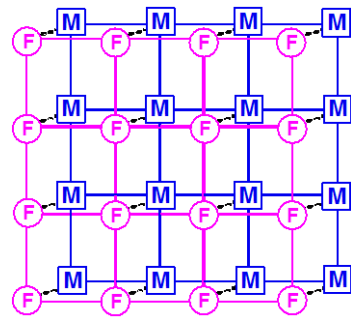


Figure 13.4. Flow connections in the “dual permeability” model. Global flow occurs between both fracture (F) and matrix (M) grid blocks. In addition there is F-M interporosity flow.



LECTURE IV: GEOTHERMAL RESERVOIR BEHAVIOR

14. Response to Fluid Production and Injection

Reservoir simulation can be applied to analyze flow to and from individual wells, or to model the behavior of an entire reservoir. It can also be used to investigate the behavior of simplified, hypothetical flow systems, where it can serve as a tool to identify flow mechanisms and understand reservoir dynamics. We will first discuss applications of numerical simulation on the scale of individual wells, and then examine approaches to field-wide modeling.

14.1 Production from a Two-Phase Reservoir with Dissolved Solids and Non-Condensable Gas

Fundamental to the understanding of reservoir response to fluid production is the classical “Theis solution” (Theis, 1935) for the pressure response of a well to fluid production at constant rate. This solution applies for the simplified conditions of 1-D radial flow of a single-phase fluid of small and constant compressibility in a homogeneous porous medium under isothermal conditions. It applies to fluid injection as well as production, and forms the basis for well testing techniques to determine reservoir parameters (Grant, Donaldson and Bixley, 1982; Bodvarsson and Witherspoon, 1989).

In many geothermal applications various complications come into play, including non-isothermal flow, fracture-matrix interactions, and boiling and condensation phenomena. Numerical simulation is a very useful tool for modeling and predicting reservoir response under these more complicated conditions.

As an example of a simulator application to fluid production, we present here one of the sample problems from the TOUGH2 user’s guide (Pruess et al., 1999), which uses the EWASG fluid property module (Battistelli et al., 1997) to examine production from a hypothetical geothermal reservoir with high salinity and CO₂. A single well produces at a constant rate of 65 kg/s from an infinite-acting reservoir in a 1-D radial flow geometry (Fig. 14.1). The reservoir is in two-phase conditions initially, with uniform initial conditions of P = 60 bar, T = 275.55 °C. Other problem parameters are given in the TOUGH2 input file (Fig. 14.2). Problem specifications made with SELEC-data include: no vapor pressure lowering (IE(10) = 0), a tubes-in-series model for permeability reduction from precipitation (IE(11) = 3), full dependence of thermophysical properties on salinity (IE(14) = 0), Michaelides’ correlation for brine enthalpy (IE(15) = 0), and CO₂ as non-condensable gas (IE(16) = 2).

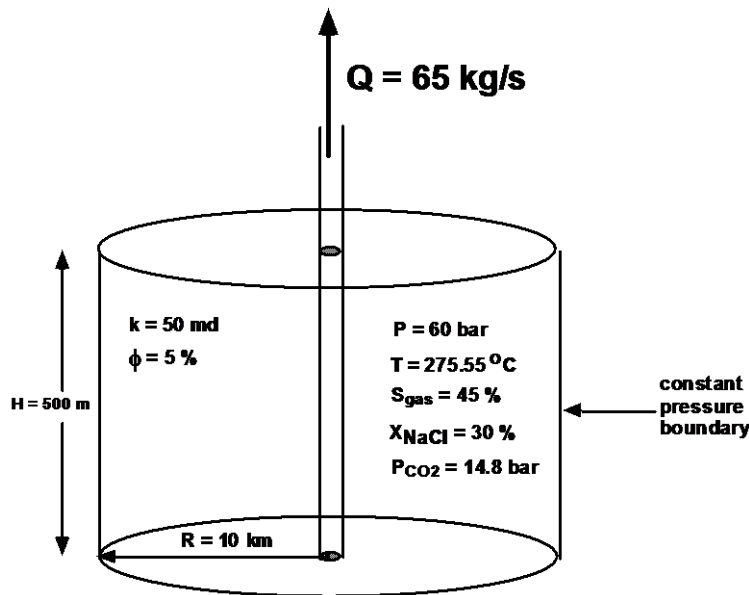


Figure 14.1. Illustration of 1-D radial model.

Fluid withdrawal causes pressures to drop near the production well. Boiling of reservoir fluid gives rise to dilution of CO₂ in the gas phase and to increased concentrations of dissolved NaCl, which begins to precipitate when the aqueous solubility limit is reached. As the boiling front recedes from the well, solid precipitate fills approximately 10 % of the original void space (see Fig. 14.3), causing permeability to decline to approximately 28 % of its original value.

Specifications of this problem (1-D radial geometry, uniform initial conditions, constant well rate) were chosen so that a similarity solution would be applicable, which should depend on radius R and time t only through the similarity variable $x = R^2/t$ (O'Sullivan, 1981). This similarity property should hold even when all complexities of two-phase flow with nonlinear relative permeabilities, CO₂ exsolution effects, salt precipitation, and associated porosity and permeability effects are taken into account. The agreement between results for two different times (5×10^5 and 2×10^6 seconds) when plotted as a function of the similarity variable shows that the similarity property holds very accurately for all thermodynamic variables (Fig. 14.3). "Solid saturation" in Fig. 14.3 denotes the fraction of pore space that is filled with solid precipitate.

```

*rhbc* - 1-D radial flow problem for EWASG, with NaCl and CO2
MESHMAKER1----*----2----*----3----*----4----*----5----*----6----*----7----*----8
RZ2D
RADII
 1
 5.
EQUID
 1          2.
LOGAR
 50          1.E2
LOGAR
 20          1.E3
EQUID
 1          0.0
LAYER---1----*----2----*----3----*----4----*----5----*----6----*----7----*----8
 1
 500.

ROCKS---1----*----2----*----3----*----4----*----5----*----6----*----7----*----8
POMED   2      2600.       .05    50.e-15    50.e-15    50.e-15      2.0    1000.0
      3      .30       .05
      1          1.

SELEC---2----3----4----5----6----7----8----9----10---11---12---13---14---15---16
 1
 1          .8       .8
      .... IE(16) = 2 chooses CO2 .....
MULTI---1----*----2----*----3----*----4----*----5----*----6----*----7----*----8
 3      4      3      6
START---1----*----2----*----3----*----4----*----5----*----6----*----7----*----8
----*----1--MOP:123456789012345678901234----*----5----*----6----*----7----*----8
PARAM---1----*----2----*----3----*----4----*----5----*----6----*----7----*----8
 1 100      100100 3000000002 40 0 3
      2.e6       -1.
      1.E4
      1.E-5     1.E00
      60.e5
      .30
      1.E-7     10.45
      275.55
TIMES---1----*----2----*----3----*----4----*----5----*----6----*----7----*----8
 1      1
 5.e5
RPCAP---1----*----2----*----3----*----4----*----5----*----6----*----7----*----8
 3      .30       .05
 1          1.
INCON---1----*----2----*----3----*----4----*----5----*----6----*----7----*----8
GENERAL---1----*----2----*----3----*----4----*----5----*----6----*----7----*----8
A1  1wel 1
      MASS      -65.

ENDCY---1----*----2----*----3----*----4----*----5----*----6----*----7----*----8

```

Figure 14.2. TOUGH2/EWASG input data for constant-rate production from a 1-D cylindrical reservoir.

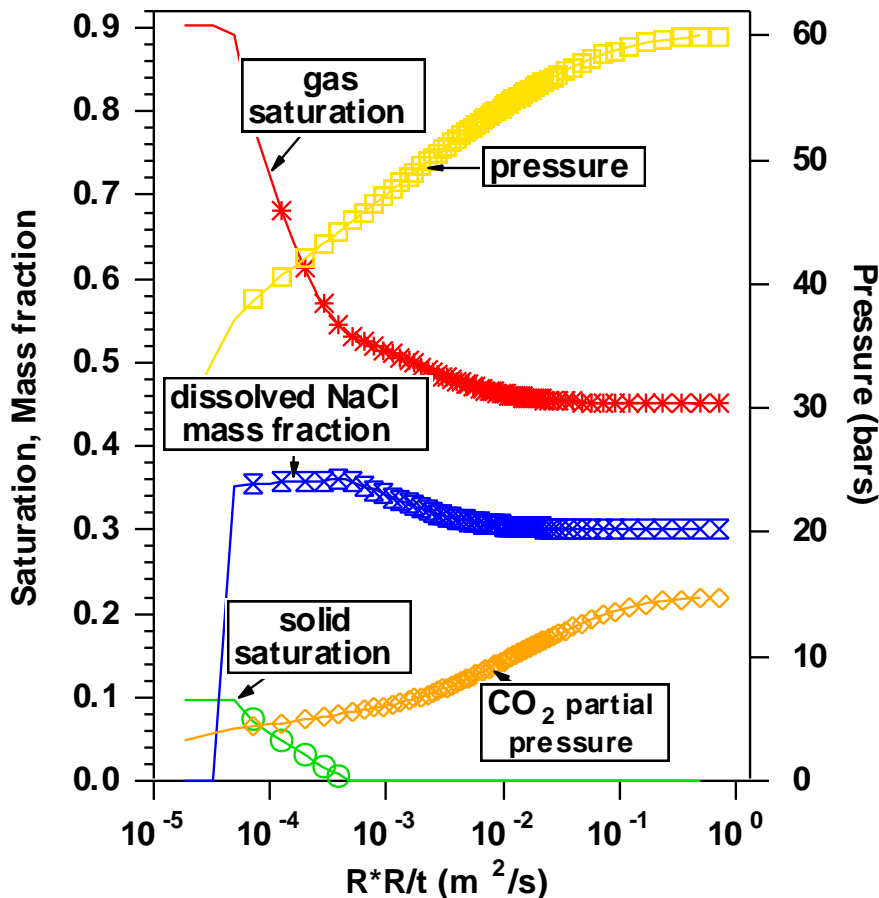


Figure 14.3. Simulated thermodynamic conditions for 1-D radial flow problem with salinity and non-condensable gas, plotted as a function of the similarity variable $x = R^2/t$. Results at 2×10^6 seconds are shown as lines, while the data at $t = 5 \times 10^5$ seconds are given as symbols.

14.2 Coupled Reservoir-Wellbore Flow

Geothermal production wells typically operate at (nearly) constant wellhead pressures. As flow rate and flowing enthalpy change with time, wellbore pressure gradients and flowing bottomhole pressures will also change. From a conceptual point of view, the most straightforward way to describe production from geothermal wells is to set up and solve equations for flow in the reservoir and flow in the wellbore in a fully coupled manner. This approach was taken by Hadgu et al. (1995) who coupled the reservoir simulator TOUGH (Pruess, 1987) with the wellbore simulator WFSA (Hadgu and Freeston, 1990).

As discussed by Murray and Gunn (1993), an alternative approach may be preferable in which the wellbore and reservoir simulations are performed separately. This can be accomplished by running a wellbore flow simulator prior to the reservoir simulation for a range of flow rates q and flowing enthalpies h , in order to generate a table of flowing bottomhole pressures P_{wb} .

$$P_{wb} = P_{wb}(q, h; P_{wh}, z, r_w) \quad (14.1)$$

In addition to the functional dependence on q and h , flowing bottomhole pressure is dependent on a number of well parameters. These include wellhead pressure P_{wh} , feed zone depth z , wellbore radius r_w , friction factors, and possibly others. Fig. 14.4 shows flowing bottomhole pressures as a function of well flow rate and enthalpy for a 0.2 m (\approx 8 inch) inside diameter well of 1,000 m feed zone depth with 7 bars wellhead pressure. The data plotted in this figure were obtained by running the HOLA wellbore simulator (Aunzo et al., 1991) for a range of flow rates and enthalpies. Formation temperature for the conductive heat loss calculation in HOLA was assumed to increase linearly from 25 °C at the land surface to 275.5 °C at 750 m depth.

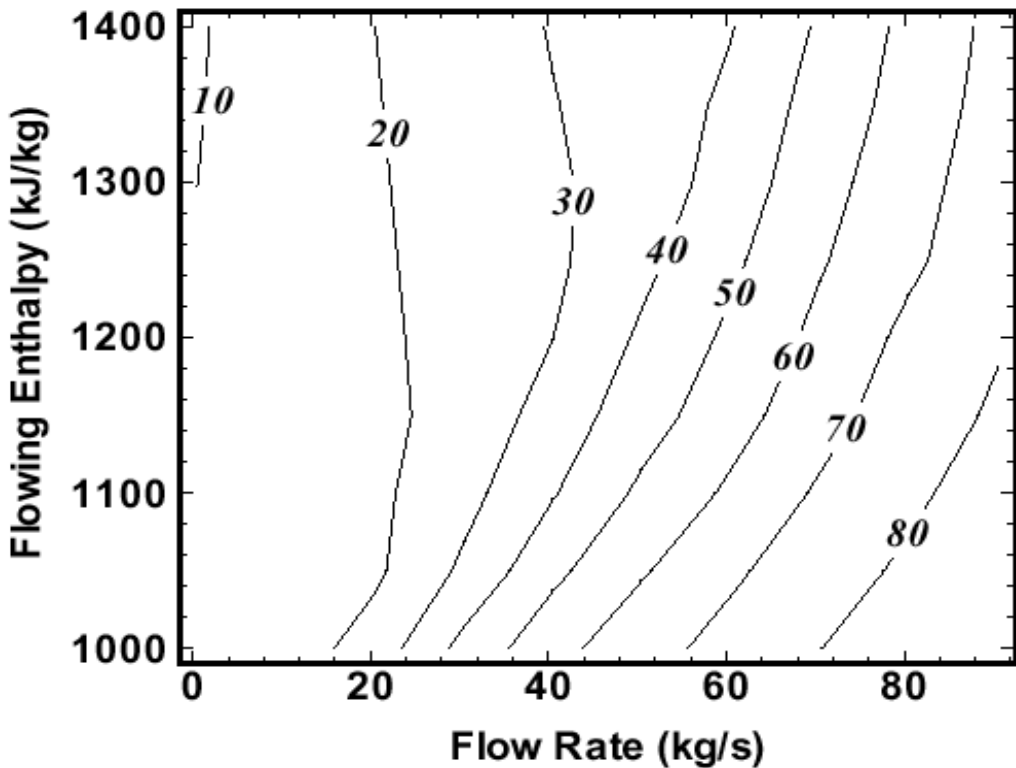


Figure 14.4. Contour plot of flowing bottomhole pressures, in bars (Pruess et al., 1999).

By interpolating on data such as shown in Fig. 14.4, Eq. (14.1) can be directly inserted into the source term representing flow from a well.

$$q_\beta = \frac{k_{r\beta}}{\mu_\beta} \rho_\beta \cdot PI \cdot (P_\beta - P_{wb}) \quad (14.2)$$

Here PI denotes the productivity index, which is a measure of the well inflow rate for given formation parameters and driving pressures. Reservoir flow equations that include a quasi-steady approximation to wellbore flow can then be solved with little added computational expense compared to the case where no wellbore flow effects are considered. In comparison with a fully coupled execution of reservoir and wellbore simulation, representing wellbore flow effects by interpolation from tabular data has some advantages, including increased robustness and calculational efficiency. It also makes it possible to use different wellbore simulators and two-phase flow correlations without any programming changes in the reservoir simulation code.

In order to demonstrate the behavior of a coupled reservoir-well system, we present a sample problem from the TOUGH2 user's guide (Pruess et al., 1999), which is a variation of a problem first solved by Hadgu et al. (1955). A well with the same characteristics as were used to obtain the data plotted in Fig. 14.4 produces from a 500 m thick two-phase reservoir containing water at initial conditions of $P = 60$ bars, $T = T_{sat}(P) = 275.5$ °C, $S_g = 0.1$. Simulated flow rate (q), flowing enthalpy (h), flowing bottomhole pressure (P_{wb}) and reservoir pressure in well grid block (P_{res}) are shown in Fig. 14.5. For comparison we also show results obtained for production with a fixed bottomhole pressure of $P_{wb} = 57.37$ bars, which is the flowing bottomhole pressure in the coupled reservoir-wellbore system at the end of the first time step (10^5 seconds). The simulation with constant bottomhole pressure gives a rapidly declining production rate. The coupled reservoir-wellbore system sustains long-term production at substantially higher rates, because it predicts a stronger rise in flowing enthalpy, for which wellbore flow requires a smaller bottomhole driving pressure. The large differences when compared with the simulation with constant bottomhole pressure emphasize the importance of coupled wellbore flow effects for two-phase geothermal production wells.

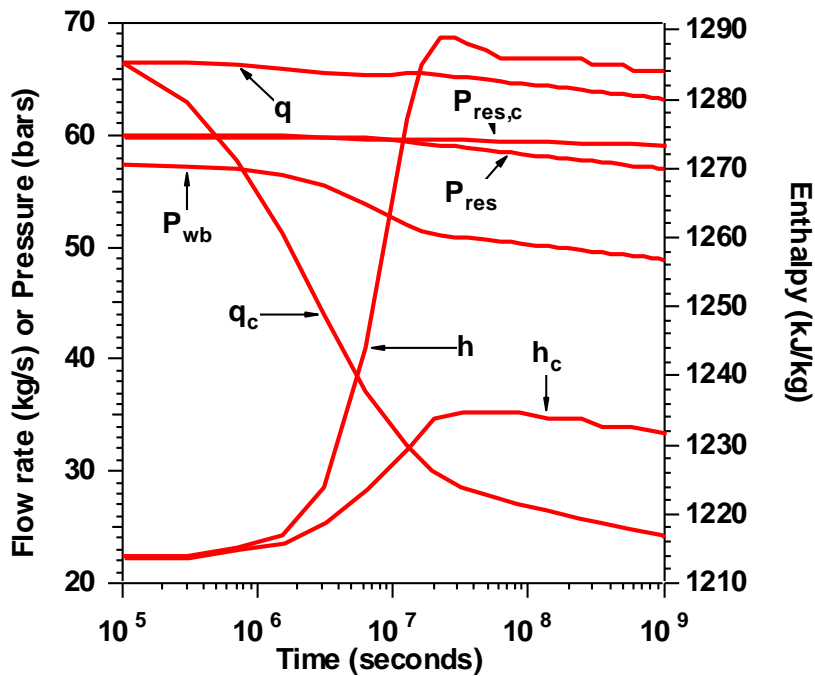


Figure 14.5. Flow behavior of a coupled reservoir-well system. Results are for flow rate (q), flowing enthalpy (h), flowing bottomhole pressure (P_{wb}), and reservoir pressure in well grid block (P_{res}). Curves with subscript “c” are for a system with constant flowing bottomhole pressure.

14.3 Injection of Cold Water

Injection of fluid with a different temperature into a permeable medium will give rise to heat transfer between fluids and reservoir rocks. In a medium with intergranular porosity, heat transfer between fluids and rocks will be rapid, so that temperature equilibrium is quickly attained locally. The heat exchange will retard the advancement of the thermal front relative to the pore velocity of the fluid. For idealized conditions of local thermodynamic equilibrium in a homogeneous porous medium, the thermal front will be sharp (except for usually small broadening from heat conduction), and will be retarded relative to the advancement of a conservative solute tracer by a retardation factor R which is given by the ratios of specific heat of the pore fluid to the entire rock-fluid mixture (Bodvarsson, 1972).

$$R = \frac{\phi \rho c_w}{\phi \rho c_w + (1 - \phi) \rho_R c_R} \quad (14.3)$$

Here, ρ is the density and c_w is the heat capacity of water. Quantities indexed with “R” pertain to reservoir rocks.

Conditions are more complex in fractured reservoirs, where cooler injected fluids may advance rapidly along fractures, while being heated only slowly by conductive heat transfer from large matrix blocks. This gives rise to very broad temperature distributions, see Fig. 14.6.

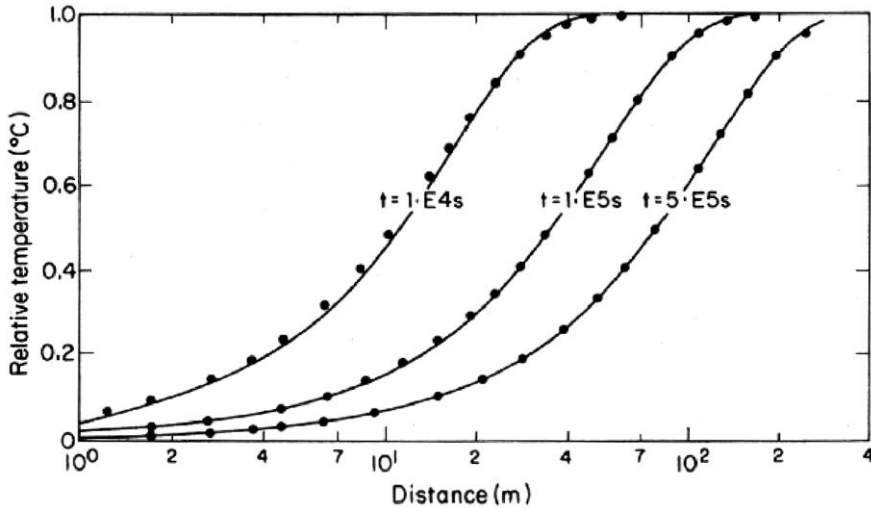


Figure 14.6. Temperature fronts during non-isothermal injection into a 1-D fracture (from Pruess and Bodvarsson, 1984). The lines represent the analytical solution of Lauwerier (1955), while the points give results obtained by numerical simulation. "Relative temperatures" are normalized to the difference between initial and injection temperatures.

Most geothermal reservoirs have predominant fracture permeability, and tracers can assist in finding fast and short-circuiting flow connections between wells. Intuitively one expects that there should be a correlation between tracer breakthrough and thermal breakthrough, and that one should avoid injecting cold water into wells that are connected to production wells by fast short-circuiting pathways. However, a more detailed analysis shows that the advancements of thermal fronts and solute tracers depend on different physical parameters. The velocity of tracer movement depends on the pore volume, while thermal breakthrough depends on the heat transfer area available along the flow path. Consider a fracture with a given heat transfer (wall) area. If such a fracture were artificially enlarged by increasing the distance between the walls, pore volume would increase but heat transfer area would remain unchanged. The relationship between fluid residence time and thermal breakthrough time involves the (generally unknown) fracture aperture as a parameter. This is shown in Fig. 14.7 for the simplified case of 1-D linear flow in a fracture.

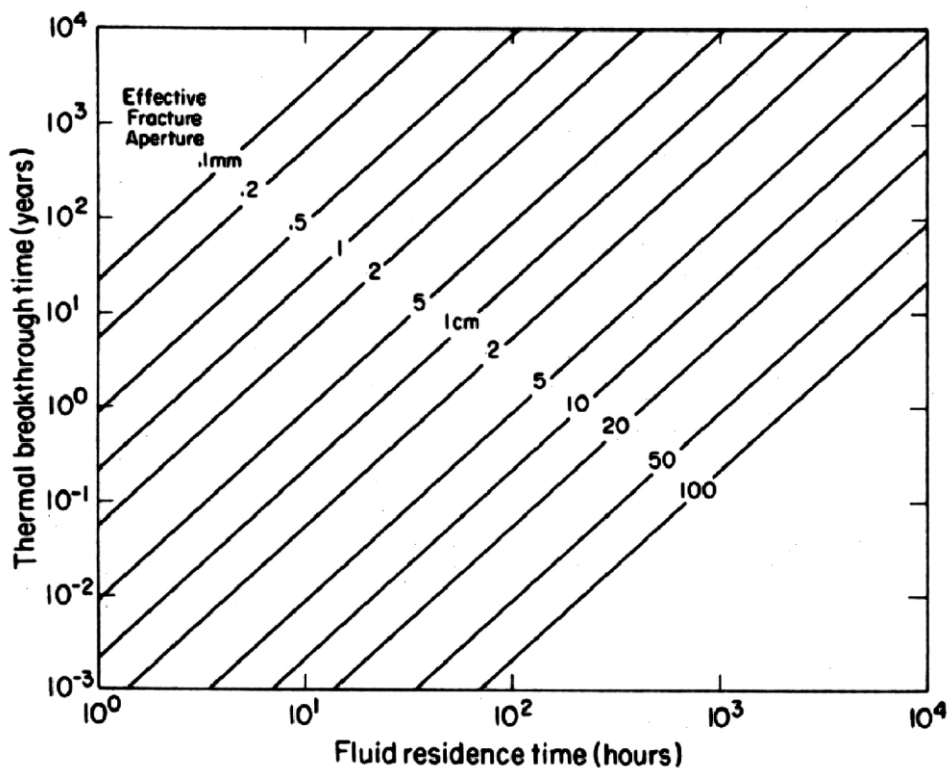


Figure 14.7. Thermal breakthrough time as function of fluid residence time and effective fracture aperture (from Pruess and Bodvarsson, 1984).

14.4 Five-Spot Production and Injection

The grid system shown in Fig. 12.5 was used to investigate enhanced heat recovery by means of water injection. The grid has six rows, each containing between one and eleven elements, for a total of thirty-six volume elements; for simplicity, only a single layer of 305 m thickness is modeled. The problem specifications as given in Table 14.1 correspond to conditions that may typically be encountered in deeper zones of hot and fairly tight fractured two-phase reservoirs (Pruess and Narasimhan, 1985). Problem variations explored by means of TOUGH2 simulations include a porous medium representation of the reservoir, as well as a fractured medium description based on the MINC concept, using embedded impermeable matrix blocks in the shape of cubes. Fig. 14.8 shows simulated temperature profiles along a line from production to injection well after 36.5 years. It is seen that the MINC results for 50 m fracture spacing are virtually identical to the porous medium results, while another MINC run for 250 m fracture spacing shows lower temperatures, indicating a less complete thermal sweep.

Table 14.1. Parameters for five-spot problem

Formation	
Rock grain density	2650 kg/m ³
Specific heat	1000 J/kg°C
Heat conductivity	2.1 W/m°C
Permeable volume fraction	2%
Porosity in permeable domain	50%
Impermeable blocks: cubes with side length	50m, 250 m
Permeability	6.0x10 ⁻¹⁵ m ²
Thickness	305 m
Relative permeability: Corey curves	
irreducible liquid saturation	0.30
irreducible gas saturation	0.05
Initial Conditions	
Temperature	300 °C
Liquid saturation	0.99
Pressure	85.93 bar
Production/Injection	
Pattern area	1 km ²
Distance between producers and injectors	707.1 m
Production rate*	30 kg/s
Injection rate*	30 kg/s
Injection enthalpy	500 kJ/kg

* Full well basis

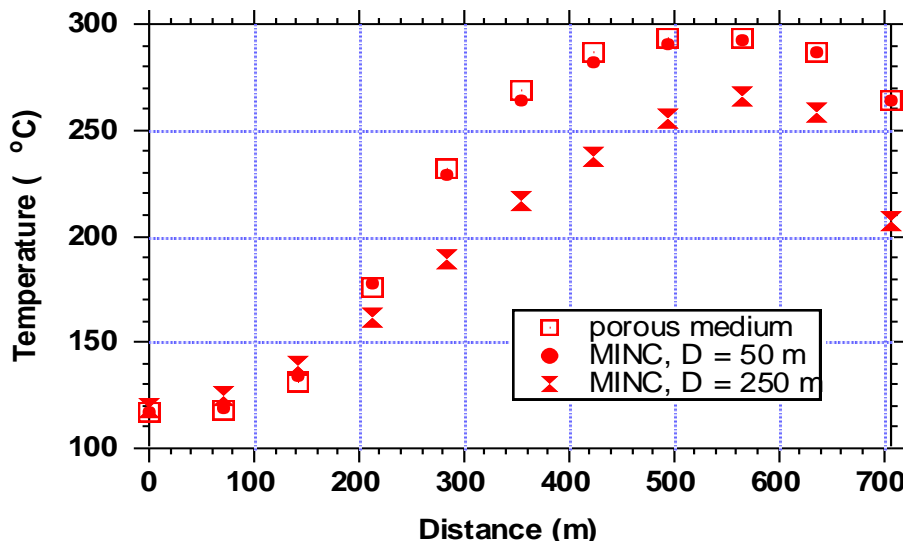


Figure 14.8 Temperature profiles for five-spot problem along a line from injection to production well after 36.5 yrs.

14.5 Heat Sweep in a Vertical Fracture

In many geothermal fields there is evidence of rapid migration of injected fluids along preferential flow paths, presumably along fractures. The present problem is designed to study thermal interference along such paths, by considering nonisothermal injection into and production from a single vertical fracture, as illustrated in Fig. 14.9 (from Pruess and Bodvarsson, 1984). The fracture walls are modeled as semi-infinite half-spaces of impermeable rock, which provide a conductive heat supply. Initial temperature is 300 °C throughout. Water at 100 °C temperature is injected at one side of the fracture at a constant rate of 4 kg/s, while production occurs at the other side against a specified wellbore pressure. Problem parameters are given in Table 14.2.

The most important heat transfer process in this problem is conductive heat supply from the rock adjacent to the fractures. This could be modeled by explicitly including the wall rock as a medium of low or vanishing permeability into the definition domain of the model. As a far more efficient and accurate alternative, the TOUGH2 simulation uses a semi-analytical treatment of heat transfer in the semi-infinite conductive half spaces adjacent to the fracture walls, using a method developed by Vinsome and Westerveld (1980), in which no explicit representation of the conductive domains by means of grid blocks is needed. Thus the flow problem reduces to 2-D. We use a grid spacing of 20 m in both horizontal and vertical directions, for a total of 120 grid blocks. Figure 14.10 shows the simulated temperature distribution after 5 years, while Fig. 14.11 shows the temperature of the produced fluid as a function of time.

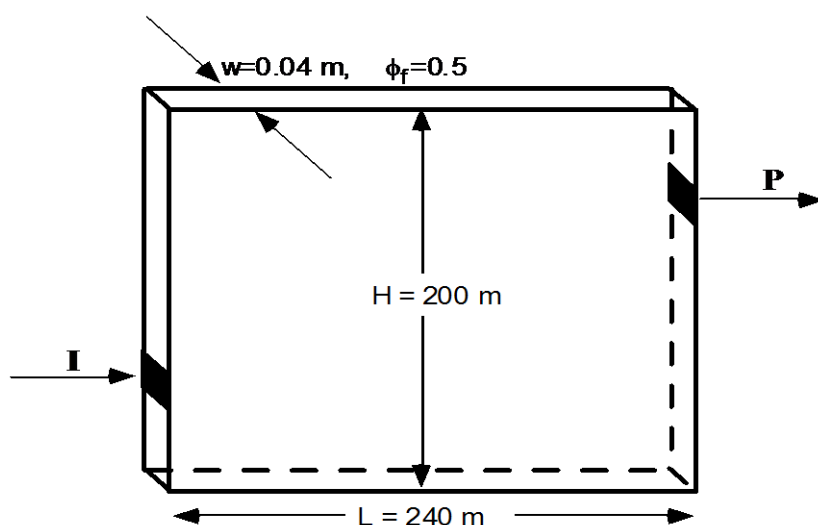


Figure 14.9. Schematic diagram of injection-production system in vertical fracture.
Injection occurs at I, production at P.

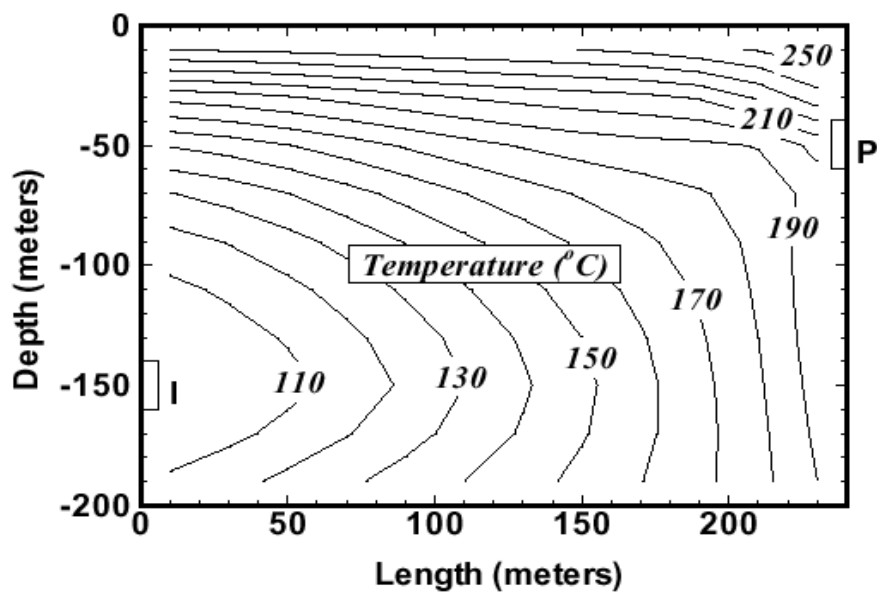


Figure 14.10. Temperature distribution in fracture plane after 5 years. Injection and production regions are marked I and P, respectively.

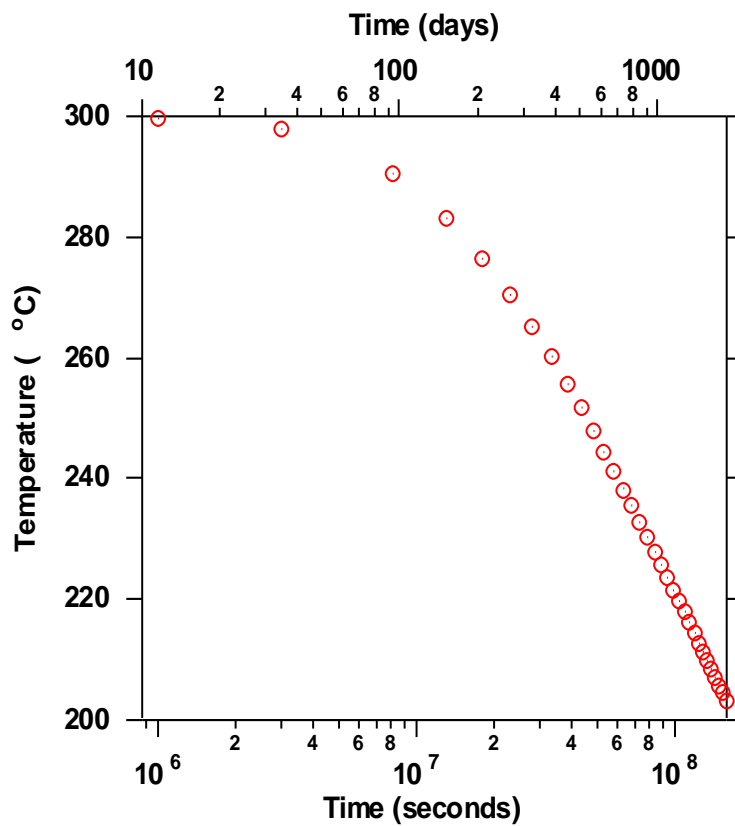


Figure 14.11. Produced fluid temperature versus time for vertical fracture problem.

Table 14.2. Parameters for fracture flow problem

Rock	
Thermal conductivity	2.1 W/m°C
Specific heat	1000 J/kg°C
Density	2650 kg/m ³
Permeability	0
Fracture	
Height	200 m
Length	240 m
Aperture	0.04 m
Permeability	$200 \times 10^{-12} \text{ m}^2$ (200 darcy)
Porosity	50 %
Initial Conditions	
Temperature	300 °C
Pressure	hydrostatic profile
Average pressure	100 bar
Injection	
Enthalpy	$4.2 \times 10^5 \text{ J/kg}$ (appr. 100 °C)
Rate	4 kg/s
Production	
Productivity index	$4 \times 10^{-12} \text{ m}^3$
Flowing pressure	96.5 bar

15. Site-Specific Reservoir Modeling

The approach to be taken in a simulation study of a specific reservoir depends on (a) the objectives of the study, (b) available data, and (c) available time and budget. Objectives may include things such as

- determine reservoir conditions and flow mechanisms
- identify upflow and recharge zones
- evaluate well decline, need for makeup wells, and optimal well spacing
- estimate future changes in discharge enthalpy and chemical composition of produced fluids
- estimate generating capacity and sustainability of a geothermal field
- production and injection design
- chemical compatibility of fluids

- well test design and analysis
- other issues in reservoir management

Data available for a simulation study may include

- geologic framework model
- data from wells (flow rates, flowing enthalpies, pressures and temperatures vs. time; fluid samples; well logs)
- geophysical surveys (resistivity, gravity, seismics, self-potential, etc.)
- geochemistry and mineralogy
- fluid and formation properties (temperature, pressure, salinity, permeability, porosity, ...)

Before proceeding with a simulation study it is necessary to develop a conceptual model. A conceptual model identifies the important aspects of the structure of the system and its most significant physical and chemical conditions and features. O'Sullivan et al. (2001) state "The conceptual model is usually represented by two or three sketches, showing a plan view and vertical sections of the geothermal system. On these sketches are shown the most important characteristics, such as surface manifestations (i.e., hot springs, steaming grounds, etc.), flow boundaries, main geologic features such as faults and layers, zones of high and low permeability, isotherms, location of deep inflows and boiling zones, geophysical data (resistivity boundaries, heat flow contours), etc. Setting up a conceptual model requires the synthesis of information from a multi-disciplinary team composed of geologists, geophysicists, geochemists, reservoir engineers and project managers. Some of the raw data require expert interpretation before they can be used. For example, the down-hole temperature logs which are used to construct the isotherm plots are often affected by internal wellbore flows, or the previous production and injection history of the well (see Grant et al., 1982). In addition, the data sets tend to be incomplete and often the conceptual models proposed by the various contributing scientists and engineers are inconsistent or incorrect. Thus the "art" of computer modeling involves the synthesis of conflicting opinions, interpretation and extrapolation of data to set up a coherent and sensible conceptual model which can be developed into a computer model."

A general methodology for geothermal field simulation has emerged, which involves the following modeling phases (Fig. 15.1; Bodvarsson et al., 1986; Bodvarsson and Witherspoon, 1989).

- Natural state (zones of upflow, recharge, and outflow; heat sources and sinks; thermodynamic conditions; formation parameters);

- Field production (history match: well rates, pressures, temperatures, enthalpies, solutes and gases, tracers; geochemical changes; time-lapse geophysics);
- Prediction scenarios (well decline, injection interference, fluid composition: solutes and gases, makeup wells, fluid and heat reserves, producibility and sustainability).

These three phases are often preceded by

- using numerical simulation to design and analyze well tests (production, injection, pressure transients, tracers).

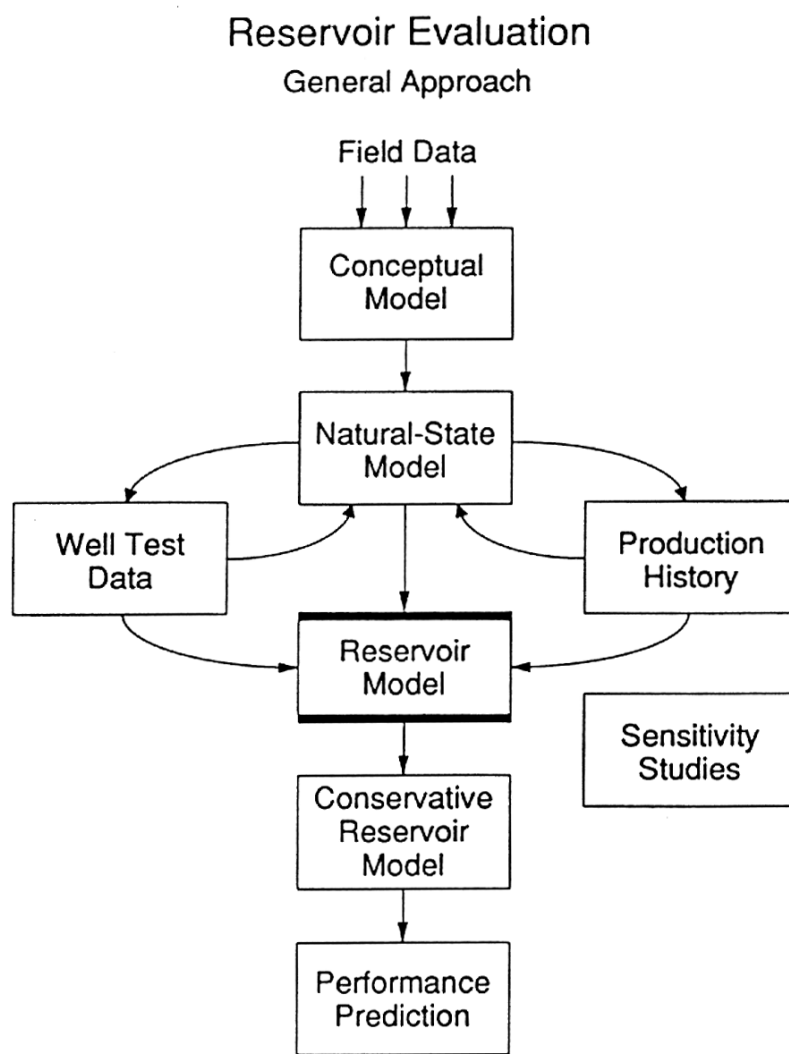


Figure. 15.1. General approach to reservoir evaluation
(from Bodvarsson and Witherspoon, 1989).

Geothermal reservoirs are dynamic systems that are subject to throughput of fluids and heat. The initial state and boundary conditions of a reservoir model must be developed carefully to provide a viable basis for modeling field exploitation (production and injection

operations). It is not satisfactory to simply specify initial conditions based on (typically sparse) subsurface measurements and conjectures about inflow and outflow zones. The initial state of a production model must be “stable,” i.e., it must be close to a steady state for the applied boundary conditions. If this is not the case, then large changes may occur when running the reservoir model forward in time; changes that have nothing to do with field perturbations due to exploitation. The initial state must be developed through careful modeling of the natural, pre-exploitation state. The procedure for natural state modeling is summarized in Fig. 15.2. We note that steady states are insensitive to storage-type parameters such as porosity, or specific heat of the rocks.

For history matching of production and injection operations, the natural state conditions are used as initial and boundary conditions. Appropriate wells are placed into the reservoir model, and simulated parameters such as flow rates, pressures, temperatures, enthalpies, tracer concentrations, etc. are compared with field observations. Model parameters such as distribution of permeability and porosity, fracture spacings, and others are then modified so as to reduce discrepancies between simulated and observed reservoir behavior. The process of parameter adjustment, often referred to as “model calibration,” can be performed in trial-and-error fashion, using engineering judgment, or it can be automated through so-called “inverse methods,” which use mathematical algorithms to automatically identify and vary sensitive model parameters, until the discrepancy between simulation and field behavior is reduced to a minimum (Finsterle et al., 2000). Inverse methods can greatly reduce the tedium of “manual” model calibration, but they have limitations as well. They cannot replace a good fundamental understanding of a given geothermal system, and their application requires good engineering judgment. Inverse techniques can only optimize a limited number of parameters within a given conceptual model. A sound conceptual model remains the most important ingredient for successful reservoir simulation.

A successfully calibrated production state model can be used in forward mode to explore future field behavior, subject to various planned or proposed scenarios and constraints. For example, the sustainability of a certain rate of fluid extraction (power production) can be evaluated. The need for makeup wells may be explored, and different injection schemes may be evaluated in terms of thermal breakthrough and pressure support. Model predictions naturally will become less reliable with increasing prediction period. As a rule of thumb, predictions from a well-calibrated model may be considered reliable for a similar period of time as the length of the history-match period. Only a few studies have been published that evaluate simulator predictions against subsequent field observations, with generally favorable results (O’Sullivan et al., 2001). Comparisons are limited by the fact that

field operations often do not comply with the prescriptions for production and injection employed in the simulations.

FIGURE 1: FLOW CHART OF NUMERICAL SIMULATION OF THE INITIAL STATE

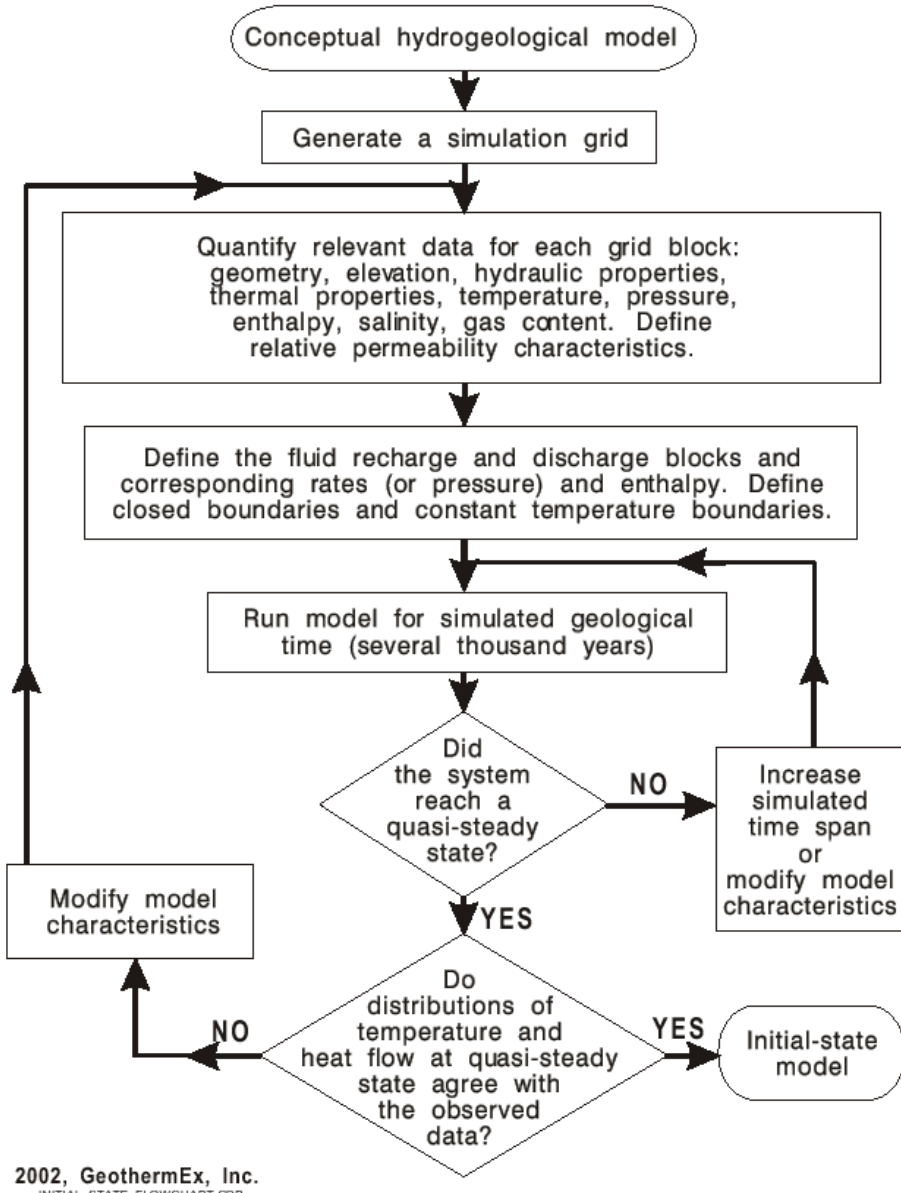


Figure 15.2. Flow chart for natural state modeling (courtesy of Subir Sanyal, 2002; used with permission).

Information on current approaches and trends in geothermal reservoir simulation is available in a recent review (O'Sullivan et al., 2001). The following features can be considered typical of current simulation approaches:

- 3-D models with a few thousand grid blocks;
- Spatial resolution ≥ 200 m horizontally, ≥ 100 m vertically;
- Geofluids represented as water, sometimes with dissolved salt and a non-condensable gas;
- Two-phase flow of water and gas, including phase change and heat transfer;
- Chemical reactions generally not considered;
- Advection-dispersion equation for tracers;
- Porous medium, or sometimes variations of double porosity.

Computer modeling of geothermal fields is a mature and widely used technology, but advances in simulation methodology are continuing. Current trends include the following developments.

- More realistic representation of reservoir fluids (multicomponent mixtures with dissolved solids and non-condensable gases);
- Reactive and phase-partitioning tracers (natural or man-made);
- Comprehensive reactive chemistry (rock-fluid interactions);
- Use of geophysical data in model calibration (microgravity and resistivity changes, self-potential, seismic surveys, subsidence, etc.);
- Near-critical and super-critical temperatures;
- Coupling between fluid flow and rock stresses, especially for enhanced geothermal systems and hot dry rock (EGS, HDR);
- Multi-scale phenomena and conditions (sharp fronts, heterogeneity, threshold and instability effects);
- Automatic model calibration (history matching);
- Joint inversions;
- Improved solution algorithms and user features.

There is much cross fertilization with developments in related areas, including nuclear waste disposal, environmental modeling, and studies of the unsaturated zone.



LECTURE V: SPECIAL TOPICS

This section illustrates applications of numerical simulation to a variety of geothermal flow problems. The selection reflects the research interests and bias of the author.

16. Water Injection into Depleted Vapor Zones

In response to extensive steam production, the vapor-dominated geothermal reservoirs at The Geysers, California, and Larderello, Italy, are beginning to run out of fluid, while heat reserves in place are still enormous. Injection of liquid water is the primary means by which dwindling fluid reserves can be replenished, and recovery of thermal energy be enhanced and accelerated. Field experience shows that water injection may have very beneficial effects, increasing reservoir pressures and flow rates of offset steam production wells. Effects of water injection are not always favorable, however, because thermal degradation (temperature decline) or water breakthrough may occur at neighboring wells.

Cold water injection into superheated vapor zones gives rise to a complex interplay of fluid flow and heat transfer with phase change (boiling and condensation). In the approximation of 1-D radial flow, this results in a system with a boiling phase front propagating ahead of a temperature front (Fig. 16.1). Results from a numerical simulation of the process are shown in Fig. 16.2.

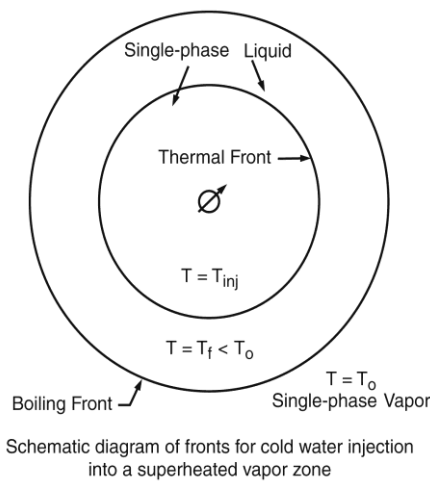
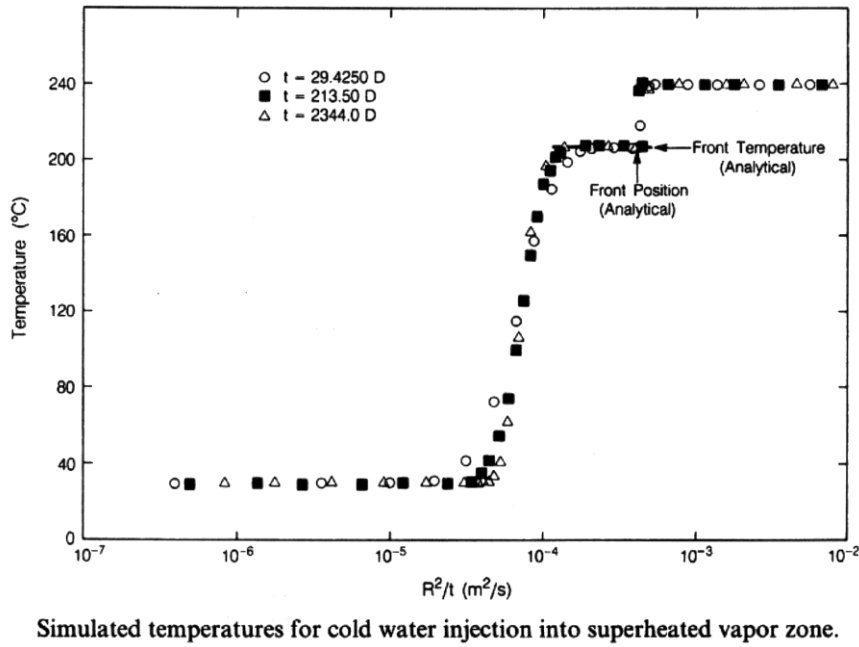


Figure 16.1. Schematic diagram of fronts for cold water injection into a superheated vapor zone (from Pruess et al., 1987).

For the more realistic case where injection is made into fractures the resulting fluid flow and heat transfer processes are far more complex. Two-phase flow in the plume takes

place under the combined action of gravity, capillary, and pressure forces. Liquid water will also partially



Simulated temperatures for cold water injection into superheated vapor zone.

Figure 16.2. Simulated temperatures for cold water injection into a superheated vapor zone, plotted as function of the similarity variable R^2/t . (from Pruess et al., 1987).

imbibe into the rock matrix. In regions where the fractures are open, water will flow generally downward, driven by gravity. However, at asperity contacts (fracture walls touching) water may pond and be diverted sideways. In regions of small fracture apertures or strong wall roughness, capillary pressure effects could also be significant. Conductive heat transfer from the wall rocks causes the temperature of the water to increase, and eventually boiling is initiated when the water reaches the saturation temperature at prevailing pressure. The vaporization process is accompanied by an increase in pressure which drives the steam away from the injection plume. The behavior of a cold water plume injected into a sub-vertical fracture under superheated conditions is shown schematically in Fig. 16.3. The boiling injection plume is a very efficient heat transfer system, operating by means of vapor-liquid counterflow (heat pipe; see Sec. 18, below). In hotter regions, at larger distance from the injection point, vapor pressures are larger than in cooler portions of the plume. Accordingly, vapor will flow from the hotter to the cooler regions (generally towards the injection point, opposing liquid flow which is directed away from the injection point). The hotter regions are zones of evaporation, in which latent heat is consumed, while in the cooler regions condensation is taking place, accompanied by deposition of latent heat. The latent heat transfer coupled with vapor flow tends to equalize temperatures throughout the two-phase plume. Numerical simulations for injection into heterogeneous fractures at superheated conditions are shown in Fig. 16.4.

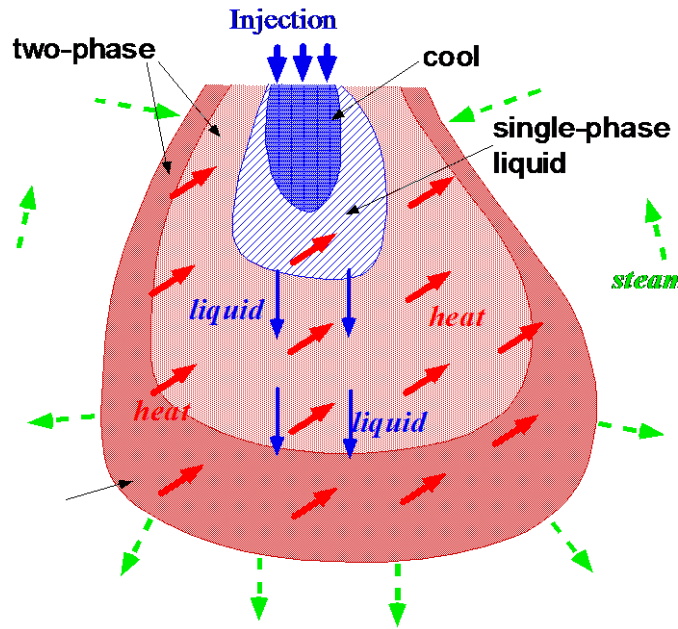


Figure 16.3. Schematic of cold water injection into a sub-vertical fracture filled with superheated steam (from Pruess, 1996).

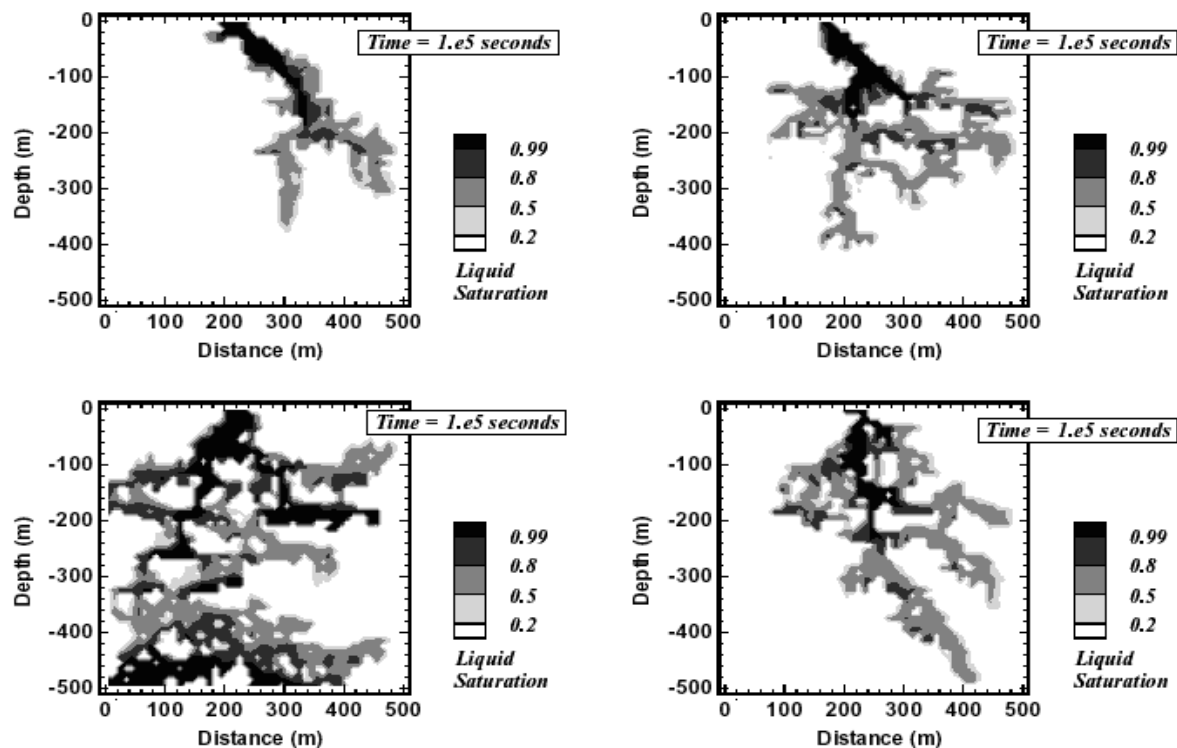


Figure 16.4. Simulated plumes for injection at a rate of 10 kg/s into four heterogeneous vertical fractures (from Pruess, 1997).

17. Phase Partitioning Tracers

Tracer testing is an important technique for investigating flow paths in geothermal systems. For applications in two-phase and vapor-dominated reservoirs, there is much interest in phase-partitioning tracers, such as non-condensable gases or man-made volatile chemicals, that can partially dissolve in the liquid phase, while partially volatilizing into the gas phase. In two-phase conditions, the total (advective and diffusive) mass fluxes of a trace component are obtained by simply adding the contributions from liquid and gas phases, taking the distribution of tracers among the phases into account.

Effective gas and liquid phase diffusivities at geothermal reservoir conditions are typically of order 10^{-7} and 10^{-10} m²/s, respectively. Corresponding diffusion distances over a time period of one year are, respectively, 1.8 and 0.0032 m. These distances are small, and it might appear as though diffusion effects would be negligible for tracer tests that may cover time periods of days to months. However, as will be seen this is not the case in fractured reservoirs, where tracers can diffuse away from the fractures into the rock matrix, and later back-diffuse into the fractures when the primary tracer pulse has passed.

We briefly summarize a numerical simulation that was patterned after injection tests with volatile tracers at The Geysers vapor-dominated reservoir in California (Beall et al., 1994, 1998). The field tests injected tritiated water and water-soluble chemicals such as R13 (CClF_3) and R134a ($\text{C}_2\text{H}_2\text{F}_4$). Different breakthrough curves (BTCs) were observed in an undepleted reservoir zone as compared to a superheated vapor region (Figs. 17.1, 2; Beall et al., 1994). The rapid returns and large tracer concentrations obtained in the superheated region were interpreted as indicating rapid, strong vaporization of injected water, while the low concentrations and slow response times in the undepleted zone were attributed to delayed and partial vaporization (Beall et al., 1994).

The simulations employed a five-spot geometry as shown in Fig. 17.3. Typical formation parameters used in previous modeling work at The Geysers were employed, and a fractured reservoir description using the MINC-method with one fracture and four matrix continua was employed (see Figs. 13.1, 13.2). The simulated BTCs shown in Fig. 17.4 show similar timings and shapes as the BTCs seen in the field. The long tail in the BTC for the strongly depleted zone (Case 2) is caused by tracer entering the matrix blocks at early times, which later diffuses back into the fractures (Fig. 17.5). The sensitivity of BTCs to this fracture-matrix interchange may allow a determination of mean matrix block size (= fracture spacing). More details are given in the original paper (Pruess, 2002).

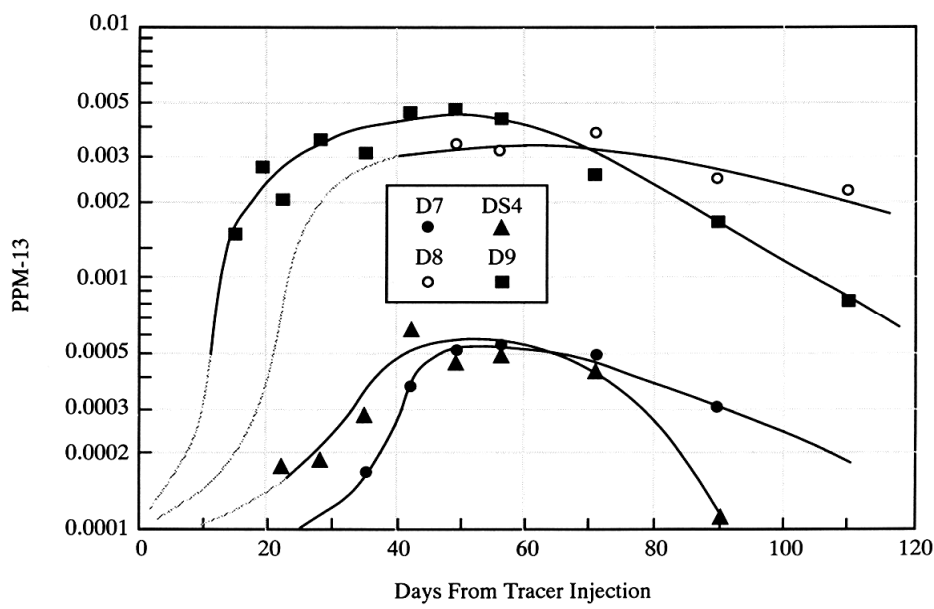


Figure 17.1. R-13 concentration in produced steam from wells in an undepleted region of The Geysers (Bear Canyon) versus time elapsed since tracer injection (from Beall et al., 1994; lines are drawn to guide the eye).

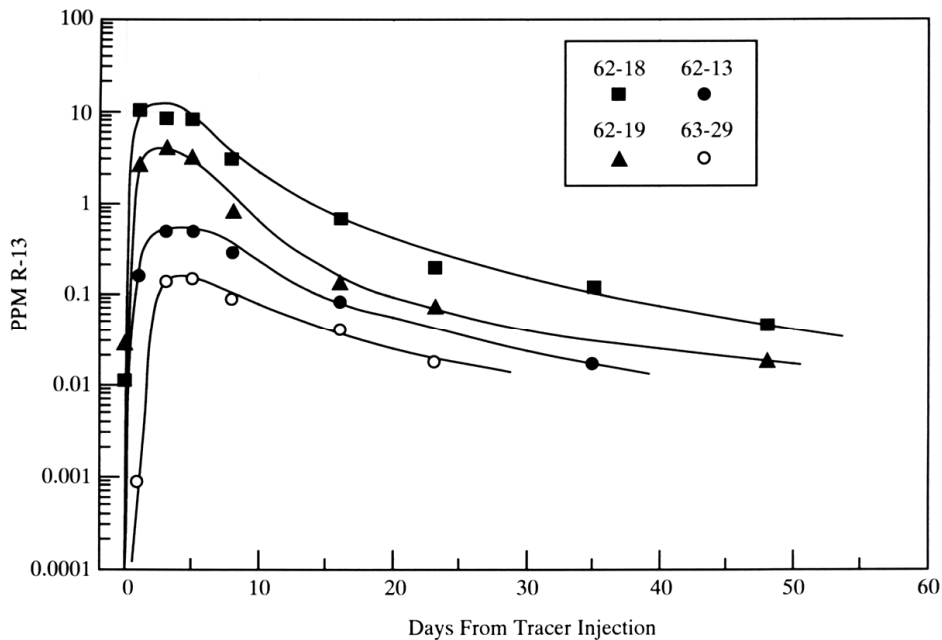


Figure 17.2. R-13 concentration in produced steam from wells in a depleted region of The Geysers (SMUD and Unit 20) versus time elapsed since tracer injection (from Beall et al., 1994; lines are drawn to guide the eye).

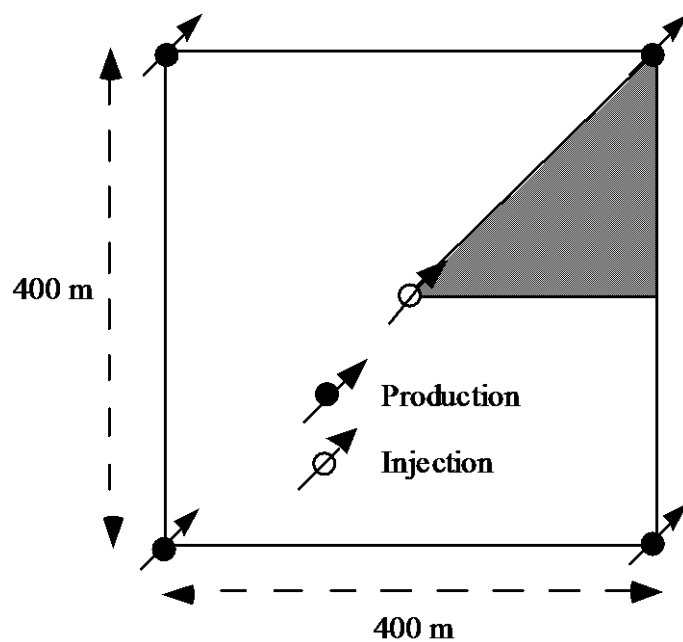


Figure 17.3. Five-spot production-injection system used for analysis of tracer migration.

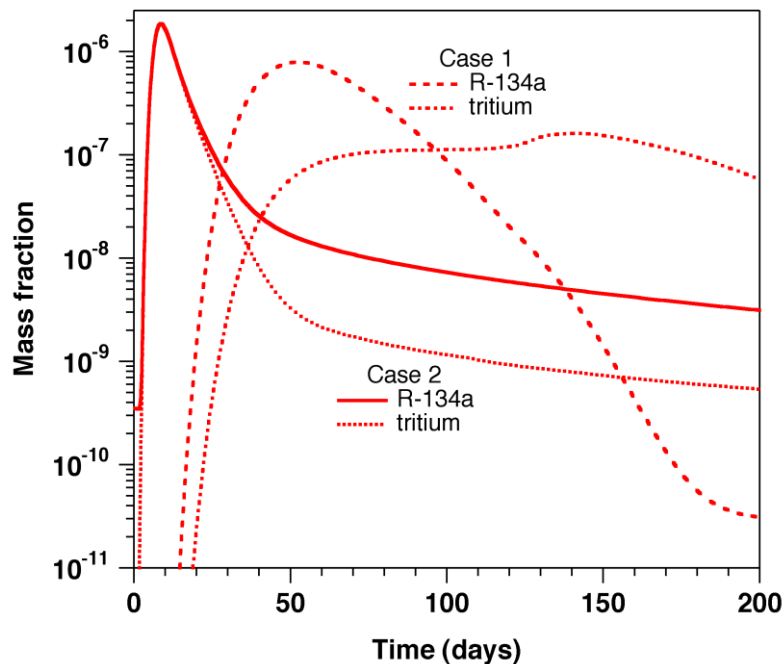


Figure 17.4. Simulated tracer breakthrough curves for five-spot problem in a vapor-dominated reservoir. Case 1 corresponds to conditions with large water saturation in the rock matrix (undepleted), while Case 2 corresponds to a depleted reservoir zone with small water saturation.

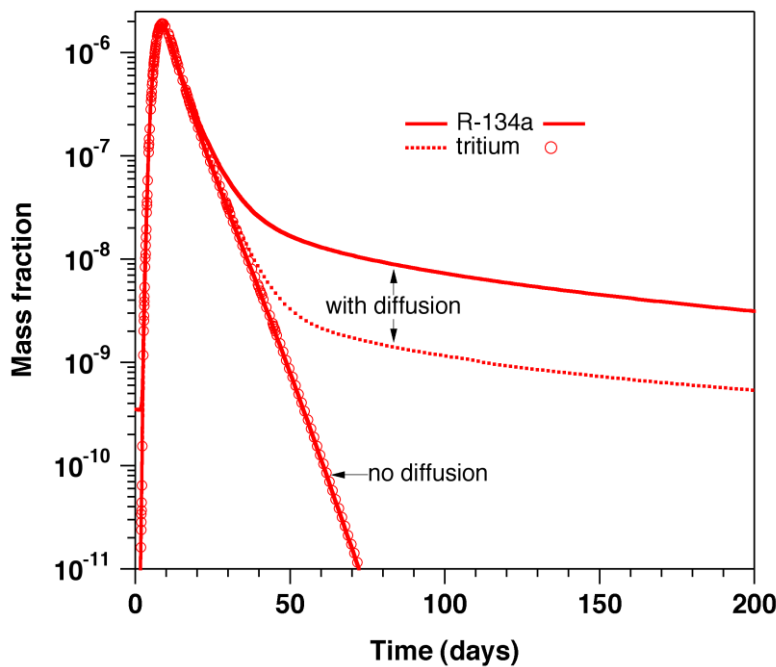


Figure 17.5. Breakthrough curves for Case 2 (depleted conditions), showing effects of diffusive mass exchange between fractures and matrix.

18. Heat Pipe Systems

Heat pipes are two-phase systems in which heat transfer occurs by means of vapor-liquid counterflow (Fig. 18.1). Water is vaporized near a deep heat source, and the vapor is pushed upward by pressure gradients. At some distance the vapor condenses, releasing a large amount of heat, and the liquid condensate flows back towards the heat source under the force of gravity. (On a small scale, heat pipes can operate by capillary force, which will draw liquid condensate back towards the region of lower water saturation near the heat source.)

In a steady-state heat pipe system, the upflow of vapor balances the downflow of liquid. Denoting the mass flux by \mathbf{F} , the corresponding heat flux \mathbf{G} is given by

$$\mathbf{G} = \mathbf{F}(h_v - h_l) \quad (18.1)$$

Water has a very large enthalpy of vaporization, $h_v - h_l = 1766.5 \text{ kJ/kg}$ at $T = 240^\circ\text{C}$ (Keenan et al., 1969), so that large heat flows can be associated with modest mass flows. From the foregoing discussion it follows that in a gravity-driven heat pipe system, the pressure gradient in the vertical direction must be intermediate between the vapor-static and hydrostatic values, in order that the driving force for vapor is upward, and the driving force for liquid downward.

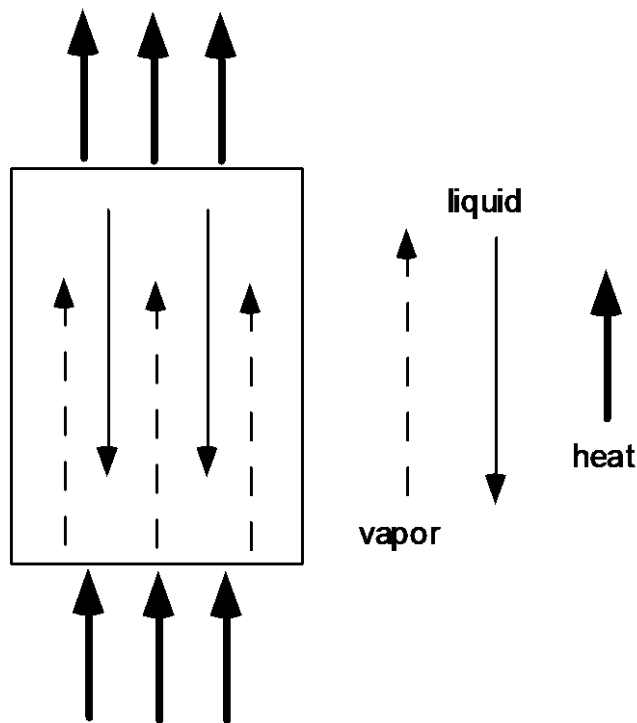


Figure 18.1. Schematic of a heat pipe system

The heat pipe mechanism can operate in geothermal reservoirs over a large region. Geothermal heat pipe systems can exist in two alternative conditions, liquid-dominated or vapor-dominated heat pipes (Fig. 18.2). For the former, the pressure gradient in the vertical is near (but less than) hydrostatic, giving rise to a small driving force for liquid downflow, and a large driving force for vapor upflow. In order that net mass flow be small, vapor relative permeability must be small and liquid relative permeability large, hence the name “liquid-dominated” heat pipe. In a vapor-dominated heat pipe, vertical pressure gradient is near (but larger than) vaporstatic, giving rise to a small driving force for vapor upflow, and a large driving force for liquid downflow. For mass fluxes to be balanced, relative permeability to vapor must be then large, to liquid small. In liquid-dominated heat pipe systems, pressures are near the “boiling point for depth” (BPD) curve, see Fig. 18.3.

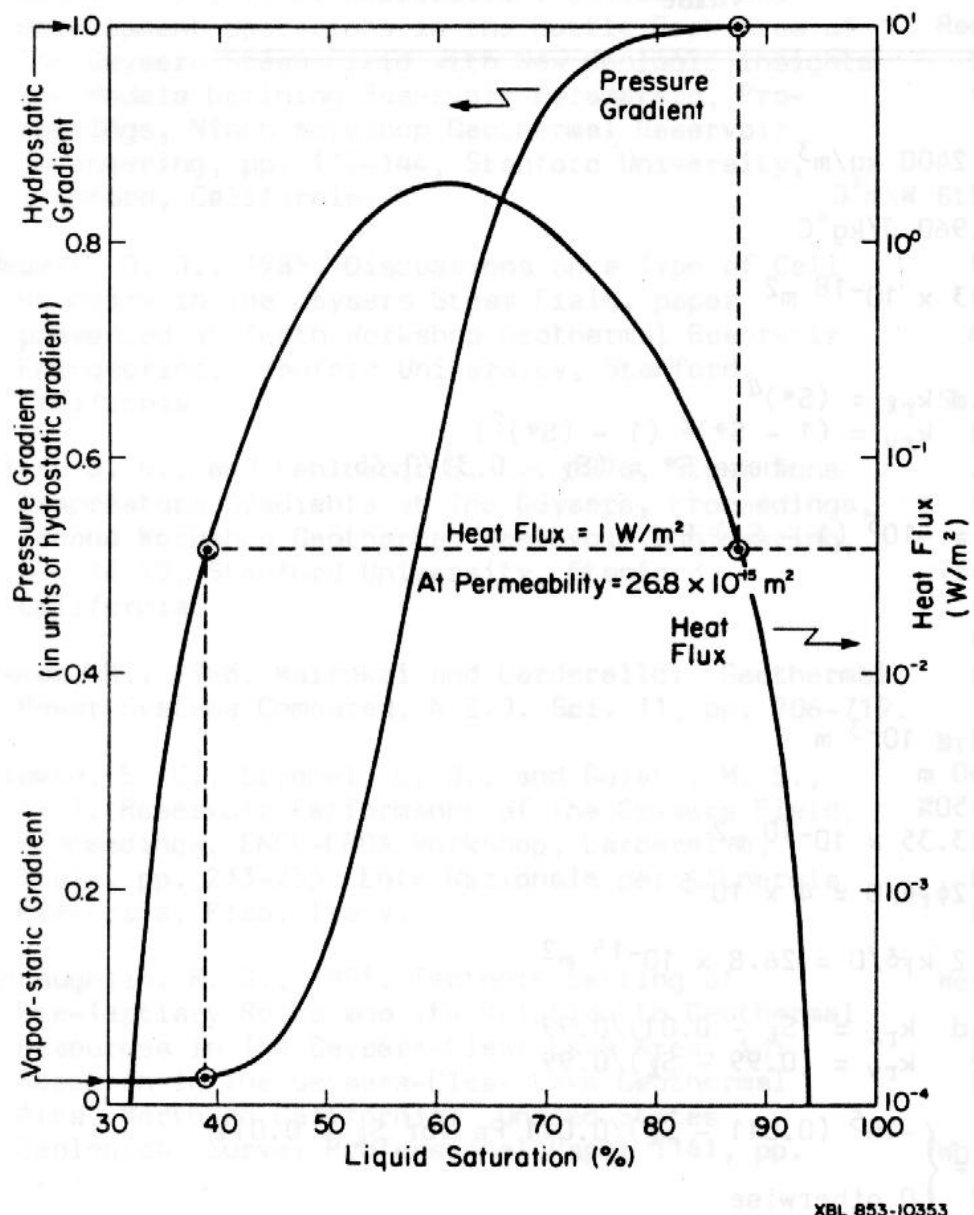


Figure 18.2. Heat flux and pressure gradient in a vertical porous heat pipe (from Pruess, 1985).

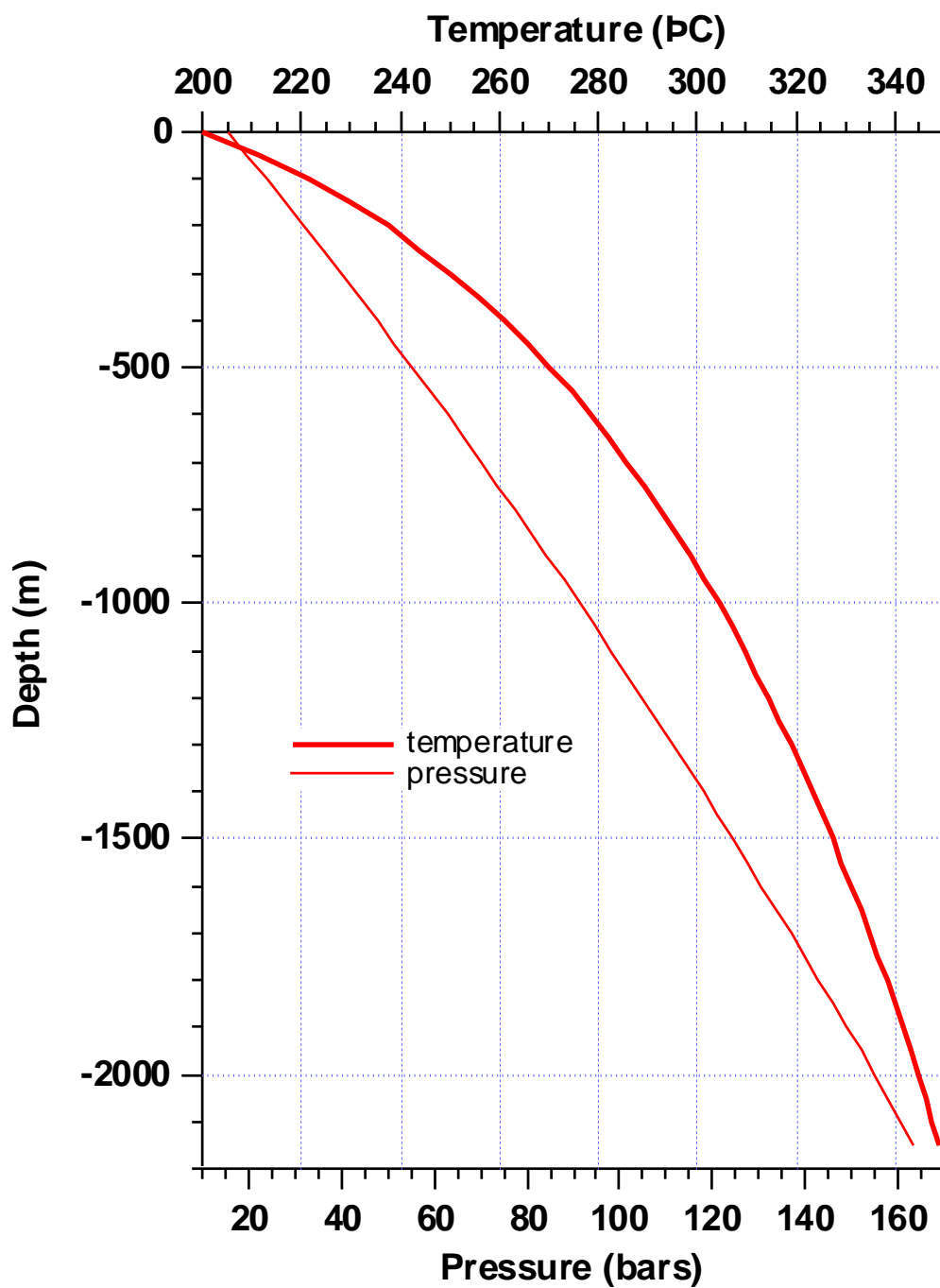


Figure 18.3. Boiling-point-for-depth (BPD) curve for pure water. Depth is measured relative to the elevation of the 200 °C isotherm.

19. Flow Instabilities

Non-isothermal and two-phase flow systems are capable of unstable behavior. Changes in fluid density can alter the balance between pressure and gravity forces, which can give rise to changes in flow patterns. Here we examine two examples, drawn from the Cerro Prieto, Mexico, and Mutnovsky, Russia, geothermal fields, respectively.

19.1 Cerro Prieto

The Cerro Prieto geothermal field, located in northern Mexico near the California border, is a liquid-dominated system that has been in production since 1973. Current installed capacity is 720 MW. Large-scale exploitation has caused substantial changes in the natural flow regime (Gutiérrez and Rodríguez, 2000). Analysis of geological, geochemical, and reservoir engineering data showed that deep, hot fluid ascends through a major fault (fault H) to recharge the geothermal system (Lippmann et al., 2000). Later work provided evidence that in response to pressure decline from production flow in the upper part of fault H had reversed, and that it had become a pathway for downflow of shallow, cool groundwaters. A simulation study was undertaken to investigate whether this flow reversal was consistent with known reservoir conditions and processes (Lippmann et al., 2000). Fig. 19.1 shows the 2-D vertical section model used in the study. The system was run to steady state, corresponding to natural-state conditions prior to large-scale production that commenced in 1986-87 in the CP-II and CP-III areas. By matching the temperature distribution, it was estimated that upflow in the H-fault occurs at a rate of 2.05×10^{-2} kg/s per meter of fault thickness, of which approximately 90 % enters the CP III reservoir and exits at the northwestern boundary, while the remaining 10 % of upflow flows into the aquifer. Subsequently, production was applied uniformly across the top of the CP III reservoir at a rate of 2.28×10^{-5} kg/s m². This causes pressures to decline in the reservoir and in the fault zone, and reduces the rates of upflow until eventually a flow reversal takes place and fluids start flowing downward from the aquifer towards the CP III reservoir. Fine gridding is required, especially near the top of the fault, in order to accurately resolve the timing of the reversal. Once fluid from the aquifer (i.e., groundwater) enters the fault, downflow increases rapidly due to the larger gravitational body force on the cooler and denser fluid. This causes reductions in vapor saturation in the reservoir (Fig. 19.2). Produced enthalpies decrease and recharge fractions increase (Fig. 19.3), in general agreement with field observations.

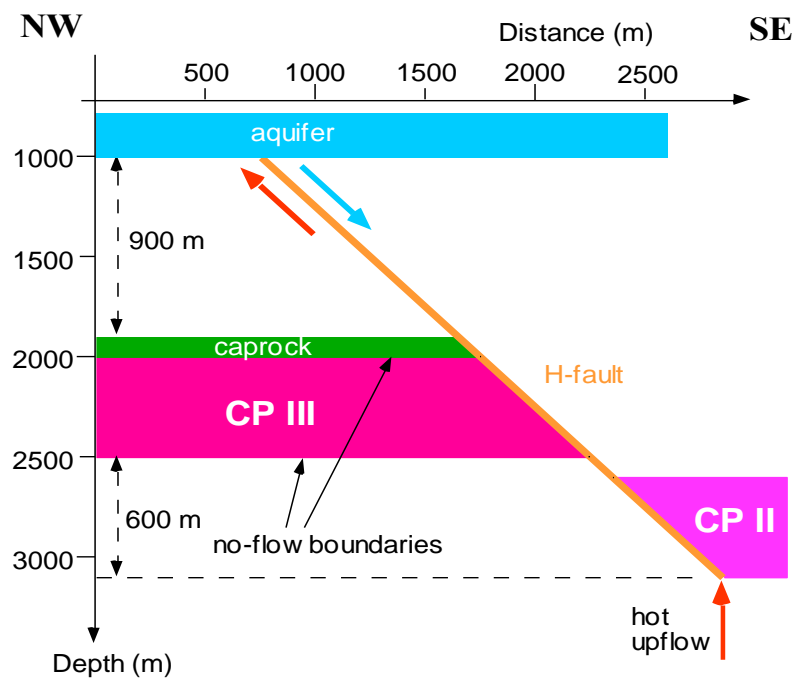


Figure 19.1. 2-D vertical section model for fluid recharge at Cerro Prieto.

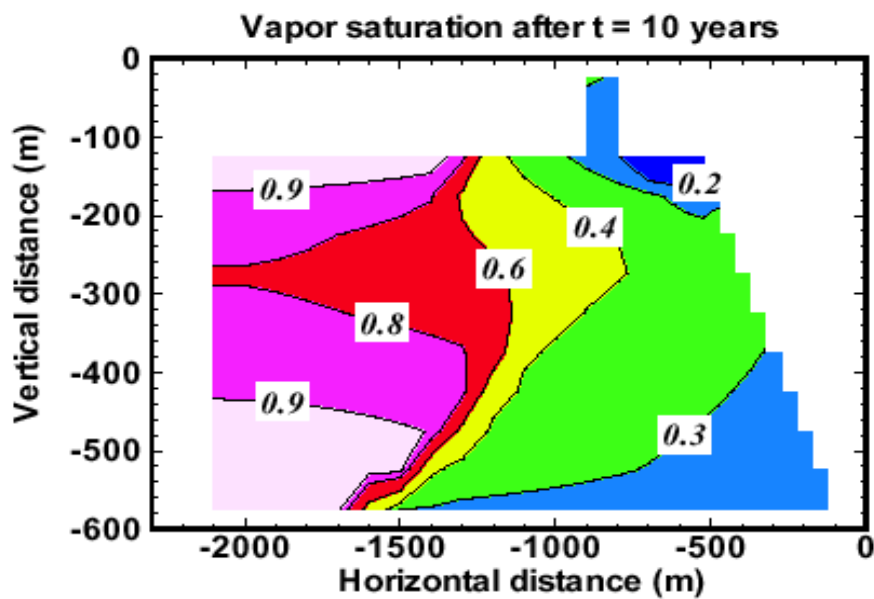


Figure 19.2. Simulated vapor saturations in the CP III reservoir after 10 years of production.

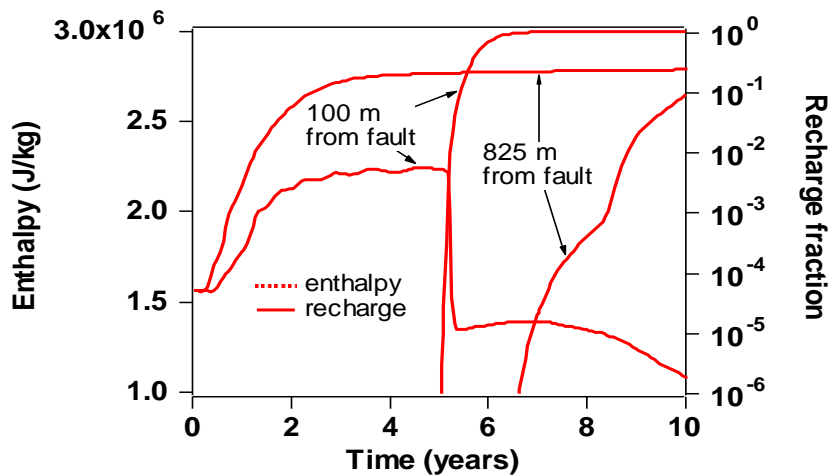


Figure 19.3. Enthalpy and groundwater recharge fraction histories for two locations in the model at different distances from the fault H in the Cerro Prieto field.

19.2 Mutnovsky

It is not uncommon for wells producing from high-temperature and two-phase geothermal systems to show unstable and time-varying behavior. Instabilities may be caused by an interplay of fluids from different feed zones intersected by a wellbore. Here we consider an example where cyclic internal flows in a wellbore are triggered by an external perturbation.

The Mutnovsky geothermal field is located in the Kamchatka peninsula in far eastern Russia. The reservoir is liquid-dominated with fluid temperatures from 235 - 270 °C. Reservoir fluids contain approximately 1% non-condensable gas, mostly CO₂, pressure conditions are close to two-phase, and permeability is fracture-dominated. Continuous high-resolution pressure monitoring revealed several episodes where modest earthquakes (magnitudes 3.9 - 4.5) at considerable distance (≈ 100 km) triggered cyclic pressure variations with amplitudes of 0.2 to 1 bar, and time periods from 30 to 90 minutes (Fig. 19.4; Kiryukhin and Pruess, 2000). A modeling study was undertaken with the objective of gaining insight into the underlying reservoir conditions.

It was hypothesized that the pressure cycling in well #30 may be caused by the interplay of two different fracture zones known to intersect this well, an upper fracture zone with a temperature of approximately 237 °C, and a lower fracture zone with a temperature of about 255 °C.

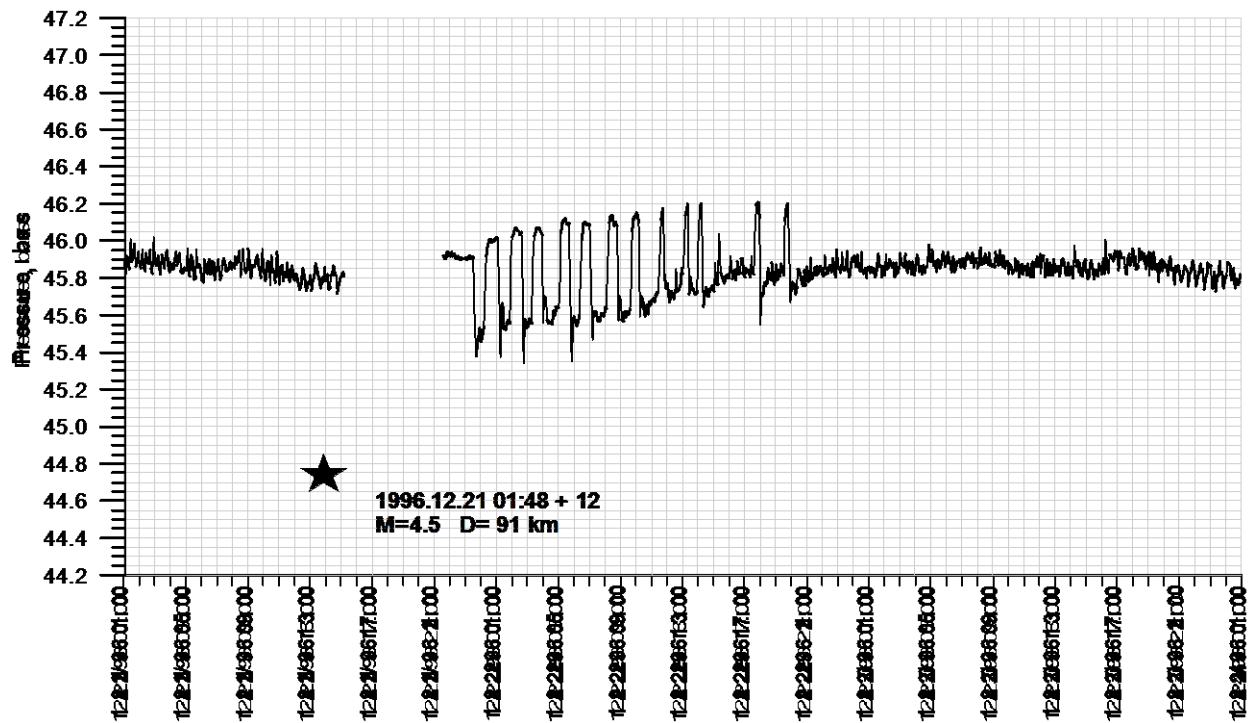


Figure 19.4. Example of co-seismic cycling in well #30, Verkhne-Mutnovsky site, Mutnovsky geothermal field (from Kiryukhin and Pruess, 2000).

The vertical distance between the zones is approximately 130 m (Fig. 19.5). A simplified numerical model was constructed which represents both fractures as horizontal regions with 1-D radial grids. The upper fracture was initialized in single-phase liquid conditions, while single- as well as two-phase conditions were used for the lower fracture. It was assumed that the only permeable features are the two fractures and the wellbore. The surrounding rock is treated as impermeable, but plays a role in conductive heat exchange with fluids in fractures and wellbore. The initial state of the system is hydrostatic equilibrium. Flow in the wellbore was approximated as porous flow with very large permeability. The two-phase fluid in the wellbore was represented as a homogeneous mixture, with density given by the volumetric average of water and steam.

$$\hat{\rho} = S_l \rho_l + S_g \rho_g \quad (19.1)$$

To examine whether such a system is capable of cyclic behavior, a step increase in pressure was applied in the upper zone, which initiates downflow through the wellbore into the lower zone. The simulated pressure distribution shown in Fig. 19.6 indeed shows cyclic behavior, and close inspection of the simulation reveals the following mechanism. In response to the downflow, pressures in the lower zone increase and downflow rates decline over time. On a slower time scale,

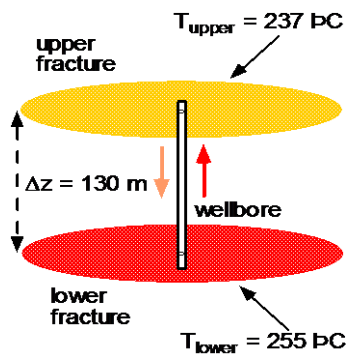


Figure 19.5. Conceptual model for flow cycling at Mutnovsky geothermal field, Kamchatka, Russia.

the cooler fluids introduced into the lower zone will be heated conductively. The associated expansion causes further pressure increase in the lower zone, reducing downflow rates, and providing more time for conductive heating of the downflowing fluid. Eventually the balance between fluid pressures and gravity body force will reverse, and upflow will be initiated. Upflow will be self-enhancing at first, due to the lower density of the hotter fluid going up in the wellbore. As pressures in the upper zone increase, upflow rates will decline. Then conductive cooling of the wellbore fluid will increase its density, until again downflow is initiated, starting a new cycle. What is driving the cycling is the “heat engine” provided by the temperature contrast between upper and lower zones. Every downflow episode will cause some temperature decline in the lower zone, while every upflow episode will cause some temperature increase in the upper zone. Over time, the cycling must “run down,” although the numerical simulation presented by Kiryukhin and Pruess (2000) only followed two cycles.

The amplitude of the pressure excursions is of order 0.5 - 1 bar, comparable to field observations at well #30. The simulated time period of approximately 1,400 hours, however, is almost three orders of magnitude larger than what was observed. At this point it is not known what other effects or conditions might cause more rapid cycling. A possible mechanism may be exsolution and dissolution of non-condensable gas in response to pressure variations. An alternative to the two-fractures model presented here and further discussion are given in the original paper (Kiryukhin and Pruess, 2000).

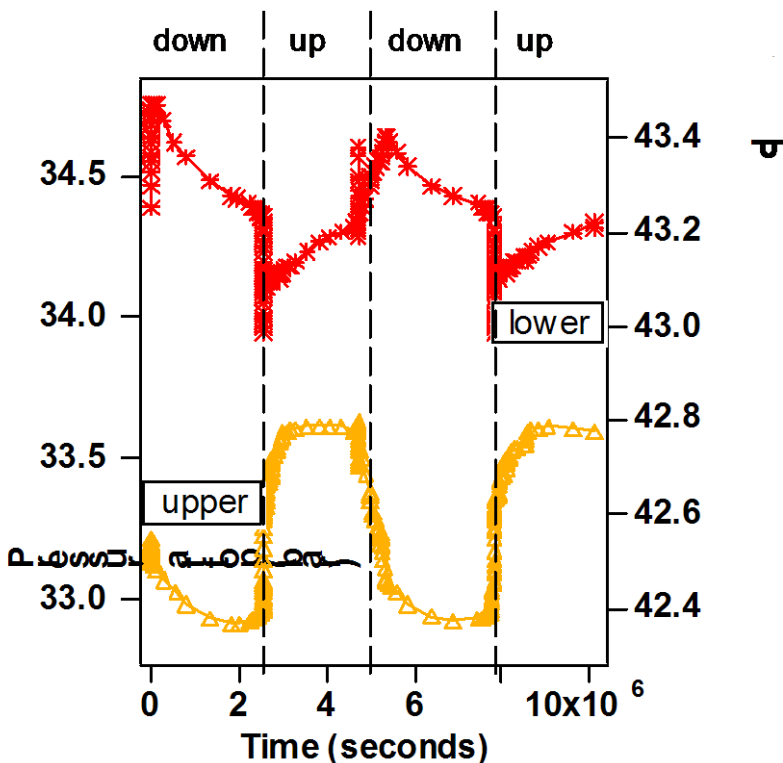


Figure 19.6. Simulated pressure behavior at intersection of upper and lower fractures with the wellbore. Directions of flow are labeled on top of the figure (after Kiryukhin and Pruess, 2000).

CONCLUDING REMARKS

The notes presented here are intended as an introduction into the practice of geothermal reservoir simulation. In the available space we could only give a brief overview of the subject. Readers are encouraged to use the substantial literature that is available in proceedings of geothermal conferences (Stanford, New Zealand and Geothermal Resources Council; World Geothermal Congresses), and in journals such as *Geothermics*. An excellent resource for finding literature on any geothermal subject is the Internet-based library database service that is provided free of charge by the Geothermal Resources Council (<http://www.geothermal.org/catalog.html>).

ACKNOWLEDGEMENT

For a review of the manuscript and valuable suggestions the author is indebted to Bo Bodvarsson, Alfredo Battistelli, and Marcelo Lippmann. This work was supported by the Assistant Secretary for Energy Efficiency and Renewable Energy, Office of Geothermal Technologies, of the U.S. Department of Energy under Contract No. DE-AC03-76SF00098.



REFERENCES

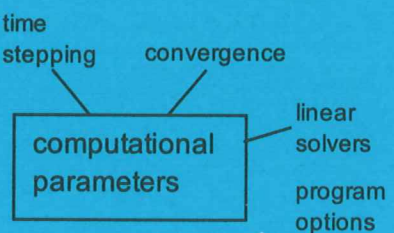
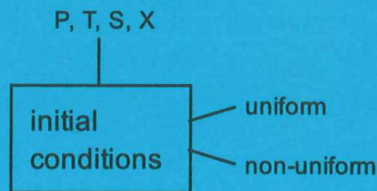
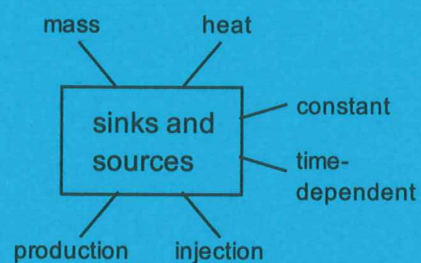
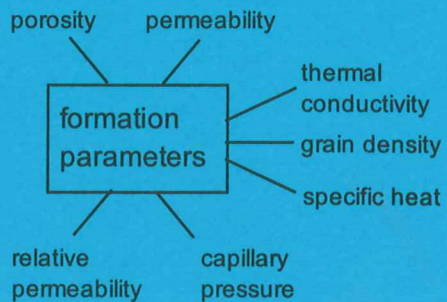
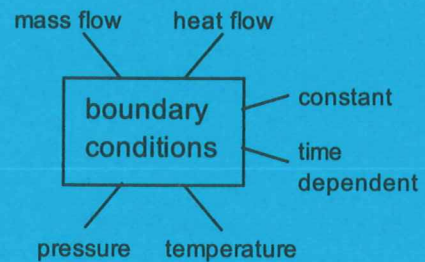
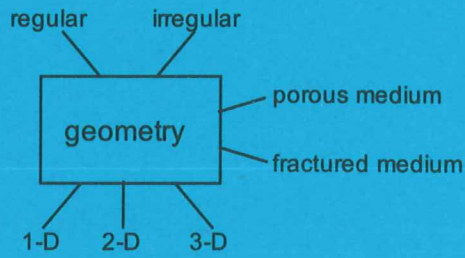
- Aunzo, Z.P., G. Bjornsson and G.S. Bodvarsson. Wellbore Models GWELL, GWNACL, and HOLA, Lawrence Berkeley National Laboratory Report LBL-31428, Berkeley, CA, October 1991.
- Barenblatt, G.E., I.P. Zheltov and I.N. Kochina. Basic Concepts in the Theory of Seepage of Homogeneous Liquids in Fissured Rocks, *J. Appl. Math.*, 24 (5), 1286-1303, 1960.
- Baria, R., J. Baumgärtner, A. Gérard, and J. Garnish, The European HDR Programme: Main Targets and Results of the Deepening of the Well GPK2 to 5000 m, *Proceedings, World Geothermal Congress 2000, Japan*, pp. 3643 - 3652, 2000.
- Battistelli, A., C. Calore and K. Pruess. The Simulator TOUGH2/EWASG for Modeling Geothermal Reservoirs with Brines and Non-Condensable Gas, *Geothermics*, Vol. 26, No. 4, pp. 437 - 464, 1997.
- Beall, J.J., M.C. Adams and P.N. Hirtz. R-13 Tracing of Injection in The Geysers, *Transactions, Geothermal Resources Council*, Vol. 18, pp. 151 - 159, 1994.
- Beall, J.J., M.C. Adams and P.N. Hirtz. Evaluation of R134a as an Injection Water Tracer in the Southeast Geysers, *Transactions, Geothermal Resources Council*, Vol. 22, pp. 569 - 573, 1998.
- Bird, R., W.E. Stewart and E.N. Lightfoot. *Transport Phenomena*, John Wiley & Sons, New York, NY, 1960.
- Birkholzer, J.T. and Y.W. Tsang. Pretest Analysis of the Thermal-Hydrologic Conditions of the ESF Drift Scale Test, Yucca Mountain Project Level 4 Milestone SP9322M4, Lawrence Berkeley National Laboratory, Berkeley, CA, 1997.
- Bodvarsson, G. Thermal Problems in the Siting of Rejection Wells, *Geothermics*, 1 (2), 63-66, 1972.
- Bodvarsson, G. S., K. Pruess, V. Stefansson, S. Björnsson and S. B. Ojiambo. A Summary of Modeling Studies of the East Olkaria Geothermal Field, Kenya, *Geothermal Res. Council, Transactions, International Volume*, 295-301, 1985.
- Bodvarsson, G.S., K. Pruess and M.J. Lippmann. Modeling of Geothermal Systems, *J. Pet. Tech.*, Vol. 38, No. 10, pp. 1007 - 1021, 1986.
- Bodvarsson, G.S. and P.A. Witherspoon. Geothermal Reservoir Engineering Part 1, *Geotherm. Sci. & Tech.*, Vol. 2, No. 1, pp. 1 - 68, 1989.
- Brownell, D.H., Jr., S.K. Garg and J.W. Pritchett. Governing Equations for Geothermal Reservoirs, *Water Resour. Res.*, Vol. 13. No. 6, 1977.
- Corey, A.T. The Interrelation Between Gas and Oil Relative Permeabilities, *Producers Monthly*, pp. 38 - 41, 1954.

- Finsterle, S., G. Björnsson, K. Pruess and A. Battistelli. Evaluation of Geothermal Well Behavior Using Inverse Modeling, in B. Faybishenko, P.A. Witherspoon, S.M. Benson (ed.), *Dynamics of Fluids in Fractured Rock*, Geophysical Monograph 122, pp. 377 - 387, American Geophysical Union, Washington, DC, 2000.
- Grant, M.A., I.G. Donaldson and P.F. Bixley. *Geothermal Reservoir Engineering*, Academic Press, New York, 1982.
- Gutiérrez, H.P. and Rodríguez, M.H. 28 Years of Production at Cerro Prieto Geothermal Field, *Proceedings*, World Geothermal Congress 2000, Japan, pp. 855 - 859, 2000.
- Hadgu, T. and D.H. Freeston. A Multi-Purpose Wellbore Simulator. *Geothermal Resources Council Transactions*, Vol. 14, pp. 1279 - 1286, 1990.
- Hadgu, T., R.W. Zimmerman and G.S. Bodvarsson. Coupled Reservoir-Wellbore Simulation of Geothermal Reservoir Behavior. *Geothermics*, Vol. 24, No. 2, pp. 145-166, 1995.
- International Formulation Committee. A Formulation of the Thermodynamic Properties of Ordinary Water Substance, IFC Secretariat, Düsseldorf, Germany, 1967.
- Keenan, J.S., F.G. Keyes, P.G. Hill and J.G. Moore. *Steam Tables - Thermodynamic Properties of Water Including Vapor, Liquid, and Solid Phases*, John Wiley & Sons, New York, 1969.
- Kiryukhin, A. and K. Pruess, Modeling Studies of Pressure Cycling Associated with Seismicity in Mutnovsky Geothermal Field, Kamchatka, Russia, *Proceedings*, World Geothermal Congress 2000, Japan, pp. 2659 - 2664, 2000.
- Lauwerier, H.A. The Transport of Heat in an Oil Layer Caused by the Injection of Hot Fluid, *Appl. Sci. Res.*, 5, Section A (2-3), 145-150, 1955.
- Lippmann, M.J., A.H. Truesdell and K. Pruess. The Control of Fault H on the Hydrology of the Cerro Prieto III Area, *Proceedings*, Twenty-Fifth Workshop on Geothermal Reservoir Engineering, Stanford University, pp. 266 - 274, 2000.
- Murray, L. and C. Gunn. Toward Integrating Geothermal Reservoir and Wellbore Simulation: TETRAD and WELLSIM, Proc. 15th NZ Geothermal Workshop, Auckland, New Zealand, 1993.
- O'Sullivan, M.J. A Similarity Method for Geothermal Well Test Analysis, *Water Resour. Res.*, Vol. 17, No. 2, pp. 390 – 398, 1981.
- O'Sullivan, M.J., G.S. Bodvarsson, K. Pruess and M.R. Blakeley. Fluid and Heat Flow in Gas-rich Geothermal Reservoirs, *Soc. Pet. Eng. J.*, 25 (2), 215–226, 1985.
- O'Sullivan, M.J., K. Pruess and M.J. Lippmann. State of the Art of Geothermal Reservoir Simulation, *Geothermics*, Vol. 30, No. 4, pp. 395 - 429, 2001.
- Pruess, K. GMINC - A Mesh Generator for Flow Simulations in Fractured Reservoirs, Report No. LBL-15227, Lawrence Berkeley Laboratory, Berkeley, CA, 1983.

- Pruess, K. A Quantitative Model of Vapor Dominated Geothermal Reservoirs as Heat Pipes in Fractured Porous Rock, *Geothermal Resources Council, Transactions*, 9, Part II, 353-361, 1985.
- Pruess, K. TOUGH User's Guide, Nuclear Regulatory Commission Report NUREG/CR-4645; also Lawrence Berkeley Laboratory Report LBL-20700, 1987.
- Pruess, K. Grid Orientation and Capillary Pressure Effects in the Simulation of Water Injection into Depleted Vapor Zones, *Geothermics*, 20 (5/6), 257-277, 1991.
- Pruess, K. Injection Plume Behavior in Fractured, Vapor-Dominated Reservoirs, *Proceedings*, 21st Workshop on Geothermal Reservoir Engineering, Stanford University, pp. 413 - 420, Stanford, CA, 1996.
- Pruess, K. On Vaporizing Water Flow in Hot Sub-Vertical Rock Fractures, *Transport in Porous Media*, Vol. 28, pp. 335 - 372, 1997.
- Pruess, K. Numerical Simulation of Multiphase Tracer Tests in Fractured Geothermal Reservoirs, in press in *Geothermics*, 2002.
- Pruess, K. and G.S. Bodvarsson. Thermal Effects of Reinjection in Geothermal Reservoirs with Major Vertical Fractures, *J. Pet. Tech.*, Vol. 36, No. 10, pp. 1567 – 1578, 1984.
- Pruess, K. and J. García. A Systematic Approach to Local Grid Refinement in Geothermal Reservoir Simulation, *Proceedings*, World Geothermal Congress 2000, Japan, pp. 2809 - 2814, 2000.
- Pruess, K., and T.N. Narasimhan. On Fluid Reserves and the Production of Superheated Steam from Fractured, Vapor-Dominated Geothermal Reservoirs, *J. Geophys. Res.*, 87 (B11), 9329-9339, 1982.
- Pruess, K. and T.N. Narasimhan. A Practical Method for Modeling Fluid and Heat Flow in Fractured Porous Media, *Soc. Pet. Eng. J.*, 25 (1), 14-26, 1985.
- Pruess, K., C. Calore, R. Celati and Y.S. Wu. An Analytical Solution for Heat Transfer at a Boiling Front Moving Through a Porous Medium, *Int. J. of Heat and Mass Transfer*, 30 (12), 2595-2602, 1987.
- Pruess, K., C. Oldenburg and G. Moridis. TOUGH2 User's Guide, Version 2.0, Lawrence Berkeley National Laboratory Report LBNL-43134, Berkeley, CA, 1999.
- Scheidegger, A. E. Statistical Hydrodynamics in Porous Media, *J. Appl. Phys.*, 25 (8), 994-1001, 1954.
- Theis, C.V. The Relationship Between the Lowering of Piezometric Surface and the Rate and Duration of Discharge Using Ground Water Storage, *Trans. AGU*, pp. 519 - 524, 1935.
- van Genuchten, M.Th. A Closed-Form Equation for Predicting the Hydraulic Conductivity of Unsaturated Soils, *Soil Sci. Soc. Am. J.*, Vol. 44, pp. 892 - 898, 1980.

- Vinsome, P.K.W. and J. Westerveld. A Simple Method for Predicting Cap and Base Rock Heat Losses in Thermal Reservoir Simulators, *J. Canadian Pet. Tech.*, Vol. 19, No. 3, pp. 87 – 90, 1980.
- Warren, J.E. and P.J. Root. The Behavior of Naturally Fractured Reservoirs, *Soc. Pet. Eng. J., Transactions, AIME*, 228, 245-255, 1963.
- White, D.E., L.J.P. Muffler, and A.H. Truesdell. Vapor-Dominated Hydrothermal Systems Compared with Hot-Water Systems, *Economic Geology*, 66 (1), 75-97, 1971.

DATA GROUPS FOR A SIMULATION PROBLEM



ISBN 9979-68-100-4